STRUCTURE AND PROPERTIES OF ORGANIC AND INORGANIC COMPOSITES MATERIALS: FROM ORGANIC PHOTOVOLTAIC CELLS TO AEROSPACE MATERIALS

Benjamin Agyei-Tuffour
BSc. (Hons) KNUST-Ghana, MSc. (NTNU-Norway)

A THESIS PRESENTED TO THE AFRICAN UNIVERSITY OF SCIENCE AND TECHNOLOGY IN CANDIDACY FOR THE DEGREE OF DOCTOR OF PHILOSOPHY

RECOMMENDED FOR ACCEPTANCE BY THE DEPARTMENT OF MATERIALS SCIENCE AND ENGINEERING

ADVISOR: WINSTON O. SOBOYEJO

NOVEMBER 2017

Structure and Properties of Organic and Inorganic Composites Materials: From Organic Photovoltaic Cells to Aerospace Materials

By

Benjamin Agyei-Tuffour

A THESIS APPROVED BY THE DEPARTMENT OF MATERIALS SCIENCE AND ENGINEERING

RECOMMENDED**: ……**

PhD Advisor, Professor Winston Oluwole Soboyejo

……..…….
Head, Dept. of Materials Science and Engineering

…….
Approved:
Vice President, Academics

Date:…….

Dedication

With much love,

this dissertation is dedicated to my family,

my parents, Mr. and Mrs. Agyei-Tufuor,

my dearest wife, Victoria

and my adorable girls, Afia and Nana Yaa.

ABSTRACT

Pressure and contacts in materials and systems play crucial roles in their performance and also their eventual failures. Pressure application closes voids, bridges gaps and improves transport across interfaces. In thin film technology of multiple layers which are usually stacked together, photonic and electrical charge transports across the interfaces can have direct consequences on the performance and failures. This study explores the effects of pressure and contacts in bulk heterojunction organic, inorganic and hybrid materials used in photovoltaic applications. We present a review of the state-of-the-art in the theoretical study of the structure of the photovoltaic cells. It involves the application of pressure on contacts between the layers of the organic photovoltaic cells with poly (3-hexylthiophene):phenyl-C61-butyric acid methyl ester (P3HT:PCBM) as the active layer. The contacts between the layers were modeled using analytical concepts and finite element models. The potential effects of surface roughness and dust particles were modeled along with the effects of lamination pressure and adhesion energy. The results show that, increased pressure is associated with decreased void length or increased contact length. The contacts associated with the interfaces between the active layer and the hole/electron injection layer poly(3,4-ethylenedioxythiophene: poly styrenesulphonate (PEDOT.PSS) and Molybdenum trioxide (MoO_3) are also compared. The implications of the results are discussed for the design of stamping/lamination processes for the fabrication of organic photovoltaic cells.

The morphology of active layers of organic photovoltaic cells plays crucial roles in achieving good performing devices with longer life span. The study of the active layer materials therefore explored an improved way of processing the active layer to enhance charge transport and lifetime of the conjugated polymer blends. The process of fabricating these devices included post deposition thermal annealing, which increases the crystallinity and enhances phase-separated

domains of deposited active layer components. A blended composite of regioregular poly(3-hexylthiophene) (P3HT) and phenyl-C61-butyric acid methyl ester (PCBM) used as the active layer in this Bulk heterojunction (BHJ) photovoltaic cell and annealed at different temperatures coupled with the application of pressure. AFM, SEM and GIWAXS techniques were employed to observe the nano- and micro- structures of the various active layers after quenching to room temperature. A better understanding of the correlation between the observed microstructures and electrical characteristic of the active layers are therefore used to explain the performance of organic photovoltaic cells.

Finally, Silicon carbide-fiber-reinforced silicon carbide matrix composites (SiC/SiC CMCs) have been proven to possess greater high-temperature strength and durability. These materials are usually used in air breathing engines due to their unique properties. However, the application of SiC/SiC CMCs is ineffective in combustion environment due to oxidation and surface recession. Efforts to improve service of SiC/SiC CMCs in combustion environments require knowledge of their long-term stability in combustion environments, volatility, phase stability, and thermal conductivity. Therefore in this chapter, the design of a reliable EBC for SiC/SiC CMCs with excellent corrosion, recession and thermal shock resistance is proposed. This design consists of a three-multilayer; yttrium disilicate/mullite/ytterbium disilicate ($Y_2Si_2O_7$/ $3Al_2O_3{\cdot}2SiO_2$ /$Yb_2Si_2O_7$) system. Also, finite element models (FEMs) are used to predict the thermal residual stresses within the proposed multilayers under operating conditions. The implications of the results are discussed for potential application of this EBC system in aerospace engines.

List of Publications

Text Book Chapters

- **B. Agyei-Tuffour**, E.R. Rwenyagila, J. Asare, O.K. Oyewole, M.G. Zebaze Kana, D. M. O'carroll And W.O. Soboyejo, *"Influence of Pressure on contacts between Layers of hybrid organic/inorganic Photovoltaic Cells*". Advanced Materials Research Vol. 1132 (2016) pp 204-216 © (2016) Trans Tech Publications, Switzerland. doi:10.4028/www.scientific.net/AMR.1132.204

Peer Reviewed Journals

- **Benjamin Agyei-Tuffour**, N.Y. Doumon, E. R. Rwenyagila, J. Asare, O. K. Oyewole, Z. Shen, C. E. Petoukhoff, M. G. Zebaze Kana, D. M. Ocarroll, and W. O. Soboyejo. Pressure Effects on Interfacial Surface Contacts and Performance of Organic Solar Cells, *Journal of Applied Physics.*, 2017, (in press):

- **Benjamin Agyei-Tuffour**, Egidius R. Rwenyagila, Joseph Asare, M.G. Zebaze Kana and Winston O. Soboyejo, Effects of Pressure on Nano- and Micro- scale Morphological Changes in Conjugated Polymer Photovoltaic Cells**,** *Journal Materials Research*., 2016, DOI: http//dx.doi.org/10.1557/jmr.2016.344, http://journals.cambridge.org

- **Benjamin Agyei-Tuffour,** Y. D. Bensah, L. N. W. Damoah, D. Dodoo-Arhin, E. Annan, J. K. Efavi, E. Sarkodee. "Synthesis and microstructural characterization of kaolin – polyethylene composites". *Polymer Composites*, 35, 1507–1515, 2014.

- **Benjamin Agyei-Tuffour,** E. Annan, E. R. Rwenyagila, E. Ampaw, E. Arthur, K. Mustapha, S. Kolawole, W. O. Soboyejo, M. I. Marinov and D. D. Radev. *Untraditional Synthesis of Ni-Based Alloys for Medical Application, ARPN Journal of Engineering and Applied Sciences, **Vol 6 No. 4,** 2013.*

- **Benjamin Agyei-Tuffour,** E. Annan, E. R. Rwenyagila, E. Ampaw, E. Arthur, K. Mustapha, S. Kolawole, W. O. Soboyejo, D. D. Radev. Untraditional Synthesis of Boron-Containing Superhard and Refractory Materials - A Review, *Global Journal of Engineering Design and Technology*, pg 21-26, 2013.

- E. R. Rwenyagila, **Benjamin Agyei-Tuffour**, K. O. Onogu, O. Akin-Ojo, M. G. Zebaze Kana, T. L. Alford, And W. O. Soboyejo. Computational modeling of optical properties in aluminum nanolayers inserted in ZnO for solar cell electrodes. 3914 Vol. 40, No. 16, 2015 / *Optics Letters.*

- E. R. Rwenyagila, **Benjamin Agyei-Tuffour**, Martiale Gaetan Zebaze Kana, Omololu Akin-Ojo Winston Oluwole Soboyejo. Optical properties of ZnO/Al/ZnO multilayer films for large area transparent electrodes, *Journal Materials Research*., 2014, DOI: 10.1557/jmr.2014.298, http://journals.cambridge.org

- A. Yaya, C.P. Ewels, J.K. Efavi, **Benjamin Agyei-Tuffour**, K. Kan-Dapaah, B. Onwona Agyeman, E. K.K. Abavare, Ali Hassanali and P.R.Briddon, A study of polybromide chain formation using carbon nanomaterials via density functional theory approach, *Cogent Engineering* (2016), 3: 1261509 http://dx.doi.org/10.1080

- J. Asare, S. A. Adeniji, O. K. Oyewole, **Benjamin Agyei-Tuffour**, J. Du, E. Arthur, A. A. Fashina, M. G. Zebaze Kana, and W. O. Soboyejo, "Cold welding of organic light emitting diode: Interfacial and contact models". *AIP Advances* 6, 065125 (2016); doi: 10.1063/1.4955141

- E. K. Arthur, E. Ampaw, S. T. Azeko, Y. Danyuo, **Benjamin Agyei-Tuffour**, K. Kan-Dapaah, J. D. Obayemi. Design of Thermally Reliable Environmental Barrier Coating for SiC/SiC Ceramic Matrix Composites. *International Journal of Composite Materials* 2013, **3(6)**: 191-197 DOI: 10.5923/j.cmaterials.20130306.08

- E. Nyankson, **Benjamin Agyei-Tuffour**, J. Asare, E. Annan, E. R. Rwenyagila, D. S. Konadu, A. Yaya & D. Dodoo-Arhin. (2013) "Nanostructured TiO_2 and their energy Applications-a review". *Journal of Engineering and Applied Sciences*, **8 [10]** 871-886.

- D. Dodoo-Arhin, S. A. Mensah, A. Yaya, **Benjamin Agyei-Tuffour**, Application of Discarded Rubber Car Tyres as Synthetic Coarse Aggregates in Light Weight Pavement Concretes. *American Journal of Materials Science* 2015, 5(4): 75-83 DOI: 10.5923/j.materials.20150504.01

- E. Nyankson, **Benjamin Agyei-Tuffour**, E. Annan, D. Dodoo-Arhin, A. Yaya, L. D. Brefo, E. S. Okpoti & E. Odai, Characteristics of Stabilized Shrink-Swell Clay Deposits using Eggshell Powder. *Global Journal of Engineering Design and Technology*, G.J. E.D.T., Vol. 2(3) 2013:1-7.

- A. Yaya, **Benjamin Agyei-Tuffour**, D. Dodoo-Arhin, E. Nyankson, E. Annan, D. S. Konadu, E. Sinayobye, E. A. Baryeh and C. P. Ewels. (2012). "Layered Nanomaterials - A Review". *Global Journal of Engineering, Design & Technology*, 1[1] 32-41. http://www.gifre.org/admin/papers/gjedt/1222 -32-41.pdf

- E. Annan, **Benjamin Agyei-Tuffour**, L. N.W. Damoah, B. Mensah, and D.S. Konadu, Nyankson, "Physico-mechanical properties of Bayer Residue-Clay bricks", *ARPN Journal of Eng & Applied Sciences Vol. 7,* No. 12, December 2012

- Y. D. Bensah, **Benjamin Agyei-Tuffour**, Lucas N. W. Damoah and Johnson K. Efavi, Processing Of Waste Polyethylene Into Polymer-Ceramic Composite Through Lipid Assisted Melt Compounding, *ARPN Journal of Engineering and Applied Sciences*, VOL. 7, NO. 6, JUNE 2012

Conference Proceedings

- **B. Agyei-Tuffour**, C.E. Petoukhoff, Z. Shen , E. R. Rwenyagila , J. Asare , D.M. O'Carroll and W.O. Soboyejo. Pressure-induced microstructural changes in conjugated polymer photovoltaic cells." MRS-Africa 2015, University of Ghana, Accra-Ghana, 7 – 10 December, 2015
- **Benjamin Agyei-Tuffour,** Peter Spattocco**,** Christopher E. Petoukhoff, Winston O. Soboyejo, Deidre M. O'Carroll "The effects of surface modification of Thin Ag electrodes on hole injection/collection for conjugated polymer optoelectronics, MRS Fall Meeting, Boston 29th November-4th December, 2014.
- **B. Agyei-Tuffour,** E. R. Rwenyagila, J. Asare, O. K. Oyewole, K. O. Onogu, M. G. Z. Kana, A. A. Oberafo, W. O. Soboyejo. "Effects of pressure on contacts between layers of organic solar cells". Organic Photovoltaics XIV Conference 25 - 29 August 2013, San Diego Convention Center, California United States.
- **B. Agyei-Tuffour**, J. Asare, W.O. Soboyejo; "AUST-NASENI workshop on Advanced Manufacturing and Nanotechnology", ***Facilitators for Green Design Technology***, African University of Science and Technology (AUST), 5-10th February, 2013.
- **B. Agyei-Tuffour**, E. Doumon, E. R. Rwenyagila, J. Asare, O. K. Oyewole, M. G. Zebaze Kana, K.O. Onogu, W. O. Soboyejo, " Pressure on contacts between Layers in Organic Photovoltaic Cells, Nigerian Materials Congress (NIMACON 2012), Obafemi Awolowo University (OAU), 21-24th November 2012.
- J. Asare, **B. Agyei-Tuffour** , O. K. Oyewole, D.Y. Momodu, G. M. Zebaze-Kana, and W. O. Soboyejo, "Effects of Deformation on Failure Mechanisms and Optical Properties of Flexible Organic Solar Cell Structures". African Materials Research Society Conference; Addis Ababa (Ethiopia), December 2013.
- O.K. Oyewole, D.O. Oyewole, J. Asare, **B. Agyei-Tuffour**, M.G. Zebaze Kana, W.O. Soboyejo. Failure Mechanisms in Layers Relevant to Stretchable Organic Solar Cells. African Materials Research Society Conference; Addis Ababa (Ethiopia), December 2013.

Manuscript in Preparation

- **Benjamin Agyei-Tuffour**, Christopher E. Petoukhoff, Winston O. Soboyejo, Deidre M. O'Carroll "The effects of surface modification of Thin Ag electrodes on hole injection/collection for conjugated polymer optoelectronics.

ACKNOWLEDGEMENTS

First of all, I would like to express my sincere gratitude and appreciation to my advisor, Professor Winston Oluwole Soboyejo, for his supervision, support and encouragement throughout these years. I greatly appreciate Professor Soboyejo for his in-depth knowledge, dedication, discussions, direction and immense motivation for this research. Also, I have to thank Professor D.M O'Carroll, Professor Eric Garfunkel and Dr. Johanna Bernstein for facilitating my visit to Rutgers University, for the supervision and valuable discussions about my research and thesis. I again express my appreciation to Prof. Zebaze Kana, Dr. Omololu Akin-Ojo and Prof. Boateng Onwona-Agyeman for the useful discussions and comments as my dissertation committee members.

I am grateful again to Professor Dimitar Radev of the Bulgarian Academy of Sciences and Dr. Emmanuel Boakye, Dr. Demien Viory, Dr. Roney Thomas, Postdoctoral fellows of IAMDN, Rutgers University for their useful laboratory assistance and technical discussions. I am also grateful to Christopher Petoukhoff, Binxing Yu, Catrice Carter, Zeqing Shen for their Laboratory assistance and useful technical assistance. I am also grateful Dr. Kevin Yager of Brookhaven National Laboratory for the access and training on the Synchrotron Light Source (NSLS X9 Beamline). Acknowledgments go to Shawn Ward of Rutgers University for the assistance with Raman experiment/analysis and nano-indentation measurements, Ryan Thorpe of the Department of Physics and the Laboratory for Surface Modification (LSM) for the training and useful discussions on X-ray Photoelectron Spectroscopy (XPS) and Ultraviolet Photoelectron Spectroscopy (UPS) experiments.

There are several people in the Soboyejo research group I would like to acknowledge for their contributions. I would like to thank Egidius Rwenyagila, Joseph Asare, Kehinde Oyewole

and Adebayo Fashina for the research collaborations, support and helpful discussions. Appreciation is also extended to my colleagues, Kwabena Kan-Dapaah and Ebenezer Annan for their support, encouragement and valuable discussions throughout the PhD struggle both at home and abroad.

My PhD studies was largely supported by the University of Ghana-Carnegie Corporation Next Generation of African Academics (UG-Carnegie NGAA), the PAMI-World Bank African Centers of Excellence, the African Development Bank, World Bank STEP-B program, National Science Foundation through the Integrated Graduate Education and Research Training (IGERT) program at the Rutgers University, Institute for Advanced Materials, Devices and Nanotechnology (IAMDN). I am grateful to the UG-Carnegie Program Director and Fund Administrators, Professor Yaa Ntiamoah-Baidu, Mrs. Afua Yeboah, Mr. Collins Amofa and Ms. Jennifer Amponsah for their support.

Lastly but not the least, I thank Professor W. A. Asomaning of the University of Ghana, for his mentorship, care and support for me and my family and I also thank my loving family for their prayers and support.

TABLE OF CONTENTS

LIST OF TABLE CAPTIONS

LIST OF FIGURES

Chapter 1
Background and Introduction

1.0 Introduction

Composite Materials find applications in every facet of the world's economy such as in medicine, energy, transportation, infrastructure, etc., due to the increasing demand for faster, efficient, reliable and environmentally cleaner systems. For instance, composite materials for energy and air transport have become more important issues these years due to the fast development of our society and the limited fossil-fuel resources. There are two approaches in meeting these challenges. In solving the energy problem, one way is to reduce the energy consumption by improving the efficiency of energy utilization and the other is to generate more energy, especially from long-term renewable sources. Organic light-emitting diodes (OLEDs) and organic photovoltaic (OPV) are layered composite devices can help ease the energy scarcity. The aerospace materials challenge can be solved by reducing the weight of the aircrafts structural component with composites which is directly related to improved fuel economy as well as protecting the components with environmental barrier coatings and thermal barrier coatings (EBC/TBC's).

1.1 Composite materials in energy: Organic Photovoltaic (OPV) and Organic Light Emitting Devices (OLEDS)

The discovery of OLEDs by Tang *et al.* in 1987[1] has led to these devices ever receiving lots of attention as a full-color display panels and lighting devices. Credits to the tremendous development during the last two decades, OLED technology have been widely used in cell

phones and large screen TV displays. Typical OLED device structure is: glass substrate/transparent anode/hole transport layer (HTL)/emissive layer (EML)/electron transport layer (ETL) /reflective cathode, where organic layers are sandwiched between the anode and cathode. While ITO is the most popular transparent anode used to inject holes into the HTL, LiF/Al is usually used as the cathode to inject electrons into the ETL [2]. After the transport through the HTL and ETL, respectively, holes and electrons recombine with each other in the emissive layer (EML) and emit light.

Over the last two decades, much research has been devoted to improving the efficiency, reliability, and color quality of OLEDs, as well as to making them commercially viable. By doping the EML with high quantum yield molecules, high efficiency and color varieties can be achieved [3]. Other functional layers such as the hole injection layer (HIL) [4-7], the electron injection layer (EIL) [2, 8] and the exciton blocking layer (EBL) [9] were introduced to increase the device efficiency and lifetime. The device lifetime can be further improved by constructing a uniformly mixed [10] or graded mixed host layer [11]. When several EMLs were incorporated together, a white OLED can be fabricated and become attractive for lighting applications [12-14]. While the significant progress in materials and device structures led to a higher efficiency and longer lifetime for OLEDs, the detailed mechanisms underlying these improvements are not fully understood.

Organic photovoltaic devices [15], also known as organic solar cells, are devices that use organic active layers to absorb sunlight and generate electricity. Organic materials have low dielectric constants and therefore excitons (electron/holes pairs) that are strongly bonded to each other are generated instead of free charge carriers by the absorption of photons [2-4]. Because the exciton binding energy is significantly higher than the thermal energy (kT), another driving

force (usually a strong electric field) is needed to dissociate the electron-hole pairs into delocalized electrons and holes. In 1986, Tang *et al*. invented the planar heterojunction (PHJ) OPV device with a structure of glass substrate/anode/ donor layer (HTL)/acceptor layer (ETL)/cathode [15]. A donor-acceptor (DA) interface was introduced to dissociate the excitons. In this case, the device efficiency is further limited by the exciton diffusion length of the organic material since only those excitons arriving at the DA interface can dissociate efficiently. In the 1990s, a bulk heterojunction (BHJ) structure was introduced, which mixed the donor and acceptor material together in the active layer. Hence most excitons generated can reach the nearby DA interface and dissociate [16]. However, the low mobility of the organic materials will enhance the recombination loss during the extraction of the charge carriers. Meanwhile, a high electric field is still favorable for the dissociation of excitons at the DA interface which limits the device thickness and photon absorption as well. OLEDs and OPV devices have the similar device structure and completely reversed working process--OLEDs generate photons from charge carriers, while OPV devices do the reverse job. Such a correlation between the two types of devices provides a perspective to study them together using analytical and numerical simulations and experimental techniques.

1.2 Nano- and Micro-Composite Materials in the Aerospace industry

Composites materials have made significant in-roads into the aerospace industry. The conventional materials used include aluminum, steel and titanium due to their light weights however, there has been a dramatic shift to modern nano- and micro- composites structures for aircraft construction based on superior light weight and ease in components assembly [17-19]. The major driving forces for composites use as light weight structural elements in the aviation developments are the superior performance especially in military equipment development and

improved fuel economy and huge savings in maintenance cost in commercial airbus carriers. Additionally, older aircrafts with metallic components are increasingly being replaced with composites Composite materials involving fibers as reinforcements and resin matrix have largely dominated the aerospace industry as shown in Table 1.1. The materials are usually in the form of prepregs and a fabrication method of autoclave moulding. Other fabrication methods such as filament winding, oven curing, resin injection moulding and metallic tooling are also commonly used the production of shell-like components, low speed aircrafts and radomes.

Table 1.1 Properties of fiber reinforcements used in aerospace applications [19]

Reinforcing Fiber	Density (g/cc)	Modulus (GPa)	Strength (GPa)	Application areas
Glass				
E-Glass	2.55	65-75	2.2 - 2.6	• Small passenger a/c parts; radomes, rocket motor casings
S-glass	2.47	85-95	4.4 – 4.8	• Highly loaded parts in small passenger a/c
Aramid				
Low modulus	1.44	80 – 85	2.7 - 2.8	• Fairings; non load bearing parts
Intermediate modulus	1.44	120–128	2.7 – 2.8	• Radomes, some structural parts; rocket motor casings
High modulus	1.48	160 -170	2.3 – 2.4	• Highly loaded parts
Carbon				
Standard modulus (high strength)	1.77 –1.80	220–240	3.0 – 3.5	• Applied in aircraft satellites, antenna dishes, missiles, etc
Interm. modulus	1.77– 1.81	270–300	5.4 – 5.7	• High performance aircraft components
High modulus	1.77–1.80	390–450	2.8 – 3.0 4.0 – 4.5	• Control surface in aircrafts and Space structures.
Ultra-high strength	1.77–1.82	290 - 310	7.0 – 7.5	• Components of fighter jets, spacecrafts, etc for superior performance

Table 1.2. Common matrices used in the aviation industry **[19]**

Thermosets				**Thermoplastics**
Epoxies	**Phenolics**	**Polyester**	**Polyimides**	**PPS, PEEK**
• Most popular • 80% of total composite usage	Cheaper Lower viscosity Easy to use High temp usage	Cheap Easy to use Popular for general applications at	High temperature application 300^{o}C Difficult to process Brittle	Good damage tolerance Difficult to process as high temp 300-400^{o}C is required

• Moderately high temperature • Comparatively expensive	Difficult to get good quality composites	room temperature		
• Low shrinkage (2-3%) • No release of volatile during curing	More shrinkage Release of volatile during curing	High shrinkage (7-8%)		
• Can be polymerized in several ways giving varieties of structures, morphology and wide range of properties	Inherent stability for thermal oxidation Good fire and flame retardance Brittle than epoxies	Good chemical resistance Wide range of properties but lower than epoxies Brittle Low T_g		
• Good storage stability to make prepregs	Less storage stability-difficult to prepreg	Difficult to prepreg		Infinite storage life but difficult to prepreg
• Absolute moisture (5-6%) causing swelling and degradation of high temperature properties • Also ultra violet degradation in long term	Absorbs moisture but no significant effect of moisture in working service range	Less sensitive to moisture than epoxies		No moisture absorption

The adhesion and contacts between different components in the composite systems have their great importance in many problems [20-22]17–19]. They can affect the performance as well as the life-time of the system. There is, therefore, a need to study the adhesion and contacts between layers that are relevant to composite organic photovoltaics and aerospace composite materials. The features of a typical composite system are summarized in Table 1.3.

Table 1.3 Feature of OPV and SiC - SiC systems with their several adhesion and contact challenges

Device	Structure	Materials	Problem	Methods

Thin-film Organic Electronics	Multilayered structure; More than three layers	Metal, polymer, ceramic and composite	Multi-body contact	Spin coating; Photoluminescence spectroscopy (PL); Raman spectroscopy; x-ray photoelectron spectroscopy; Nanoindentation; Finite element method; Atomic force microscopy
Air breathing Engines	Multilayered structure	Ceramic-ceramic composite	Multi-body	Finite element method, Materials Selection

1.2 Objectives

There is a need to develop affordable approaches to materials development for improved air transport and to harness solar energy for the generation of electricity in rural/urban areas of Africa and the world. These will be explored in this project using Silicon Carbide fiber in Silicon Carbide Matrix Composites (SiC-SiC CMC's) to protect air breathing engines used in the aerospace industry and bulk heterojunction (BHJ) organic solar cells that have the potential to significantly reduce the cost of solar cells to levels that are affordable to people especially in rural/urban areas of Africa.

The potential of such systems has also been enhanced by the recent improvements in the efficiencies of BHJ solar cells to approximately 8% [23]. However, there are still some concerns: the long-term stability of the BHJ solar cells and SiC-SiC composites, especially in the presence of oxygen and water vapor in the atmosphere. There is also the potential to further improve the OPV device efficiencies by promoting improved charge transport through increased adhesion and contact across the layers in BHJ solar cells.

1.3 Scope of This Work

The objective of this study is to explore the potential role of pressure, adhesion and contact in the design of interfaces in composite structures that can promote improved charge transport across BHJ solar cells and the efficiency in adopting SiC/SiC composites in protecting air breathing machines in the aerospace industry. Pressure-assisted lamination will be explored as a method for improving the contacts between layers in BHJ solar cells. The contacts will be modeled by considering the deformation and adhesion around dust particles (or voids) that are present in the clean room environment. Initial efforts will be made to relate the contacts to the current-voltage behavior of OPV devices.

This thesis is divided into seven chapters. The background and introduction is presented in chapter one, the relevant literature on Composite Materials for Aerospace application, BHJ photovoltaic cells and device physics is reserved in chapter two. Models for the prediction of contacts are then presented in chapter three. These include analytical and numerical models of contact between layers that are relevant to BHJ solar cells, and PDMS (optical adhesive) packages that can limit the access of water vapour and oxygen into the BHJ solar cells. The predictions from the models are correlated with previously reported experimental results in Chapter Three. The influence of annealing and pressure on nano- and micro- morphology, polymer chain alignment and current-voltage behavior are presented in Chapter Four.. The use of hybrid materials (both organic-inorganic materials for photovoltaic cells are presented in Chapter Five. Chapter Six presents the application composite materials for aerospace applications before presenting the salient conclusions from this work and suggestions for future work in Chapter Seven.

1.4 References

[1] C. W. Tang, S. A. Vanslyke, "Organic Electroluminescent Diodes", *Applied Physics Letters*, **51**, 913 (1987).

[2] L. S. Hung, C. W. Tang, M. G. Mason, "Enhanced electron injection in organic electroluminescence devices using an Al/LiF electrode", *Applied Physics Letters*, **70**, 152 (1997).

[3] C. W. Tang, S. A. Vanslyke, C. H. Chen, "Electroluminescence of Doped Organic Thin-Films", *Journal of Applied Physics*, **65**, 3610 (1989).

[4] H. Jiang, Y. Zhou, B. S. Ooi, Y. Chen, T. Wee, Y. L. Lam, J. Huang, S. Liu, "Improvement of organic light-emitting diodes performance by the insertion of a Si3N4 layer", *Thin Solid Films*, **363**, 25 (2000).

[5] D. Liu, C. G. Zhen, X. S. Wang, D. C. Zou, B. W. Zhang, Y. Cao, "Enhancement in brightness and efficiency of organic electroluminescent device using novel N,N-di(9-ethylcarbaz-3-yl)-3-methylaniline as hole injecting and transporting material", *Synthetic Metals*, **146**, 85 (2004).

[6] Y. Shirota, Y. Kuwabara, H. Inada, T. Wakimoto, H. Nakada, Y. Yonemoto, S. Kawami, K. Imai, "Multilayered organic electroluminescent device using a novel starburst molecule, 4, 4', 4 "-tris (3-methylphenylphenylamino) triphenylamine, as a hole transport material", *Applied Physics Letters*, **65**, 807 (1994).

[7] S. A. VanSlyke, C. H. Chen, C. W. Tang, "Organic electroluminescent devices with improved stability", *Applied Physics Letters*, **69**, 2160 (1996).

[8] L. S. Hung, C. H. Chen, "Recent progress of molecular organic electroluminescent materials and devices", *Materials Science & Engineering R-Reports*, **39**, 143 (2002).

[9] B. W. D'Andrade, M. E. Thompson, S. R. Forrest, "Controlling exciton diffusion in multilayer white phosphorescent organic light emitting devices", *Advanced Materials*, **14**, 147 (2002).

[10] V. E. Choong, S. Shi, J. Curless, C. L. Shieh, H. C. Lee, F. So, J. Shen, J. Yang, "Organic light-emitting diodes with a bipolar transport layer", *Applied Physics Letters*, **75**, 172 (1999).

[11] D. G. Ma, C. S. Lee, S. T. Lee, L. S. Hung, "Improved efficiency by a graded emissive region in organic light-emitting diodes", *Applied Physics Letters*, **80**, 3641 (2002).

[12] F. W. Guo, D. G. Ma, "White organic light-emitting diodes based on tandem structures", *Applied Physics Letters*, **87**, 173510 (2005).

[13] G. Schwartz, M. Pfeiffer, S. Reineke, K. Walzer, K. Leo, "Harvesting triplet excitons from fluorescent blue emitters in white organic light-emitting diodes", *Advanced Materials*, **19**, 3672 (2007).

[14] M. Strukelj, R. H. Jordan, A. Dodabalapur, "Organic multilayer white light emitting diodes", *Journal of the American Chemical Society*, **118**, 1213 (1996).

[15] C. W. Tang, "Two-layer organic photovoltaic cell", *Applied Physics Letters*, **48**, 183 (1986).

[16] G. Yu, J. Gao, J. C. Hummelen, F. Wudl, A. J. Heeger, "Polymer Photovoltaic Cells - Enhanced Efficiencies Via a Network of Internal Donor-Acceptor Heterojunctions", *Science*, **270**, 1789 (1995).

[17] T. Edwards **"**Composite Materials Revolutionize Aerospace Engineering*", INGENIA*, Issue 36 September 2008

[18] P. D. Mangalgiri *"*Composite materials for aerospace applications", *Bull. Mater. Sci.*, Vol. 22, No. 3, May 1999, pp. 657-664. © Indian Academy of Sciences.

[19] N. V. Nayak, "Composite Materials in Aerospace Applications", *International Journal of Scientific and Research Publications,* Volume 4, Issue 9, September 2014 1 ISSN 2250-3153

[20] R. E. Baier, E. G. Shafrin, and W. A. Zisman, "Adhesion: Mechanisms that assist or impede it," *Science*, vol. 162, no. 3860, pp. 1360-1368, Dec. 1968.

[21] E. M. Liston, L. Martinu, and M. R. Wertheimer, "Plasma surface modification of polymers for improved adhesion: a critical review," *Journal of Adhesion Science and Technology*, vol. 7, no. 10, pp. 1091-1127, Jan. 1993.

[22] R. Maboudian, "Critical review: Adhesion in surface micromechanical structures," *Journal of Vacuum Science & Technology B: Microelectronics and Nanometer Structures*, vol. 15, no. 1, p. 1, Jan. 1997.

[23] B. Sorensen, Renewables energy: Its physics, engineering, use environmental impacts, economy and planning aspects" Elsevier Science-Chapter 4 (2004).

Chapter 2

Literature Review

2.0 Introduction

The ever increasing energy demand and for faster transportation means due to world economic and trade purposes of the world is still mostly stilled by non-renewable energy sources, materials limitations resulting in an increased emission of greenhouse gasses and a growing shortage of fossil energy resources. The emission of these gases, with CO_2 as largest contributor, is altering the energy balance of the climate system with unforeseen consequences for the planet.[1,2] and therefore it is of utmost importance to change the materials for energy from inorganic silicon panels to organic bulk heterojunctions (BHJ composites) and aircrafts production using aerospace composite materials.

2.1 Composite Materials in Aerospace Applications

Composite materials for aerospace applications are an important considerations for faster transportation, fuel conservation and environmental considerations in the 21st century. The use of composite materials provides a much better means of air travels because for example the composite's strength-to-weight ratios far outweighs that of metals [3]. The reduction in weight leads to increased fuel economy and lower emissions due to the fact that plastics require minimal joining points, have improved efficiencies in aerodynamic performance and the reduced cost in their manufacturing [3]. Due to the drive for more efficient aerospace jet engines, operating

temperatures are also being driven higher and higher. As a result, the structural components in the hot section of the engine, typically composed of metal superalloys, are beginning to reach their temperature limits, even with thermal barrier coatings (TBCs) providing additional high temperature capabilities. For this reason, there is a shift towards using silicon-based ceramic matrix composites (CMCs) for these structural components [3-5].

2.1.1 Properties and applications of aerospace composite Materials

Materials used in the aerospace industry falls into the general category of materials: Ceramics, metals, polymers, inorganic glasses and composites. Ceramics have high melting points compared to polymers and metals and also have high strength and favorable thermal expansion response that make ceramics a reliable choice of material for aerospace application. However, the high degree of brittleness and the susceptibility to fracture failure often makes ceramics an inconvenience choice for structural applications. The strengths of metals and polymers reduce at high temperatures though polymeric materials are able to withstand much lower temperatures. Composites are a class of materials that combine two or more materials with significantly different structure and composition. Common examples of composites include fiber reinforced plastics, reinforced concretes, vinyl coated steel, etc. Currently, improvements in polymer materials research and the discovery of resins as matrices in polymer based composite when mix with carbon fibers (reinforcements with high strength and stiffness) has produced reliable structural material for complicated designs in the manufacturing of modern aviation vehicles. These developments have necessitated the large scale application of advanced composites in the design and manufacturing of military equipment across the world. The state-of-the-art launch vehicles and missiles, small and big civil aircrafts, satellites, helicopters are demonstrations of the impact of composite materials as well as the potential for application in other fields [5].

Aerospace systems manufacturing using polymers has been in long existence as about one third of the structural components are made from polymer based composites reinforced with advanced fibers. These types of materials have largely been adopted in military aircraft developments especially in radomes, fins, wings and control surfaces. The amounts of polymers (up to 15%) are somehow restricted in the construction of commercial air transport though this trend is fast changing. [5]. There are also developments in which the entire aircraft is made from composite materials though for small air vessels. These clearly show that, non-metallic materials are comparable to the well-known and improved metallic alloys including Ti, Al-Li, Al-Zn and Al-Cu [4-6]. In addition to these, the unique characteristics of composites have largely influenced and also introduced complex design possibilities, analyses and fabrication improvements in the aircraft industry. Much more, the concurrent availability of computational modeling technologies, coupled with improved methods of processing and fabrications, and the use of numerical simulations have greatly minimized the challenges that earlier plagued the industry and have led to substantial growth in the use of composites in aircraft structures.

Table 2.1 Composite features of aerospace structure [5]

Requirement	Applicability	Effect
Light-weight	All aerospace programme	• Semi-monocoque construction * Thin-walled-box or stiffened structures • Use of low density materials: * Wood * Al-alloys * Composites • High strength/weight, High stiffness/weight
High reliability	All space programmes	Strict quality control • Extensive testing for reliable data • Certification: Proof of design
Passenger safety	Passenger vehicles	Use of fire retardant materials • Extensive testing: Crashworthiness
Durability-fatigue and corrosion degradation: Vacuum Radiation Thermal	Aircraft Spacecraft	Extensive fatigue analysis/testing * Al-alloys do not have a fatigue limit!!! • Corrosion prevention schemes • Issues of damage and safe-life, life extension • Extensive testing for required environment • Thin materials with high integrity
Aerodynamic performance	Aircraft Reusable	Highly complex loading

	spacecraft	• Thin flexible wings and control, surfaces * Deformed shape-Aeroelasticity * Dynamics • Complex contoured shapes * Manufacturability: N/C Machining; Moulding
Multi-role or functionality	All aerospace programmes	Efficient design • Use: composites with functional properties
Fly-by-wire	Aircrafts, mostly for fighters but also some passenger a/c	* Structure-Control Interactions * Aero-servo-elasticity * Extensive use of computers and electronics * EMI shielding
Stealth	Specific military aerospace application	Specific Surface and Shape of aircraft Stealth coatings!!
All-weather operation	Aircraft	Lightning protection, erosion resistance

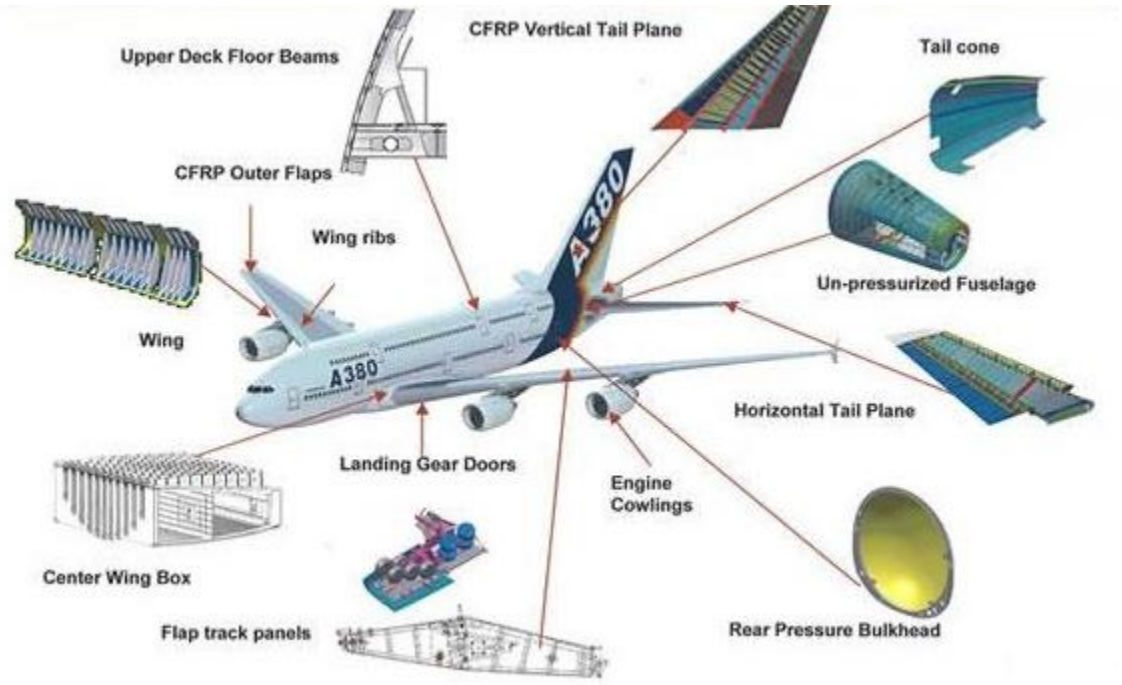

Figure 2-1 Composite Features of an aircraft A380 [7]

2.2 Solar Cells and Composite Materials

One source of renewable energy that is abundantly available is solar radiation. There is ~174 petawatts of energy in the uppermost part of the atmosphere with about 30% reflecting back to space. The land masses, atmosphere and the oceans absorb about 4 million exajoules annually whereas the amount that reaches the earth's surface alone is more than all the non-

renewables resources including coal, natural gas, uranium and oil over a year period. This energy from the sun can be converted to electrical energy as well as thermal energy for water heating. The conversion of the sun energy into electrical energy can be made possible using photovoltaics or solar cells. [8].

Therefore, a solar cell or photovoltaic cell is a solid state device that uses photovoltaic effects to convert the energy from the sun directly into electricity. The photovoltaic effect is the amount of voltage or current generated in materials when exposed to light. The charges generated build up the voltage between the electrodes through the transfer of the electron between the different bands.

The photovoltaic cells behave commonly like any other solid state devices made from semiconductors, such as integrated circuits and transistor as well as diodes. They indicate the basic source of power generation of the photovoltaic system. These semiconductors and their associated solar cells span different materials and different structures to be able to extract the optimum power at the minimum cost possible. [9].

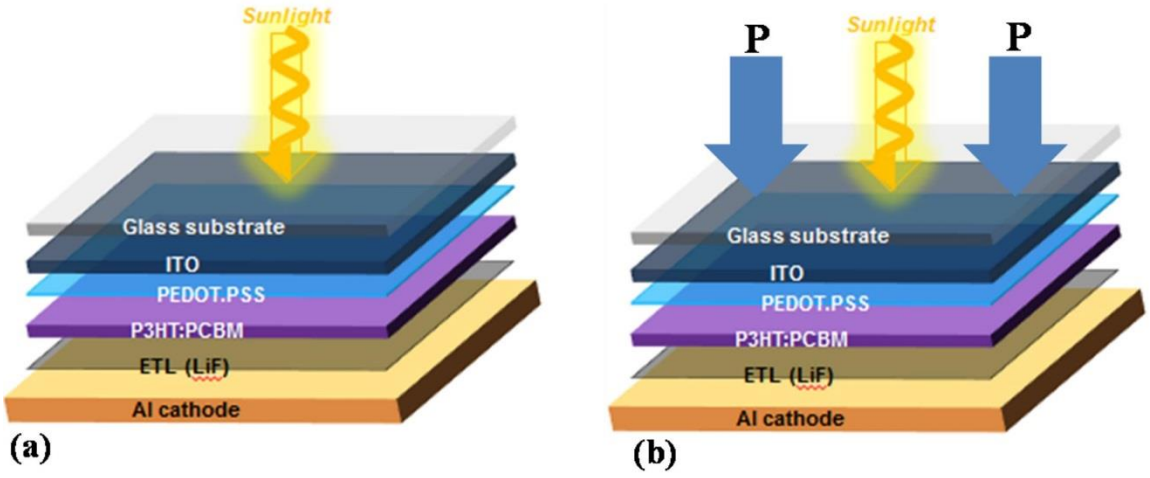

Figure 2.2 Organic photovoltaic cell layered structures

2.2.1 Types of solar cells

Solar cells have been produced from different materials with different performance efficiencies and costs. Generally, highly efficient solar cell should possess materials that have desirable characteristics with the spectrum of light from the sun which is main energy source. Currently, there are two broad types of solar cells including the inorganic and organic solar cells.

2.2.2 Inorganic Photovoltaic Cells

Since the development of the first crystalline silicon solar cell by Chapin, Fuller and Pearson in 1954, the majority of solar cells nowadays are based on silicon. Monocrystalline silicon solar cells has reached efficiencies of up to 25% (14 -17% in production) [8]. However, much energy is required for their production which makes these solar cells expensive. This class of solar cells is by far the most wide spread and efficient.

The main material used is Silicon (Si); and the most prevalent material for solar cells is crystalline Silicon (***c-Si***). This class is also subdivided into two groups:

The monocrystalline solar cells are made up of single-crystal wafers. The orientations of the unit cells are the same throughout the crystal. Monocrystalline Silicon is often made using the *Czochraslski* crystal growth process. They are produced by saw-cutting the wafers from silicon crystals are known to be the most advanced and efficient solar cell technologies They have efficiencies ranging from 20 – 30% though the processes are complicated and a bit expensive compared to the other technologies. [9].

Polycrystalline solar cells are also produced from recrystallized silicon usually from the top-cuts of the monocrystalline silicon. The ingots are saw cut into wafers for the production of the cells.

It is relatively cheaper to produce polycrystalline solar cells because the manufacturing processes are simple. However, cells from multicrystallline cells usually have low efficiencies, 12-15%.

Thin film solar cells can also be produced from inorganic materials by depositing one layer on another using a substrate. Due to the significantly reduced amount of materials needed, thin films solar cells tends to reduce the cost of production. All the film materials are usually very good absorbers of light and common among them are: Copper Indium Gallium Selenide (CIGS), amorphous silicon, cadmium Telluride, etc. The thin films for may form a heterojunction for example in CdTe/CIS or p-i-n junctions in amorphous silicon solar cells. These thins films usually have tin oxide as the transparent conducting anode and a metal layer as the back contact cathode layer. Many of the thin films are deposited using chemical vapour deposition, sputtering and hot wire technologies

2.2.3 Organic Photovoltaics cells

A promising class of thin film solar cells is based on organic materials, the so-called organic photovoltaic cells. This relatively new field can be divided into three subclasses; small molecule, dye-sensitized, and polymer-based organic solar cells.

Small molecule solar cells are fabricated by thermal evaporation of the active material. Control of the deposition processes gives easy access to different device architectures [10]. However, the vacuum based deposition technique needed for the production of this class of solar cells may prevent low cost, high throughput fabrication techniques and large area applications.

O'Reagan and Grätzel in 1991 produced the dye-sensitized solar cell (or Grätzel cell, **Figure 2.3**) [11] and consists of a donor material (the dye, often ruthenium based) attached to a mesoporous TiO_2 network which also acts as the acceptor material [11]. An electrolyte (usually I^-/I_3^-) regenerates the dye and is responsible for the hole transport to the appropriate electrode.

Efficiencies up to 11.2% have been obtained using this type of solar cell. A major advantage of dye-sensitized solar cells over both other organic counter parts is that no exciton diffusion is required. Charge separation takes place immediately after excitation of the dye due to direct contact with the TiO_b acceptor. The use of a liquid electrolyte to regenerate the dye hereafter is one of the main disadvantages of this class due to inherent stability problems associated with encapsulation of a liquid. Researchers are currently looking for ways to substitute the liquid electrolyte with a solid in this class of organic solar cells. [12]

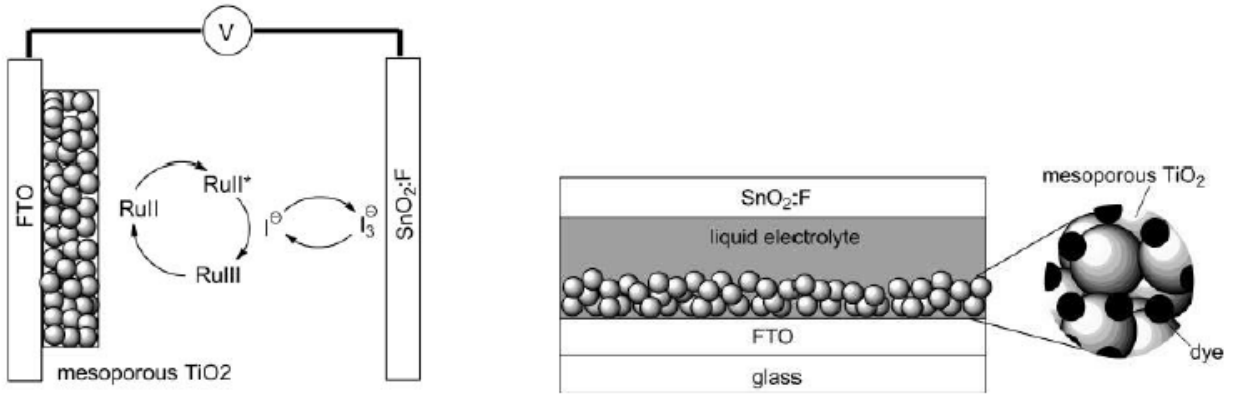

Figure 2.3: *Left: the working principle of a Grätzel cell; upon absorption of light the ruthenium(II) dye is excited and undergoes charge transfer to the TiO_2 resulting in a ruthenium(III) complex. This is regenerated by the I_3-/I- electrolyte couple by transferring the hole to the counter electrode. Right: a schematic representation of a Grätzel cell.[12]*

Organic photovoltaic (PV) cells also uses the phenomenon of charge separation when two materials surfaces are brought together to form an interface. Materials which are grouped as n-type and p-type semiconductors when brought together form P-N junctions. There also exists heterojunctions and bulk heterojunctions that are formed between semiconductors or semiconductor-metal junctions.

Organic photovoltaics, especially, Bulk Heterojunction (BHJ) Solar Cells have dominated in the various research reports in the past few years. [13]. The main advantage of

organic photovoltaic cells over their inorganic and other organic counterparts is that the organic materials comprising the active layer can be solution processible and provides alternatives for reduced cost of deposition. Common techniques adopted in organic solar cell fabrications include spray coating, doctor blading, inkjet printing, spin coating and roll-to-roll production which allows fast and cheap production and also accessible for large area applications [14]. Furthermore, these cells are light-weight and flexible. Materials usage is also greatly reduced because the organic materials have high absorption coefficient and therefore can absorb most of the light leading to enhanced photo and charge generations in polymer solar cells.

However, compared to the traditional inorganic solar cells a big disadvantage up to now is their rather low efficiency and limited lifetime and efforts to overcome these disadvantages are currently under intense study by research groups and companies. [15-17]. Organic solar cells currently produce efficiencies of 10-12% and these are due to several reasons. OPV materials with optimized energy levels, improved charge mobilities in the active layer, reduced recombination possibilities and efficient charge generation are key factors to consider when selecting materials for efficient OPV fabrication. The unfavorable nano- and micro-morphologies of the active layer can adversely affect the efficiency of the BHJ solar cells. There also exists the lack of understanding of the structures of the chemical make-up of the materials blended to form the active layer in addition to their complicated micro- and nano- morphological relationships [18-21]. This thesis seeks to offer reliable techniques to study the micro- and nano-morphology of some polymer blends used in OPV fabrication and their relationship with interfacial contacts and adhesion energies between the thin films.

2.3 Organic Photovoltaic Device Physics

2.3.1 Charge generation and transport

The photoactive layers of organic solar cells when exposed to electromagnetic radiation absorb light and electrons move from the HOMO to the LUMO of the p-type material. To achieve greater efficiency in photon collection from the sunlight, the emission spectrum of the sunlight must match the absorption spectrum of the photoactive layer. This means that, organic active layers should be physically thin but optically thick to maximize the absorption of light from the incident radiation.

Excitons (electron/hole pairs) are the main source of charge carriers in the organic solar cells and their creation is a major step in the conversion of light energy to electrical energy. These charge carriers are photogenerated through the dissociation of excitons at electron donor/acceptor by electron transfer between the donor and acceptor of a photoactive layer, with the assistance of extra energy supply by the absorbed photon. The photogenerated carriers are then separated as holes diffused towards the positive large work function (ϕ) anode electrode, while the electrons diffuse towards the negative small work function (ϕ) cathode electrode without recombination. Charge carrier recombination is one of the major factors that limit the power conversion efficiency of organic solar cells.

Also, mobility (μ) or charge carrier drift is another important property of the active layer and is defined as the charge carrier drift velocity $\boldsymbol{v}$ per unit field $\boldsymbol{E}$ of a semiconductor, given by the expression:

$$\mu = {|v|}/{E} \tag{2-1}$$

The mobility for electrons and holes are both positive and the electrical conductivity is the combination of the product of concentration of charge carriers and charge mobilities. This is given in the expression:

$$\sigma = (n_e \mu_e + p_h \mu_h) \tag{2-2}$$

where $\boldsymbol{\mu_e}$ is the mobility of electrons, $\boldsymbol{\mu_h}$ that of the holes and e is the electronic charge. The $\boldsymbol{p_h}$ and $\boldsymbol{n_e}$ are the charge carrier concentrations of holes and electrons. The power-law temperature dependence $\boldsymbol{T^n}$ for mobilities is weak, and the pronounced $\boldsymbol{T}$ dependence of the conductivity is due principally to the dependence of the electron and hole concentrations on the temperature [22].

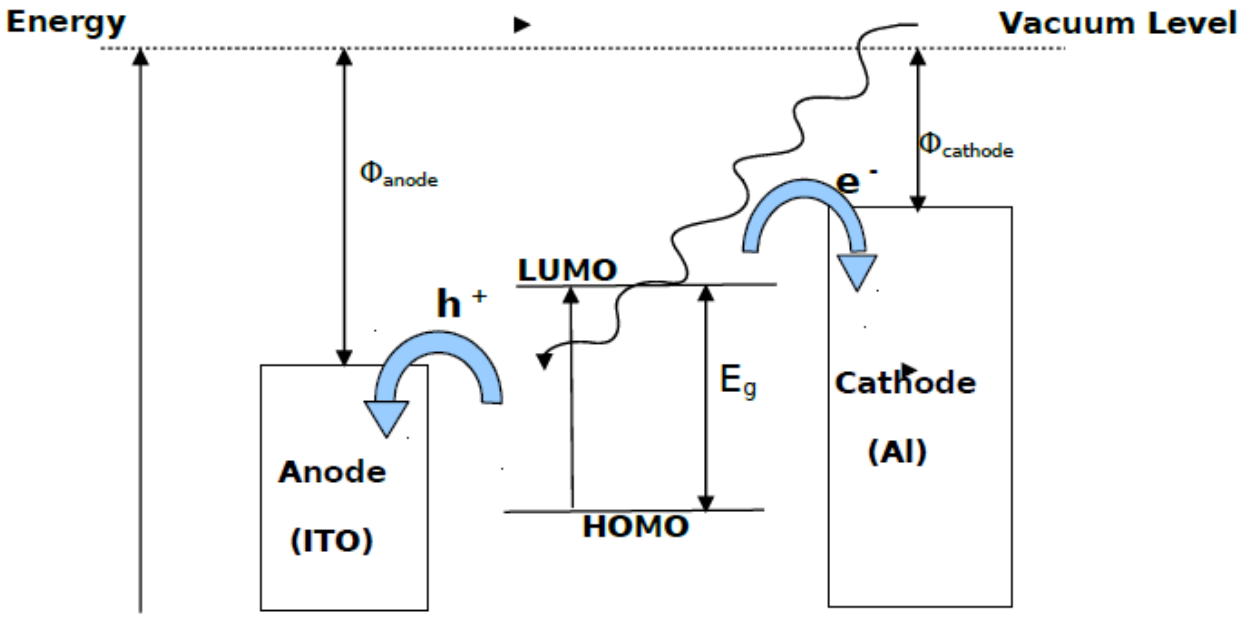

Figure 2.4 *Schematic representation of the operation of organic photovoltaic cells*

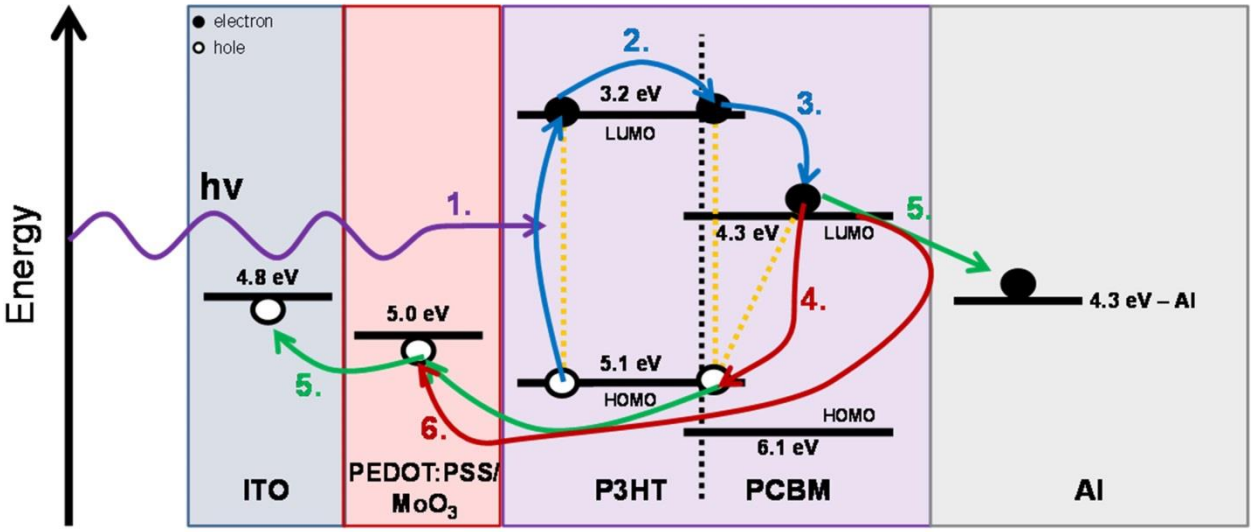

Figure 2.5 *Photophysical processes inside a conventional organic photovoltaic (OPV) device: (1) photon absorption by donor forms the exciton; (2) exciton diffuses towards donor-acceptor interface; (3) electron is transferred to acceptor (germinate pair formation); (4) germinate pair recombination may occur; (5) free electron and free hole may transfer to respective electrodes; (6) bimolecular recombination of free carriers may occur. [22]*

2.4 Solar cell parameters with emphases on organic photovoltaics

Organic solar cell performance can be determined by measuring current-voltage (*I-V*) characteristics in the dark and under illumination. A proper working device shows a diode character when measured under a varied bias voltage. The parameters to calculate the power conversion efficiency can be measured when the solar cell is illuminated under conditions resembling the Sun's irradiation (1000 W/m^2). These conditions are defined as AM 1.5 which is the solar spectrum on a clear sunny day with the incoming light at an angle of 42° with the Earth's surface [25].

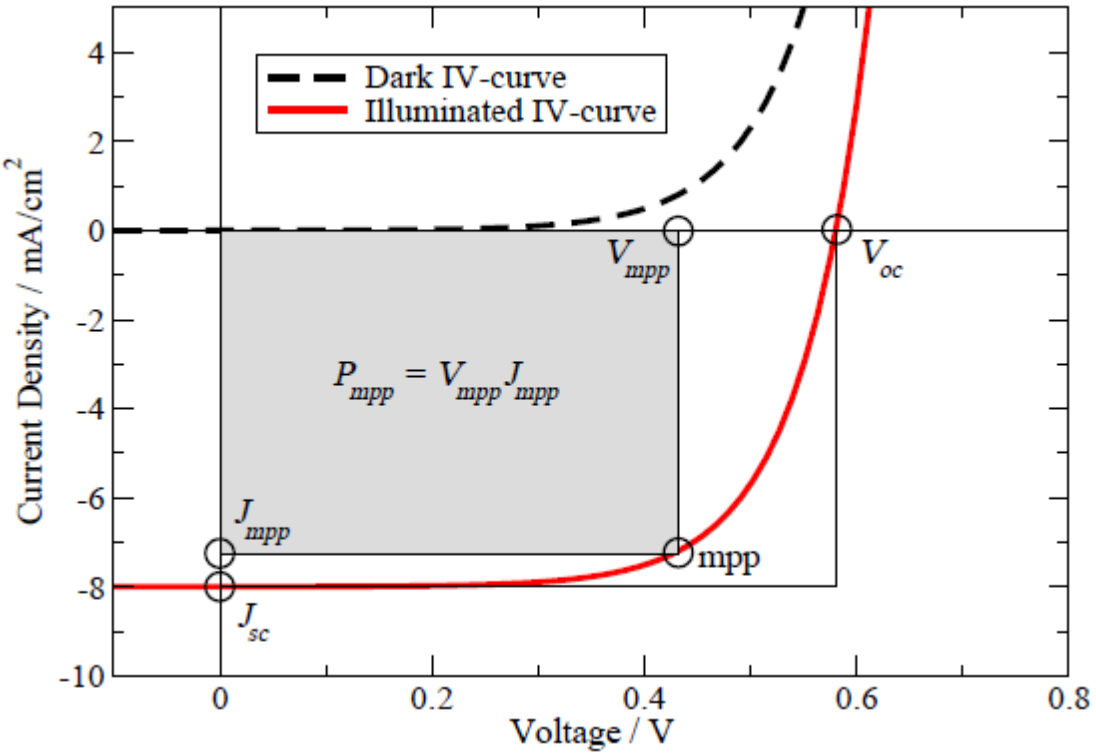

Figure 2.6 *Typical Current Density-Voltage Characteristic of an Organic Solar Cell (Adapted from Ref. [3])*

Quite a number of key parameters can be obtained directly from the current-voltage curve of the solar cell. (**Figure 2.6**): The short circuit current density (I_{sc}), defined as the current at zero voltage, the open circuit voltage (V_{oc}), which is the voltage when no current flows, and the maximum power point (MPP), this is the point where the product of current and voltage is maximal. An important value to determine the quality of a solar cell is its fill factor (FF), which is the ratio of the actual maximal obtained power (I_{MPP} x V_{MPP}) divided by the power given by the product of I_{sc} and V_{oc}. The fill factor depends on series and parallel resistance of the device which is *inter alia* influenced by layer thickness, balance of charge transport and quality of the electrode interfaces. [26, 27] Present highly efficient organic solar cells reach fill factors of around 0.70.

$$FF = \frac{P_{\max}}{V_{oc} \times I_{sc}} = \frac{V_{\max} \times I_{\max}}{V_{oc} \times I_{sc}} \tag{2-9}$$

The main characteristic of the performance of a solar cell is the power conversion efficiency η which can be calculated as follows, where PIN is the incident light power density.

$$\eta = \frac{V_{oc} \times I_{sc}}{P_{in}} FF \tag{2-10}$$

The short circuit current density (I_{sc}) depends on the number of absorbed photons which are converted to electrical current. It is therefore correlated to the incident light intensity, absorption properties, and generation, transportation, and collection of charges [28]. The open circuit voltage (V_{oc}) on the other hand is correlated to the difference between the highest occupied molecular orbital (HOMO) of the donor material and the lowest unoccupied molecular orbital (LUMO) of the acceptor material [29]. However, the actual value is lowered by recombination processes at the donor/acceptor interface and at the electrode interfaces. The exact origin of these recombination losses is still under investigation [30-32]. In silicon-based solar cells, the current density, I_L, under photon illumination is given by [33]:

$$I_L = I_s \left(e^{qv/nKT} - 1 \right) - I_{ph} \tag{2-11}$$

where I_S is the saturation current density, V is the applied voltage, q is the elementary charge, T is the temperature, K is Boltzmann's constant, n is the ideality factor and I_{ph} is the photogenerated current density. For an ideal silicon based solar cell, $I_{ph} = I_{sc}$ at the applied voltage. Open circuit voltage occurs when $I_L = 0$. By solving equation (2.11) using the fact that $I_L = 0$, the open circuit voltage is given by:

$$V_{oc} = \left(\frac{nKT}{q} \right) \ln \left(\frac{I_L}{I_S} + 1 \right) \tag{2.12}$$

where , $\frac{I_{sc}}{I_s} = \frac{I_{sc}}{I_s}$ is the short circuit current, and is the saturation current.

According to Koster et al. [34] and [35], the open circuit voltage and short circuit current of organic solar cells is given by:

$$V_{oc} = \frac{E_g}{q} - \frac{KT}{q} \ln\left[\frac{(1-P)\gamma N_c^2}{PG_b}\right] \tag{2-13}$$

and

$$I_{sc} = ne\mu E \tag{2.14}$$

where E_g is the energy gap, N_c is the effective density of states, G_b is the generation rate of the bound electron-hole pairs, P is the dissociation probability of a bound electron-hole pairs into charge carriers, and γ is the Langevin recombination constant. The energy gap is the energy difference between the highest occupied molecular orbital HOMO level of the donor and the lowest unoccupied molecular orbital LUMO level of the acceptor [36]. The *n* is the density of charge carriers, *e* is the elementary charge, μ is the mobility and *E* is the electric field.

Additional tools to determine the quality of a solar cell are its quantum efficiencies, which define the efficiency of photon to electron conversion at a certain wavelength. One distinguishes between the external quantum efficiency (EQE) and the internal quantum efficiency (IQE). The external quantum efficiency is defined by the ratio of collected electrons to the incident photons, whereas the internal quantum efficiency defines the ratio of the conversion of absorbed photons to electrons. It has been predicted by calculations that efficiencies of ~11% for single junction organic solar cells and ~15% for organic tandem solar cells are possible if materials with the right electrical and optical properties are used and an optimal morphology is formed [37,38] . However assumptions have been made with respect to both donor and acceptor which with the

development of new materials can turn out to be outdated. A good example is the absorption of the acceptor which in the calculation was assumed to be negligible. As already addressed above, the absorption of the acceptor can be important especially in small band gap materials. Therefore even higher efficiencies are expected to be within range for organic photovoltaics.

2.5 Materials

2.5.1 Donor material, the conjugated polymer

About four decades ago in 1977, research on the semiconducting properties of conjugated organic polymers started. The organic polymers were found to be conductive when the conjugated polymers were chemically doped. [39, 40]. These conjugated materials consist of alternating single and double carbon-carbon bonds. The mutual overlap between the pz orbitals of the carbon atoms results in delocalization of the π-electrons in extended molecular orbitals along the backbone. The intrinsic semiconductor behavior of conjugated polymers comes from the behavior of the delocalized π-electrons and charge generation and transport mechanisms differ greatly from the inorganic materials which rely on the concept of free charges and band conduction. In organic semiconductors, holes and electrons hop from one localized state to another in the organic semiconductor. This process is called hopping [41]. Compared to inorganic materials; this hopping process results in relatively low charge carrier mobility. The strength of these organic materials lies in applications where ease of processing is combined with moderate transport performance requirements.

The first generation of bulk heterojunction organic solar cells was mainly based on mixtures of poly[2-methoxy,5-(2'-ethyl-hexyloxy)-*p*-phenylene vinylene] (MEH-PPV) or poly[2-methoxy,5-(3',7'-dimethyloctyloxy)-*p*-phenylene vinylene] (MDMO-PPV) as donor and PCBM

as acceptor material, Figure 2.10. The highest reported efficiencies reached 3%, but the polymers were limited by a non-optimal light absorption and showed rather low mobilities [42, 43]. The PPVs were followed by polythiophenes, in particular regioregular poly-3-hexyl-thiophene (RR-P3HT), which still remains the work horse material and benchmark in the field at present. After extensive research on methods to optimize the processing conditions of the active layer efficiencies of up to 5% were reached [44, 45].

In the past years, a variety of conjugated copolymers have been synthesized and tested as donor material in bulk heterojunction organic solar cells [46]. These polymers consist of electron rich and electron poor units, like *e.g.* fluorenes, thiophenes, carbazoles or benzothiazoles. By combining these building blocks the optical and electronical properties of the resulting polymer can be controlled.

However, to prepare highly efficient organic solar cells with these polymers remains challenging; in many cases the obtained morphology is not optimal [47-49]. Nevertheless, several of these materials helped to further improve the efficiency of organic solar cells [50, 51]. Recently, record efficiencies of 7.4% were reported for solar cells made from PTB7 [52]. The highest certified efficiencies claimed up to date were set by Solarmer in December 2009 at 7.9% (NREL 0.1 cm^2), Heliatec and I_{app} in April 2010 at 7.7% (Fraunhofer Institute for Solar Energy Systems ISE in Freiburg, 1.1 cm^2) with the current world record by Konarka in December 2010 at 8.3% (NREL 1.0 cm^2).

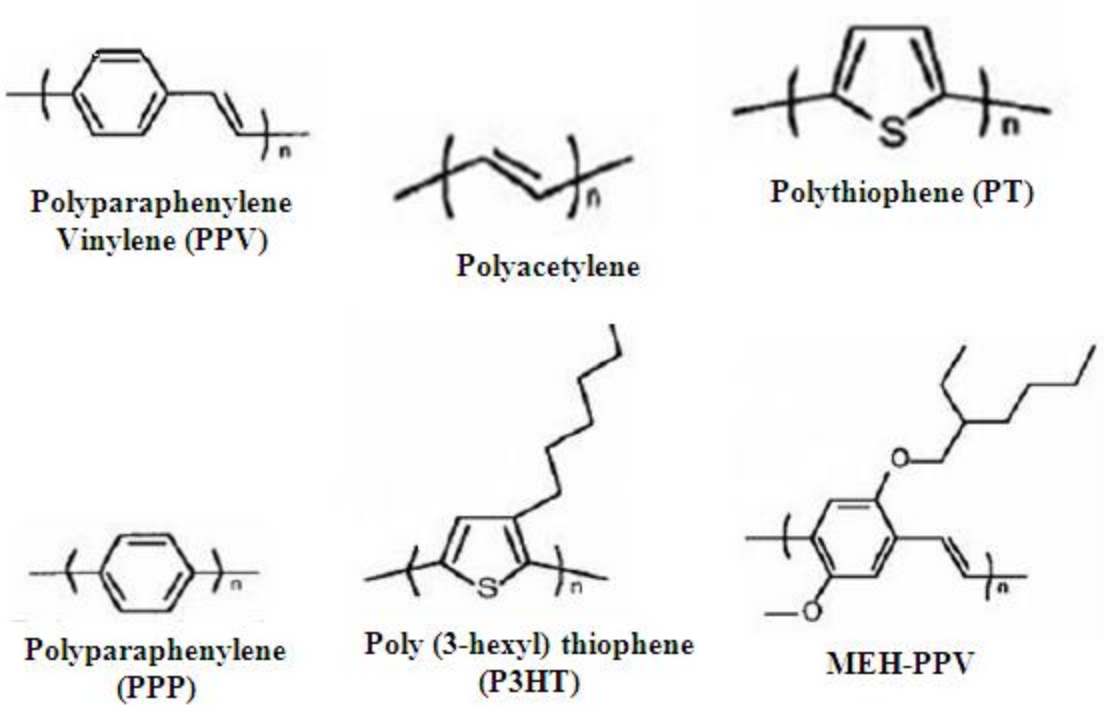

Figure 2.7 *Structures of polymers used in Organic photovoltaic cells.*

2.5.2 Fullerenes (acceptors) for photovoltaic applications

Over the years many different polymers were developed and used as donor material in organic solar cells, but as acceptor material PCBM is still widely used. Although many attempts were made to replace PCBM by other fullerene derivatives, it still remains the n-type material of choice in organic solar cells. It shows similar crystal-packing as C60, which results in a higher electron mobility, compared to other fullerene derivatives [53]. However, [44] PCBM **(Figure 2.8(a))** is more and more replaced by [54] PCBM **(Figure 2.8(b))** which has similar electronic properties but a significantly higher absorption coefficient especially at shorter wave lengths. This improved absorption can complement the light absorption of small bandgap polymers which have improved absorption towards longer wavelength, but lack absorption in the blue-green part of the solar spectrum [55-57].

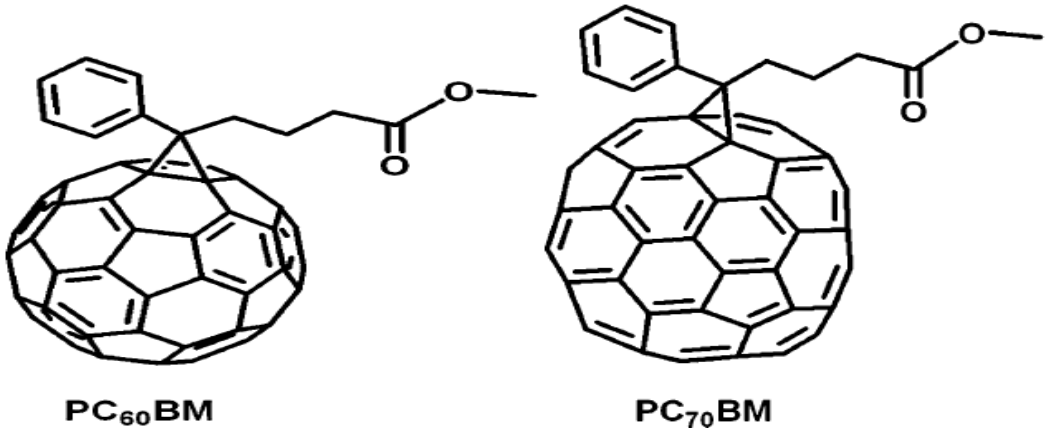

Figure 2.8 *Fullerenes for Photovoltaic applications (a) $PC_{60}BM$ and (b) $PC_{70}BM$*

2.5.3 Improving the fullerene acceptor for use in bulk heterojunction architectures

Improving the device performance compared to benchmark devices comprising P3HT:PCBM either consists of raising the efficiency through improved current or voltage obtained from a cell or by extending the lifetime of the cell. Methods to increase the lifetime of devices mostly consist of improving their resistance to both air and water, or by increasing the thermal stability of the active layer morphology.

Because current is hard to influence through structural manipulation and depends strongly on processing conditions, the most straight forward method to improve the performance of the solar cell is through its open circuit voltage. The most direct method to influence the V_{oc} of donor-acceptor based OPV devices is to alter the offset between the LUMO of the donor and the LUMO of the acceptor. The open circuit voltage is ultimately limited by the difference between the HOMO of the donor and the LUMO of the acceptor. The offset between the LUMO of the donor and LUMO of the acceptor enables electron transfer and the offset between the HOMOs drives the hole transfer, but these offsets also result in a loss in V_{oc}. Studies into P3HT:PCBM cells indicate that, an offset for the LUMO-LUMO greater than the 0.3 - 0.5 eV is required for

the transfer of electrons that may give an open circuit voltage of only 0.6 V, much smaller than the 2 eV band gap of P3HT. When a lower LUMO-LUMO offset is obtained, there is greater possibilities of device efficiency increases, especially with P3HT:PCBM cells.

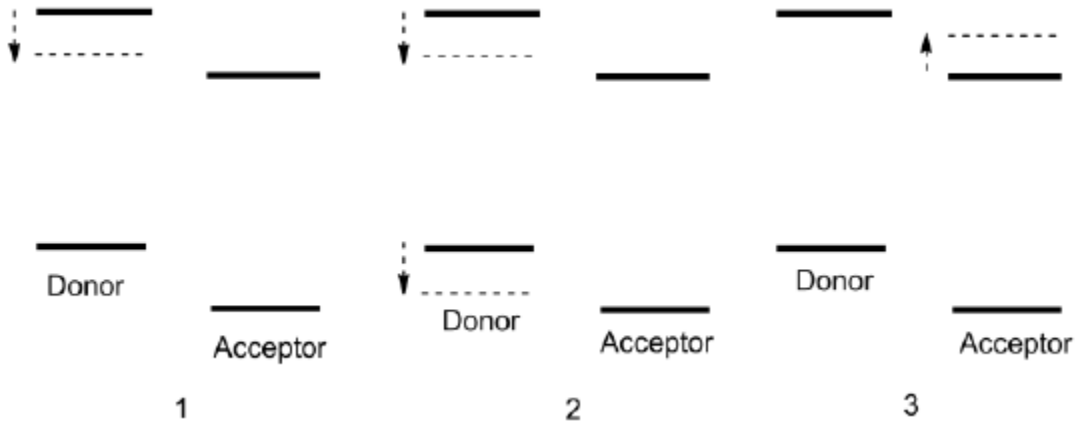

Figure 2.9:1-3 *Three possible methods for lowering the LUMO-LUMO offset between donor and acceptor; 1. Lowering the LUMO of the donor, 2. Lowering both the LUMO and the HOMO of the donor, 3. Raising the LUMO of the acceptor. [Bouwer Thesis]*

2.5.4 Pressure, Adhesion and Contacts Theories

The application of pressure to improve interfacial surface contatcts in thin film organic solar cells and light emitting devices are guided by the basic contact theories to help in the characterization of adhesion and contacts in layered structures [59-62]. These theories consider two elastic spheres in contact and relate the normal load to the displacement. They also provide methods for the estimation of the adhesion energies from adhesion force data measured from experimental techniques, for example atomic force microscopy (AFM).

The classical Hertzian contact theory [63] assumed that there is no adhesion between two elastic spheres in contact. The Johnson-Kendall-Roberts (JKR) model [60] describes the contact between soft materials with short range, strong adhesion forces, and large tip radii. In contrast,

the Derjaguin-Muller-Toporov (DMT) model [61] applies to adhesion between stiff materials with long range, weak adhesion forces, and small tip radii.

In this regime, the adhesion forces can be estimated by the following two limiting cases: the Johnson-Kendall-Roberts (JKR) model [61], which applies in the case when the adhesion forces are short range compared to the elastic deformation they produce (i.e. compliant material with strong adhesion), and the Derjaguin-Muller-Toporov (DMT) model [62], which describes well the case of long range surface forces with a Hertzian geometry (i.e. stiff materials, weak adhesion forces). Intermediate between the JKR and DMT models, the Maugis-Dugdale (MD) model [63] proposes an analytical solution.

Figure 2.10 compares the interaction forces (per unit area) for the Hertz, JKR and DMT models with the realistic interaction. In the Hertz model, there is no attractive force, only hard wall repulsion at contact. The JKR model represents short range adhesion, which can be described by a delta function with strength γ and short-range contact zone. The DMT model represents a long-range surface force, which has a Hertzian contact profile, with an additional external load as attractive forces. For realistic interactions, the integral of the force-distance attractive well, for example Lennard-Jones potential, corresponds to the work of adhesion, i.e. adhesion energy, γ.

Figure 2.11 [66] presents the force-distance relation in the Maugis-Dugdale (MD) model, which is an analytical solution in the intermediate regime between the JKR and DMT models. Maugis [62] used a Dugdale square well potential to approximate the interaction potential in reality. In this interaction, a constant adhesive stress (force per unite area) σ_0 acts between the surfaces over a range of δ_t.

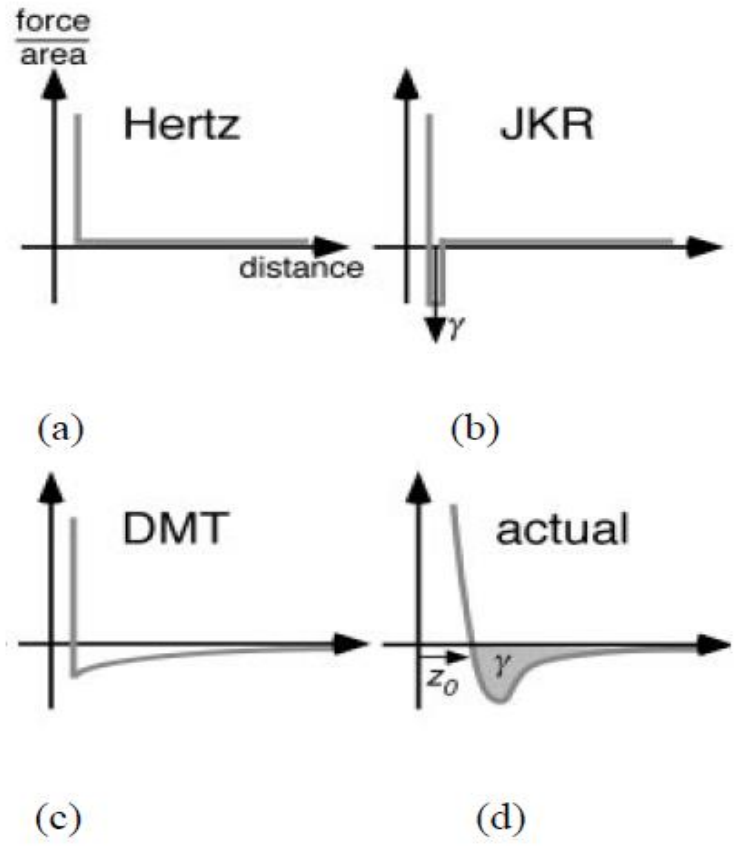

Figure 2.10 *Interaction forces (per unit area) for (a) Hertz model, (b) JKR model, (c) DMT model and (d) actual interaction [58].*

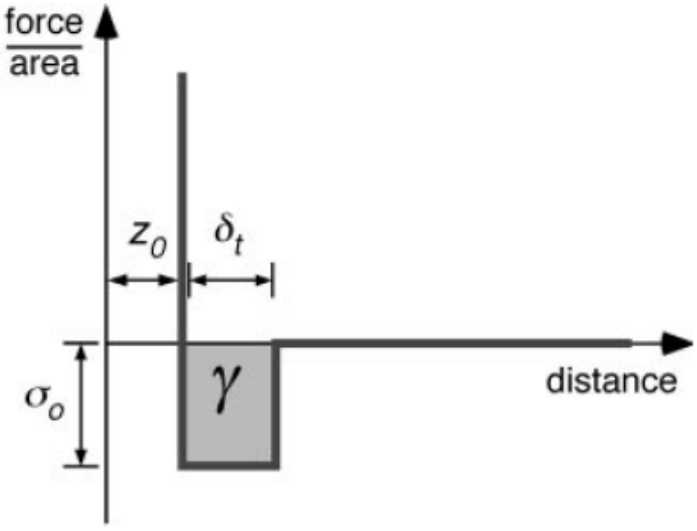

Figure 2.11 *Schematic of Dugdale model used by Maugis [63].*

To select the appropriate model, Maugis [66] defined a transition parameter, which is given by:

$$\lambda = 2\sigma_o \left(\frac{R}{\pi \kappa^2 \gamma} \right)^{1/3} \tag{2-15}$$

where γ is the adhesion energy per unit area; R is the combined radius given by $R = R_1 R_2 / (R_1 + R_2)$, where R_1 and R_2 are the radii of the two spheres, respectively; κ is the combined elastic modulus for two spheres in contact, which is given by, $\kappa = 4/3\left[(1-\nu_1)^2 / E_1 + (1-\nu_2)^2 / E_2 \right]$ where $E_1$and E_2 are the elastic moduli of the two spheres, ν_1 and ν_2 are the Poisson ratios of the two spheres, respectively. By choosing σ_o to match the minimum adhesive stress of a Lennard-Jones potential with equilibrium separation distance z_o, it follows that $\delta_t = 0.97 z_o$. The JKR model applies when $\lambda > 5$.The DMT model applies when $\lambda < 0.1$. The MD model applies for the intermediate values of λ.

In the non-zero adhesion cases, the negative critical load at which the surfaces of two spheres separate, when being pulled apart, was defined as pull-off force or adhesion force. For the two extreme cases, it is given in JKR and DMT theories by:

$$F_{JKR} = \frac{3}{2} \pi \gamma R \tag{2-16}$$

$$F_{DMT} = 2\pi \gamma R \tag{2-17}$$

In the MD model, two equations are needed to relate the contact radius, α, and the contact force, F:

$$\frac{\lambda \hat{a}^2}{2}\left[\sqrt{m^2-1}+(m^2-2)\cos^{-1}\left(\frac{1}{m}\right)\right]+\frac{4\lambda^2 \hat{a}}{3}\left[\sqrt{m^2-1}\cos^{-1}\left(\frac{1}{m}\right)-m+1\right]=1 \qquad (2\text{-}18)$$

$$\hat{F}=\hat{a}^3-\lambda \hat{a}^2\left[\sqrt{m^2-1}+m^2\cos^{-1}\left(\frac{1}{m}\right)\right] \qquad (2\text{-}19)$$

where and are two dimensionless parameters defined by:

$$\hat{a}=\frac{a}{\left(\frac{\pi\gamma R^2}{\kappa}\right)^{1/3}} \qquad (2\text{-}20)$$

$$\hat{F}=\frac{F}{\pi\gamma R} \qquad (2\text{-}21)$$

and the parameter m represents the ratio between the contact radius, a, and an outer radius, c, when the gap between the sphere surfaces reaches δ_t, i.e., where the adhesion no longer takes place. However, the above equations are difficult to use, since there is not a single expression relating only α and F. Equations (2-18) and (2-19) need to be solved simultaneously by letting *m* vary appropriately between limits, which depend upon λ. Furthermore, in the usual case with experimental measurements, such as AFM force measurement, the value of λ is an unknown. The relation for the pull-off force must be determined through α iterative technique [64]. Carpick

et al.[63] [34] proposed that the relation between contact radius a and the contact radius at zero load α_0 can be described by a generalized equation

$$\frac{a}{a_o} = \left(\frac{\alpha + \sqrt{1 - F/F_{ad}}}{1+\alpha} \right)^{2/3} \tag{2-22}$$

where F_{ad} is the general adhesion force. Where α=1, it corresponds exactly to the JKR case, and when α=0, it corresponds exactly to the DMT case. They showed that for intermediate cases, for which 1<α<0, the generalized transition equation corresponds very closely to solutions provided by Maugis using λ:

$$\lambda = -0.924 \ln\left(1 - 1.02\alpha\right) \tag{2-23}$$

Equation (2-10) was later modified by Pietrement and Troyon [64] through fitting to be

$$\lambda = -0.913 \ln\left(1 - 1.018\alpha\right) \tag{2-24}$$

Applying Equation (2-21) to adhesive forces gives:

$$\hat{F}_{ad} = \frac{F_{ad}}{\pi \gamma R} \tag{2-25}$$

They also determined empirical equations supplying direct conversion equations between parameter α and $\bar{F}_{ad}$ by:

$$\hat{F}_{ad} = 0.267\alpha^2 - 0.767\alpha + 2.000 \quad (2\text{-}26)$$

The AFM force measurement measures F_{ad} with R and κ known, the adhesion energy can be calculated by solving the Equations (2-15), (2-24), (2-25) and (2-26).

This section reviews prior theories [60–63] for the characterization of the contact adhesive interactions. The theories provide methods to characterize the adhesion between two elastic spheres in contact. They can also be used to estimate the adhesion energies and pressure effects on the contact and void length ratios for the analytical modeling and also from atomic force microscopy (AFM) experiments.

2.6 Surface Roughness and Morphology Characterization

2.6.1 Atomic Force Microscopy

Using an atomic force microscope (AFM) (Digital Instruments Nanoscope IIIa AFM, Plainview, NY) in the tapping mode, it is possible to measure the roughness of a sample surface and morphology at a high resolution, to distinguish a sample based on its mechanical properties and in addition, to perform a microfabrication of a sample.

In *tapping mode*, the cantilever is driven to oscillate up and down at or near its resonance frequency by a small piezoelectric element mounted in the AFM tip holder similar to non-contact mode. However, the amplitude of this oscillation is greater than 10 nm, typically 100 to 200 nm. The interaction of forces acting on the cantilever when the tip comes close to the surface, van der

waals forces, interactions, electrostatic, etc. cause the amplitude of this oscillation to decrease as the tip gets closer to the sample. An electronic servo uses the piezoelectric actuator to control the height of the cantilever above the sample. The servo adjusts the height to maintain a set cantilever oscillation amplitude as the cantilever is scanned over the sample. A *tapping AFM* image is therefore produced by imaging the force of the intermittent contacts of the tip with the sample surface.

This method of "tapping" lessens the damage done to the surface and the tip compared to the amount done in contact mode. Additionally, there are significant less lateral forces in the tip-sample interaction in tapping mode over contact mode. Tapping mode is gentle enough even for the visualization of supported lipid bilayers or adsorbed single polymer molecules (for instance, 0.4 nm thick chains of synthetic polyelectrolytes) under liquid medium. With proper scanning parameters, the conformation of single molecules can remain unchanged for hours.

2.6.2 X-ray Photoelectron (XPS) and Ultra violet photoelectron spectroscopies (UPS)

X-ray photoelectron spectroscopy (XPS) and Ultra violet photoelectron spectroscopies (UPS) are surface-sensitive quantitative spectroscopic techniques that measure the elemental composition and the workfunction of metals and metal oxides at the parts per thousand range, empirical formula, chemical state and electronic state of the elements that exist within a material. The XPS and UPS spectra were collected from the spin coated PEDOT:PSS films, thermally evaporated silver films and electrochemical and ultra violet ozone oxidized silver films. This was done in a vacuum chamber that was pumped down to the base pressure ~10^{-8} mbar under excitation using a twin-anode Al *K-α* X-ray radiation source (*hv*~1.486keV) with an X-ray spot size of 15 μm and a spherical sector analyzer with multichannel detectors (Thermo Scientific, UK). During XPS, the samples were mounted on stainless steel stubs using double-sided adhesive tape. All of the XPS

data were corrected for sample charging during X-ray irradiation using adventitious hydrocarbon referencing: E_b(C1s) = 284.8 eV.

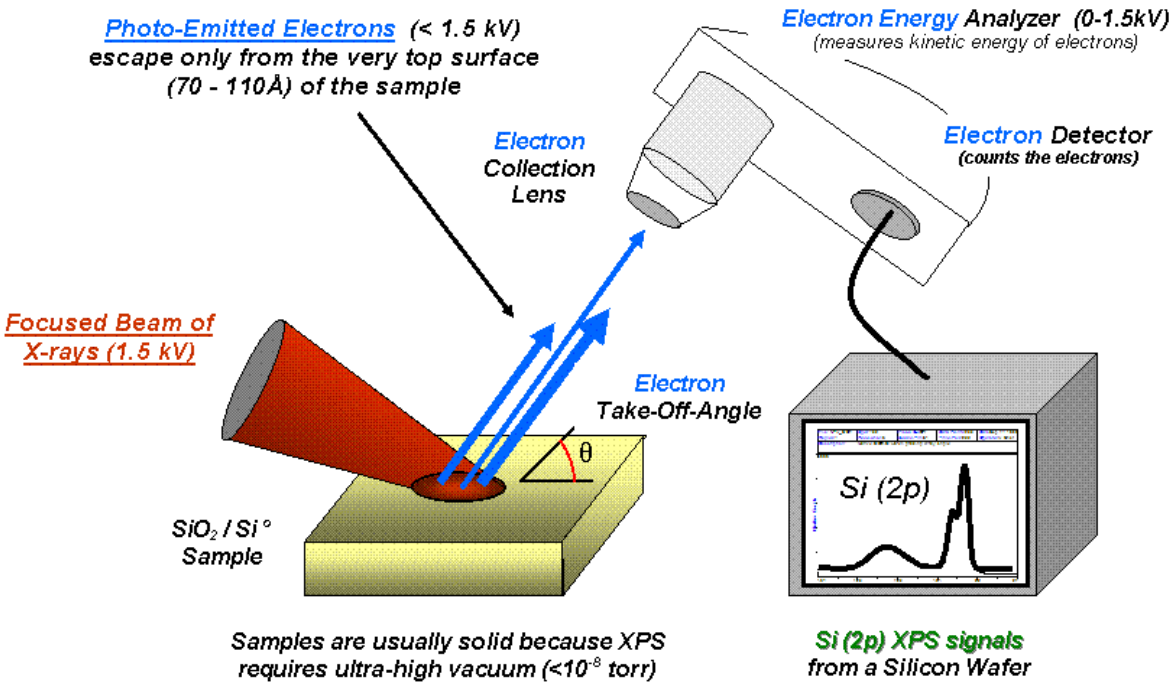

Figure 2.12 *Schematic representation of XPS and UPS techniques (Source: Wikipedia assessed on August, 2016 at 10:15 am*

2.7 Synchrotron light Source, Theory and Experiments

X-ray scattering techniques are of interest because they can provide information about bulk features across multiple length scales [65-67] based on whether small (SAXS) or wide (WAXS) angle X-ray scattering is utilized. Recently, several synchrotron facilities have developed simultaneous SAXS/WAXS measurement capabilities [67-70], simplifying the experience for users of these facilities as well as allowing for more efficient use of the beam time. Of particular interest is the combined SAXS/WAXS system at the X9 beamline of the National Synchrotron Light Source (NSLS) at Brookhaven National Lab due to its proximity to Rutgers University. Additionally, through the use of grazing incidence methods (GISAXS/GIWAXS), near-surface

features and buried interfaces can be studied as these techniques essentially become surface-sensitive [65,71]. This makes GISAXS and GIWAXS measurements particularly useful for organic thin films, in which the supramolecular and internal structures of these films can be studied using these respective techniques. Organic thin films have become a topic of great interest recently, particularly for their applications in organic optoelectronic devices (i.e., photovoltaics, electroluminescent devices, and thin film transistors). GISAXS and GIWAXS have become important research tools for the analysis of organic thin films and devices, particularly for conjugated polymers and polymer blends.

2.7.1 Theory of Operation

Small and wide angle X-ray scattering techniques have very similar underlying physical principles; the primary difference arises in the method of detection of SAXS and WAXS signals. As such, the principles of SAXS will be focused on here, but these principles are readily applied to WAXS as well.

2.7.2 Theoretical Basis

When X-rays of wave vector, k_0, interact with a sample, the X-rays will be reflected, absorbed, transmitted, or scattered from the sample. In reality, all of these processes will occur with the fraction of each of these processes summing to 1. Here, the primary focus is on scattering, and X-rays scattered from a material will have a new wave vector, k_s. The change in momentum that occurs as a result of the scattering process is given by q:

$$q = k_s - k_o \qquad \text{2-44}$$

Where the incident wave vector is given by:

$$k_o = \left|\bar{k_o}\right| = \frac{2\pi}{\lambda} \qquad 2\text{-}45$$

where λ is the wavelength of the X-rays and is typically in the range of 0.01 - 10 nm [65]. These processes are depicted in **Figure 2.13**. Typical SAXS experiments are performed in transmission mode, making this technique sensitive to bulk rather than surface structures [65].

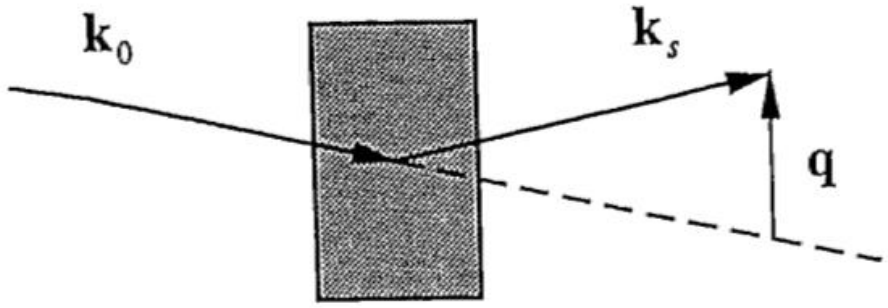

Figure 2.13 *Schematic of a generic elastic scattering process, an incident beam characterized by wavevector* $\mathbf{k_0}$ *penetrates into a sample and is scattered through angle 2Θ. The direction of the scattered beam is then given by* $\mathbf{k_s}$ *[65].*

If the only angle of interest is 2θ, then the expression for q can be given by [65]:

$$q = \frac{4\pi}{\lambda}\sin\theta \qquad 2\text{-}46$$

When electromagnetic radiation interacts with matter, one important factor to consider is the material's refractive index, *n*. For X-rays, this is given by [65]:

$$n = 1 - \delta + i\beta \qquad 2\text{-}47$$

where β represents the absorption component and is typically determined by the mass absorption coefficient, μ:

$$\beta = \frac{\mu\lambda}{4\pi} \qquad 2\text{-}48$$

and 1 - δ is the real part of the refractive index. δ, can be described by the electron density,

$$\delta = \frac{\lambda^2}{2\pi}\rho_e r_o \qquad 2.49$$

where r_o is the electron radius. The variation of n and ρ_e through a sample describe the real space structure of the sample, but the scattering intensity is usually measured in reciprocal space, in which case the scattering cross-section ($d\sigma/d\Omega$, which is scattered intensity per unit solid angle per incident flux) becomes important. The scattered intensity is given by [65]:

$$I_{\exp}(q) = \Phi TE \int \frac{d\sigma}{d\Omega}(q)\, d\Omega \qquad 2\text{-}50$$

where Φ is the incident photon flux, T is the transmission coefficient, E is the detector efficiency and Ω is the solid angle over which the detector collects the scattered photons.

2.7.3 Grazing Incidence

The x-ray scattering techniques described have all been for normal incidence, where the x-rays transmit through the sample completely. A different method of obtaining X-ray scattering measurements is by using grazing incidence, in which the incident angle (θ_o) is kept at no larger than a few degrees **(Figure 2.14)** [65]. There are two major differences between X-ray scattering under grazing incidence and X-ray scattering under normal incidence. First, penetration depth into the sample is limited since the x-rays now have to travel through more of the sample when at an angle, and the penetration depth decreases rapidly with decreasing incident angle. Additionally, penetration into underlying layers such as substrates can be limited based on total reflection. As θ_0 is decreased towards zero, θ_1, the angle at which the beam travels through the sample will no longer have any real components (based on Snell's law); thus, a critical angle θ_c can be defined where, if the incident angle is less than this value, there will be no (or minimal) penetration into the substrate:

$$\theta_c = \sqrt{2\delta_1} \qquad 2\text{-}50$$

where δ_1, is the real component of the refractive index, defined previously [65]. An additional effect observed in grazing incidence mode is that the intensities of reflected and scattered radiation at the surface and interface becomes measureable, allowing one to probe buried interfaces as well as near-surface structures. Grazing incidence X-ray scattering is particularly useful for thin film analysis, its surface sensitivity, and its ability to study features at buried interfaces within the sample [65, 71].

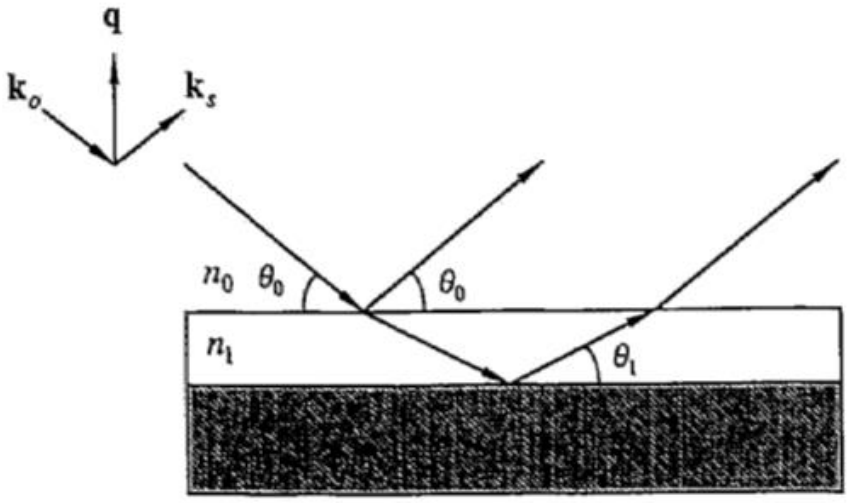

Figure 2.14 *In a grazing incidence experiment the beam incident upon the sample at angle Θ_o may be in general both partially transmitted through the interface and partially reflected. The transmitted beam is propagated at a grazing angle Θ_t with respect to the surface and may be reflected from other interfaces in the sample, such as the film/substrate interface illustrated here. In this cast the radiations reflected from the two interfaces interfere, yielding a distinctive pattern characteristic of the film thickness [65].*

2.7.4 Combined SAXS/WAXS Measurements at NSLS

The X9 beamline at the National Synchrotron Light Source (NSLS) at Brookhaven National Lab (BNL) was designed and constructed around 2006-2008 with the primary focus of SAXS/WAXS experiments [67]. The X9 beamline uses a unique SAXS/WAXS detector system that allows for

simultaneous acquisition of SAXS and WAXS data in a way differing from previous systems (described below). A general setup of the X9 beamline has the photon source called the mini-gap undulator (MGU) of length 360 mm with 23 x 14.5 mm periods and minimum gap separation of 3.3 mm, which provides a continuous spectrum having fundamental energy ~ 2 keV [80]. X-rays from the undulator enter the cryocooled double-crystal monochromator (DCM) to select the desired energy, then after passing through the DCM, monochromated X-rays are passed through a pair of 850 and 400 mm-long Kirkpatrick-Baez (KB) bimorph mirrors in order to horizontally and vertically focus the X-ray beam, respectively. The X-ray beam is then passed through 2 slits to define the beam size and divergence, followed by another pair of micro KB focusing mirrors to potentially reduce the beam size down to 10 μm; the beam enters a third pair of slits before finally striking the sample. After scattering from the sample, the scattered X-rays travel 3.4 m to the SAXS detector and the WAXS detector is placed at a wide enough angle to collect X-rays scattered at larger angles. A beam stop is placed before the SAXS detector to partially block the unscattered/forward-scattered X-rays. [68]

The WAXS detector is positioned off-axis from the direct beam such that the beam is not blocked, but X-rays scattered at wide angles can be detected [67]. One of the more recent advances in X-ray scattering is the use of Charged-Coupled Device (CCD) detectors to obtain 2D diffractograms. At the X9 beamline, a vacuum-compatible Kodak 4301E CCD sensor having 2084 x 2084 pixels (24 μm in size), custom-built by Photonic Science, is used for WAXS measurements. The detector must be vacuum compatible such that it can be placed in the vacuum chamber to receive a portion of the scattered beam [67, 68]. The WAXS detector has a layer of Gadox (Tb) phosphor on its surface to convert X-rays into visible photons. The phosphor is

shielded from ambient light by a black Kapton window, which still allows 98 % of the X-rays to be transmitted at 12 keV or higher [67].

The SAXS detector is a Mar 165 CCD detector, located 3.4 m from the center of the sample stage. As seen from **Figure 2-15 (d)**, there is overlap between the SAXS and WAXS detectors, specifically between ~ 0.12 - 0.2 $Å^{-1}$ [80]. The SAXS and WAXS data can potentially be combined automatically using software developed at the X9 beamline, and the data is calibrated using silver behenate [68]. Although simultaneous SAXS/WAXS measurements are very convenient, GIWAXS and GISAXS data at the X9 is usually collected sequentially to avoid shadowing of the WAXS detector in the GISAXS pattern as well as due to the difference in required exposure times for the separate measurements [67]. The WAXS detector is moved a few millimeters during the GISAXS measurements, which only takes moments to complete [67].

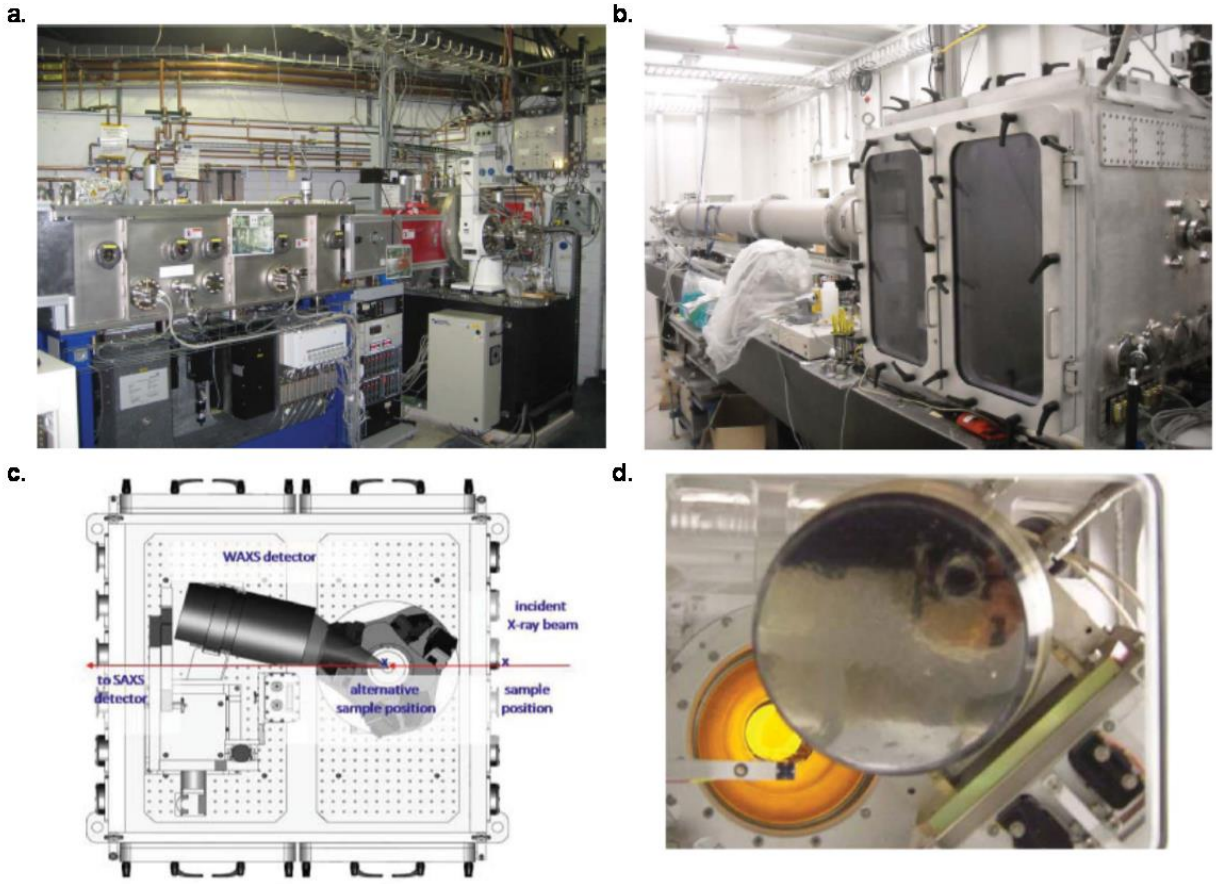

Figure 2.15 *(a) Photograph of the beamline optical components with the double-crystal monochromator (on the right) and the KB horizontal/vertical bimorph adaptive focusing mirrors (on the left). b) The long vacuum-compatible chamber of NSLS beamline X9 that contains both the SAXS (at the far end) and WAXS detectors (designed by Scott Coburn). c) Position of the WAXS and SAXS detectors relative to the X-ray beam. d) View from the X-ray beam in the direction of the detectors. This view indicates the overlapping region, which can be seen from the SAXS images. [68]*

2.7.5 GIWAXS/GISAXS Application in Organic Optoelectronic Materials

The field of organic optoelectronics has grown tremendously over the past several decades. Part of the success of this growing field has been the development and continuous improvement of conjugated (i.e., conducting) polymers, which can range from semiconducting to metallic. Several advantages of conjugated polymers include (but is not limited to): 1) they can be processed using low-temperature, solution-based techniques such as spin-coating; 2) they have

very large absorption coefficients, such that even ~ 100 nm of the polymer layer can be optically thick; and 3) they can form thin, flexible layers suitable for flexible electronics. These properties make conjugated polymers attractive for optoelectronic applications such as photovoltaics, light-emitting devices, and thin-film transistors. Two of the most common conjugated polymers used in optoelectronic applications - P3HT and F8BT, as well as one of the most common organic molecules blended with P3HT in photovoltaic applications, PCBM.

One of the major problems with these organic materials, however, is that they tend to have very low charge carrier mobilities (~ 10^{-4} $cm^2V^{-1}s^{-1}$) compared to inorganic, crystalline semiconductors (*c.f.* Si, with an electron mobility of ~ 1.5 x 10^3 $cm^2V^{-1}s^{-1}$). The mobility of these polymers can be improved by a variety of techniques, such as control of the polymer regioregularity (percentage of "head-to-tail" repeating units), molecular weight, and nanostructure. However, all of these techniques share a common effect of increasing the order, or the alignment of the polymer chains, in thin organic films. SAXS and WAXS, particularly in the grazing incidence mode (i.e., GISAXS and GIWAXS) are ideal to study the morphological changes in these organic thin films - on both the nanoscale and the mesoscale - in order to try to improve the mobility of conjugated polymer films.

2.7.5.1 Polymer Chain Alignment

It is well-known that the conductivity of conjugated polymer films is anisotropic, being dependent on the orientation of the polymer chain subunits. P3HT is a conjugated polymer that has been extensively studied for photovoltaic and transistor applications. Its conductivity depends on its regioregularity (which is the percentage of head-to-tail attachments of the hexyl side chains to the 3-position of the thiophene chains), its molecular weight, and its nanoscale structure. Using GIWAXS, two main orientations of the polymer chains have been identified:

"edge-on" and "face-on" alignment, as depicted in the insets of **Figure 2-16** [72-74]. These orientations are identified by the intensity of particular scattering peaks in the 2D GIWAXS contours. In particular, the lamella layer structure (side chains) give rise to (100) reflections, whereas the $\pi - \pi$ stacking (thiophene faces stacked on top of one another) give rise to (010) reflections [72-74]. From Fig. 2-16a, since the (100) peak is very strong along the vertical axis (the *q*z axis), it has been suggested that the lamella structures must be normal to the film, i.e. the edge-on orientation is probably dominant. In **Figure 2-16(a)**, the fact that the (010) peak is so disperse implies that even though the polymer chains are edge-aligned, there must be disorder in which direction (parallel to the substrate) the $\pi - \pi$ stacks are facing [72-74]. For **Figure 2.16(b)** however, the strong (010) peak in the *q*z direction suggests that the $\pi - \pi$ stacking is normal to the film, and the strong (100) reflections along the *q*|| direction supports the idea that the lamella are oriented parallel to the film; both of these reflections give evidence to the face-on orientation of the polymer chains [72-74]. This is the standard crystallographic notation for P3HT and will be used when discussing how to control polymer chain alignment. It is also important to note that the in-plane mobility (as confirmed by FET mobility measurements) is greater in the edge-on orientation of the polymer chains by ~ 3 orders of magnitude compared to the face-on orientation [72,73].

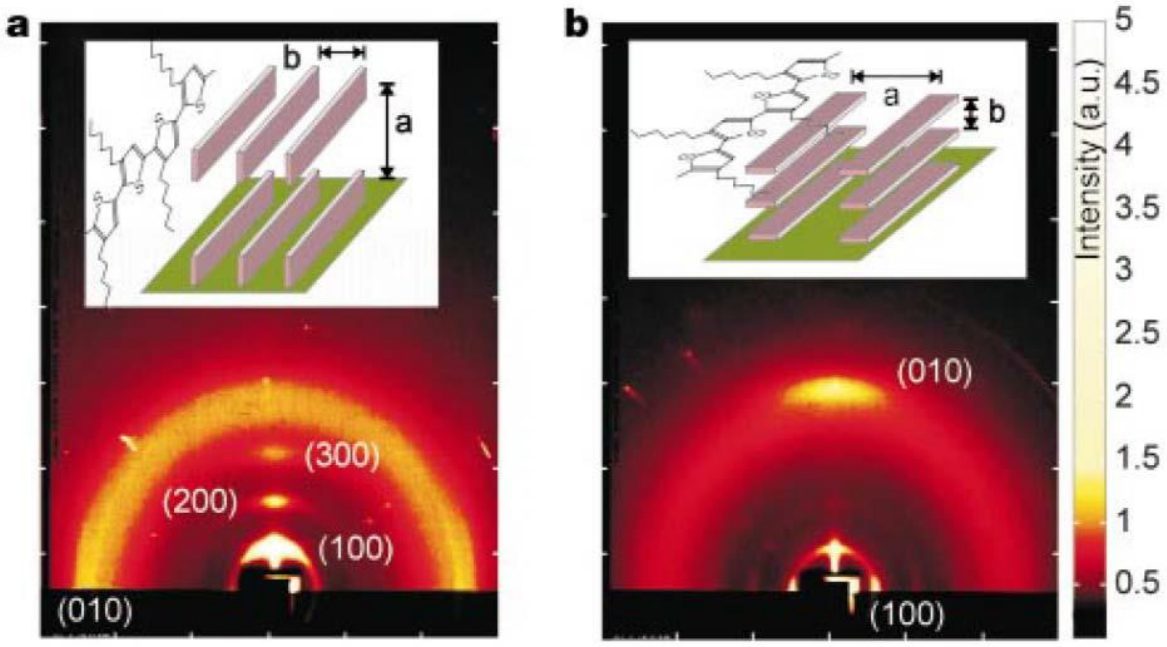

Figure 2.16 *Two different orientations of ordered P3HT domains with respect to the FET substrate.* ***a***, ***b****. The wide-angle X-ray scattering images are a color representation of the two-dimensional distribution of the Cu Kα X-ray intensity from spin-coated, 70 - 100 nm thick P3HT films with regioregularity of 96 % (**a**) and 81 % (**b**) on SiO_2/Si substrates. The vertical (horizontal) axes correspond to scattering normal (parallel) to the plane of the film. The insets show schematically the different orientations of the microcrystalline grains with respect to the substrate [72]*

2.7.5.2 Regioregularity-Induced

The preferential alignment of polymer chains has been shown to be dependent on the regioregularity of the polymer. In **Figure 2-16**, the P3HT samples were dynamically spin-coated onto FET substrates; **Figure 2-16(a)**, the P3HT films had 96 % regioregularity, and in **Figure 2-16(b)**, the films had 81% regioregularity [72]. This indicates that higher regioregular solutions of P3HT give preferential alignment of the (100) axis normal to the film (edge-on), and that lower regioregularity in solutions of P3HT give preferential alignment of the (010) axis normal to the film (face-on) [84]. Thus, high regioregularity gives rise to edge-on orientation, which also has mobility values around 0.1 cm2 V-1 s-1 [72].

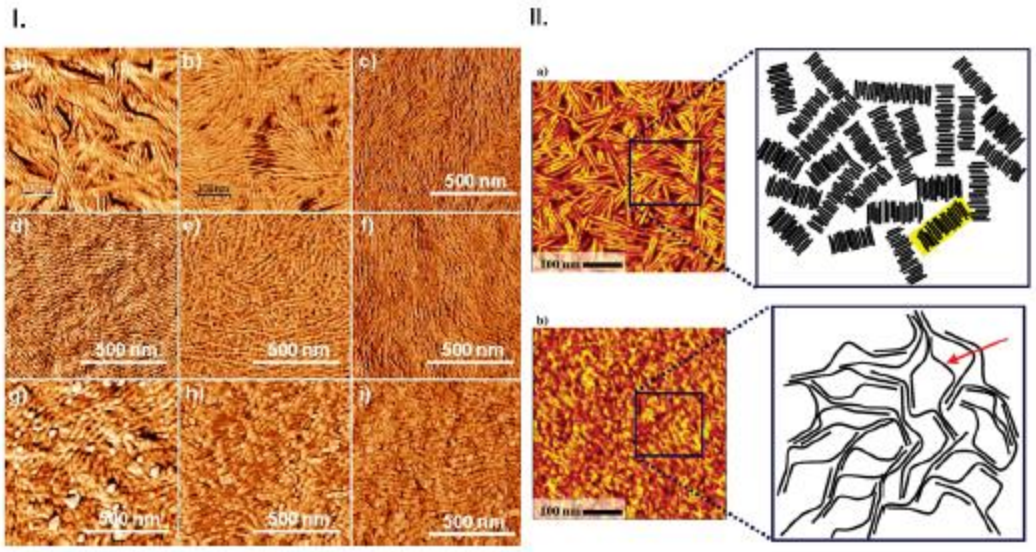

Figure 2.17 ***(i)*** *Tapping mode AFM images (phase contrast, 1 µm x 1 µm) of thin films of RR-P3HTs of various molecular weights in FET devices prepared by drop casting from toluene. Corrected weight average molecular weights in (a-i) were respectively equal to: 2.4, 4.8, 5.1, 7.0, 7.5, 11.8, 15.7, 17.3, and 18.4 kDa [82].* ***(ii)*** *Model for transport in low-MW (< 5 kDa)* ***(a)*** *and high MW (> 20 kDa)* ***(b)*** *films. Charge carriers are trapped on nanorods (highlighted in yellow) in the low-MW case. Long chains in high-MW films bridge the ordered regions and soften the boundaries (marked with an arrow) [73].*

2.7.5.3 Molecular Weight Dependence

In addition to regioregularity, the molecular weight of the polymer in solution before forming a thin film can affect the degree of polymer chain alignment, and ultimately carrier mobility. It has been shown by phase contrast atomic force microscopy (AFM) that low molecular weight (MW), highly regioregular (> 98 %) P3HT films tend to form nanofibril- or nanorod-like structures when deposited and annealed (**Figure 2.15**) [73,75]. However, AFM is extremely surface-sensitive, only very small areas can be imaged at one time, and due to the small dimensions and stickiness of the P3HT nanofibrils, new tips were required for every scan [75]. For these reasons, GISAXS and GIWAXS can be very beneficial techniques to determine the nanoscale structure and/or confirm data acquired through AFM.

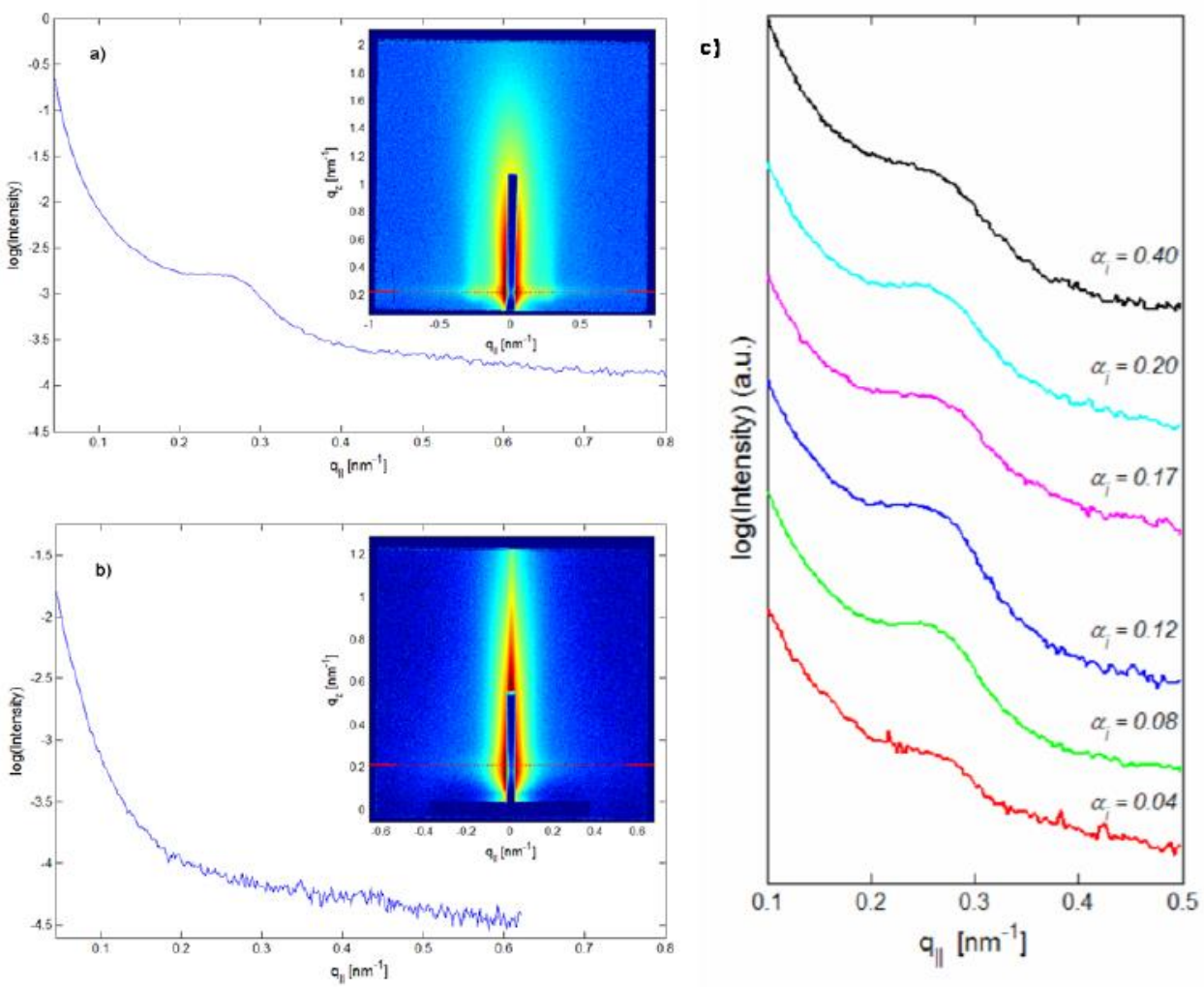

Figure 2.18 *GISAXS patterns for thin films of 7.0 kDa RR-P3HT prepared by casting from toluene (a) and chloroform (b) acquired at a critical angle (0.12°). (c) GISAXS patterns acquired for thin films of 7.0 kDa RR-P3HT at different angles of X-ray incidence. The GISAXS patterns were integrated over ±0.022 ° around critical exit angle (maximum of the Yoneda peak) and offset vertically for clarity. [75]*

Zhang *et al*. studied the periodicity of P3HT nanofibrils using GISAXS (**Figure 2.18**). Based on the hump that occurred around 0.2 - 0.3 nm^{-1} along *q*, the authors were able to determine the width of the nanofibrils [75]. However, since grazing incidence mode is known to be surface sensitive, this still did not help answer the question regarding whether the nanofibrils occurred throughout the P3HT film, or just at the surface. To investigate the thickness-dependence, Zhang *et al*. varied the incident angle from 0.04 ° to 0.40 °, and the hump did not change its shape/size

with changing incident angle (**Figure 2-16 (c)**) [75]. Using this method, a surface-sensitive technique such as GISAXS can be used to probe the bulk of thin films also. The authors also plotted the width of the nanofibrils, calculated from GIWAXS, versus the width of the nanofibrils measured from the AFM, and the data correlated very well (**Figure 2.17(d)**), indicating that GISAXS can be used to study nanoscale feature sizes similar to AFM, but can probe a much wider area due to the size of the incident beam. Klein *et al*. studied low and high MW P3HT films using 1D in-plane GIWAXS (**Figure 2.18 (a)** [73]. For low MW films, the (100) and (010) peaks were both present, indicating that there is both ordering of lamellar chains as well as the $\pi - \pi$ stacking present in the plane of the film (mixture of both edge-on and face-on orientations). The low MW films also had much sharper peaks than the high MW films, indicating that lower MW films have larger crystallites and less variation in their *d*-spacing compared with higher MW films. The higher MW films, however, did not show the (010) peak in the plane of the film, although the (100) was still present, indicating that for the high MW films, the face-on orientation was preferred [73].

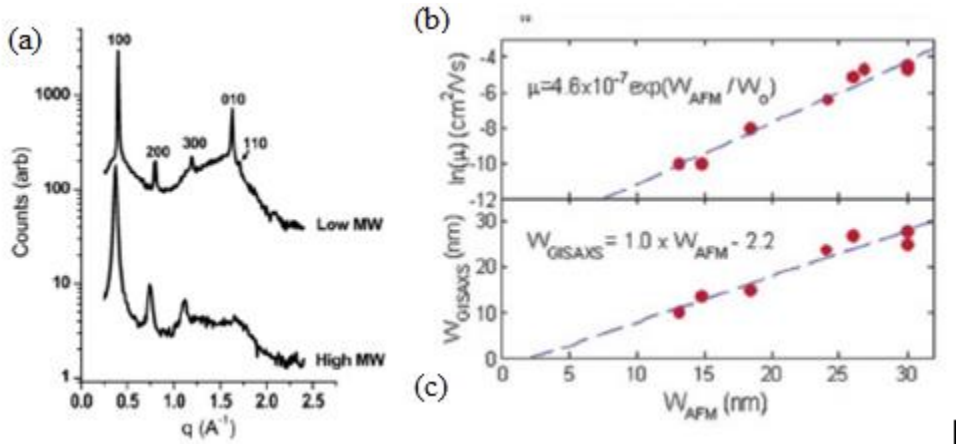

Figure 2.19 ***(****a) In-plane grazing incidence XRD data comparing low-MW films to high-MW films annealed films spin-cast from chloroform [80], (b-c) Linear correlation between GISAXS periodicities and nanofibril widths [75].*

2.8 References

[1] Parry ML, *Cambridge Univ Press, Cambridge, UK, and New York*, 2007

[2] S. Solomon, G. K. Plattner, R. Knutti and P. Friedlingstein, *Proc. Natl. Acad. Sci. U. S. A.* 2009, **106**, 1704

3] T. Edwards *Composite Materials Revolutionize Aerospace Engineering,* INGENIA Issue 36 September 2008

[4] P. D. Mangalgiri *Composite materials for aerospace applications,* Bull. Mater. Sci., Vol. 22, No. 3, May 1999, pp. 657-664. © Indian Academy of Sciences.

5] N. V. Nayak, *Composite Materials in Aerospace Applications,* International Journal of Scientific and Research Publications, Volume 4, Issue 9, September 2014 1 ISSN 2250-3153

6] F. Smith, *The use of composite in aerospace: past, present and future challenges,* Avalon Consultancy Services, www.avaloncls.com

7] The Atlas Group, http://theatlasgroup.biz/composite, accessed on 22nd January, 2016 (21:35 GMT)

[8] M. A. Green, K. Emery, Y. Hishikawa and W. Warta, *Prog. Photovoltaics,* 2009, **17**, 320

[9] Markvart, T. et al (1994), "Solar electricity" - John Wiley & Sons -

[10] J. Xue, B. P. Rand, S. Uchida and S. R. Forrest, *Adv. Mater*., 2005, **17**, 66

[11] B. O'reagan and M. Grätzel, *Nature*, 1991, **353**, 737

[12] U. Bach, D. Lupo, P. Comte, J. E. Moser, F. Weissörtel, J. Salbeck, H. Spreitzer and M. Grätzel, *Nature*, 1998, **395**, 583

[13] N. S. Sariciftci, L. Smilowitz, A. J. Heeger and F. Wudl, *Science,* 1992, **258**, 1474

[14] C. J. Brabec and J. D. Durrant, *MRS Bull*., 2008, **33**, 607

[15] H. Hoppe and N. S. Sariciftci: *Polymer Solar Cells*, S. R. Marder, K.-S. Lee (eds.): *Photoresponsive Polymers II.* Springer, Berlin/Heidelberg, 2008, **214**, 1

[16] B. C. Thompson and J. M. J. Frechet, *Angew. Chem. Int. Ed*., 2008, **47**, 58

[17] G. Dennler, M.C. Scharber and C.J.Brabec, Advanced Materials. 2009 21, 1323.

[18] Koster, C. J. A. et al (2006), Appl. Phys. Lett. 88, 2006, 693511

[19] Dennler, G. et al (2005), "Flexible, conjugated polymer-fullerene-based bulk heterojunction solar cells: Basics, encapsulation, and integration" - J. Mater. Res., Vol. 20, No.12

[20] Aldous, S. (2005), "How Solar Cells Work" How Stuff Works: http:// science.How stuff works.com/solar-cell1.htm

[21] Preuss, P. (2002), "An unexpected discovery could yield a full spectrum solar cell" Research News – Berkeley Lab. http://www.lbl.gov/Science-Articles/Archive/MSD-fullspectrum-solar-cell.html

[22] Poole, C. P. J. & Owens, F. J. (2003), "Introduction to Nanotechnology" – John Wiley & Sons Inc. Publication – ch. 5 Pp20 -22 ; 125-132

[23] Fonash, S. J. (2010), " Solar cell device physics" Pp 67-75

[24] Markvart, T. & Castafier, L. (2006), "Solar Cells- Materials, Manufacture and Operation"- Elsevier Ltd.-

[25] J. M. Kroon, M. M. Wienk, W. J. H. Verhees and J. C. Hummelen, *Thin SolidFilms*, 2002, 403, 223

[26] V. D. Mihailetchi, J. Wildeman and P. W. M. Blom, *Phys. Rev. Lett.*, 2005, **94** ,126602

[27] M. S. Kim, B. G. Kim and J. Kim, *ACS Appl. Mater. Interfaces*, 2009, **1**, 1264

[28] P. W. M. Blom, V. D. Mihailetchi, L. J. A. Koster and D. E. Markov, *Adv. Mater.*,2007, **19**, 1551

[29] L. J. A. Koster, V. D. Mihailetchi, R. Ramaker and P. W. M. Blom, *Appl. Phys.Lett.*, 2005, **86**, 123509

[30] V. D. Mihailetchi, L. J. A. Koster, J. C. Hummelen and P. W. M. Blom, *Phys. Rev.Lett.*, 2004, **93**, 216601

[31] L. J. A. Koster, E. C. P. Smits, V. D. Mihailetchi and P. W. M. Blom, *Phys. Rev. B*, 2005, **72**, 085205

[32] D. Veldman, O. Ipek, S. C. J. Meskers, J. Sweelssen, M. M. Koetse, S. C. Veenstra, J. M. Kroon, S. S. van Bavel, J. Loos and R. A. J. Janssen, *J. Am. Chem.Soc.*, 2008, **130**, 7721

[33] R. Steim, P. schilinsky, S. A. Choulis, C. J. Brabec, Sol. Energy Mater. Sol. Cells 93 (2009) 1963-1967

[34] L. J. A. Koster, V. D.Mihailetchi, R. Ramaker, P. W. M. Blom: Light intensity dependence of open-circuit voltage of polymer:fullerene solar cells. Appl. Phys. Lett. 86, 123509 (2005)

[35] F. C. Krebs, Organic Electron. 10(2009) 761-768

[36] F. C. Krebs, S. A. Gevorgyan, J. Alstrup: J. Mater. Chem. 19(2009) 5442-5451

[37] G. Dennler, M. C. Scharber, T. Ameri, P. Denk, K. Forberich, C. Waldauf and C. J. Brabec, *Adv. Mater.*, 2008, **20**, 579

[38] M. C. Scharber, D. Wuhlbacher, M. Koppe, P. Denk, C. Waldauf, A. J. Heeger and C. L. Brabec, *Adv. Mater.*, 2006, **18**, 789

[39] C. K. Chiang, C. R. Fisher, Y. W. Park, A. J. Heeger, H. Shirakawa, E. J. Louis, S. C. Gau and A. G. MacDiarmid, *Phys. Rev. Lett*., 1977, **39**, 1098

[40] H. Shirakawa, E. J. Louis, A. G. MacDiarmid, C. K. Chiang and A. J. Heeger, *J.Chem. Soc. Chem. Commun*., 1977, 578

[41] D. Hertel and H. Bassler, *ChemPhysChem*., 2008, **9**, 666

[42] C. J. Brabec, S. E. Shaheen, C. Winder, N. S. Sariciftci and P. Denk, *Appl. Phys.Lett.*, 2002, **80**, 1288

[43] V. D. Mihailetchi, L. J. A. Koster, P. W. M. Blom, C. Melzer, B. de Boer, J. K. J.van Duren and R. A. J. Janssen, *Adv. Funct. Mater.*, 2005, **15**, 795

[44] W. L. Ma, C. Y. Yang, X. Gong, K. Lee and A. J. Heeger, *Adv. Funct. Mater.*,2005, **15**, 1617

[45] M. D. Irwin, B. Buchholz, A. W. Hains, R. P. H. Chang and T. J. Marks, *Proc. Natl. Acad. Sci. U. S. A.*, 2008, **105**, 2783

[46] R. Kroon, M. Lenes, J. C. Hummelen, P. W. M. Blom and B. De Boer, *Polym.Rev.*, 2008, **48**, 531

[47] L. M. Campos, A. Tontcheva, S. Gunes, G. Sonmez, H. Neugebauer, N. S. Sariciftci and F. Wudl, *Chem. Mater.*, 2005, **17**, 4031

[48] M. Lenes, M. Morana, C. J. Brabec and P. W. M. Blom, *Adv. Funct. Mater.*, 2009, **19**, 1106

[49] F. L. Zhang, E. Perzon, X. J. Wang, W. Mammo, M. R. Andersson and O. Inganäs, *Adv. Funct. Mater.*, 2005, **15**, 745

[50] J. Peet, J. Y. Kim, N. E. Coates, W. L. Ma, D. Moses, A. J. Heeger and G. C. Bazan, *Nat. Mater.*, 2007, **6**, 497

[51] S. H. Park, A. Roy, S. Beaupre, S. Cho, N. Coates, J. S. Moon, D. Moses, M. Leclerc, K. Lee and A. J. Heeger, *Nat. Photonics*, 2009, **3**, 297

[52] Y. Liang, Z. Xu, J. Xia, S.-T. Tsai, Y. Wu, G. Li, C. Ray and L. Yu, *Adv. Mater.*, 2010, **22**, E135

[53] T. G. Schmalz, W. A. Seitz, D. J. Klein and G. E. Hite, *Chem. Phys. Lett.,* 1986,**130**, 203

[54] M. T. Rispens, A. Meetsma, R. Rittberger, C. J. Brabec, N. S. Sariciftci and J. C.Hummelen, *Chem. Commun.,* 2003, 2116

[55] S. Yoo, W. J. Potscavage, B. Domercq, J. Kim, J. Holt and B. Kippelen, *Appl.Phys. Lett.,* 2006, ***89***, 233516

[56] Y. Yao, C. J. Shi, G. Li, V. Shrotriya, Q. B. Pei and Y. Yang, *Appl. Phys. Lett.,*2006, **89**,15350

[57] M. M. Wienk, J. M. Kroon, W. J. H. Verhees, J. Knol, J. C. Hummelen, P. A. vanHal and R. A. J. Janssen, *Angew. Chem. Int. Ed*., 2003, **42**, 3371

[58] Y. He, H. Chen, J. Hou and Y. Li, *J. Am. Chem. Soc*., 2010, **132**, 1377

[59] V. H. H. Hertz, "Ueber die Berührung fester elastischer Körper," *Journal für die reine und angewandte Mathematik (Crelle's Journal)*, no. 92, pp. 156-171, 1882.

[60] K. L. Johnson, K. Kendall, and A. D. Roberts, "Surface energy and the contact of elastic solids," *Proceedings of the Royal Society A: Mathematical, Physical and Engineering Sciences*, vol. 324, no. 1558, pp. 301-313, Sep. 1971.

[61] B. Derjaguin, "Effect of contact deformations on the adhesion of particles," *Journal of Colloid and Interface Science*, vol. 53, no. 2, pp. 314-326, Nov. 1975.

[62] D. Maugis, "Adhesion of spheres: The JKR-DMT transition using a dugdale model," *Journal of Colloid and Interface Science*, vol. 150, no. 1, pp. 243-269, Apr. 1992.

[63] R. Carpick, D. Ogletree, and M. Salmeron, "A general equation for fitting contact area and friction vs load measurements," *Journal of Colloid and Interface Science*, vol. 211, no. 2, pp. 395-400, Mar. 1999.

[64] M. A. Lantz, S. J. O'Shea, M. E. Welland, and K. L. Johnson, "Atomic-force-microscope study of contact area and friction on $NbSe_2$," *Physical Review B*, vol. 55, 16, 10776-10785, 1997.

[65] Foster, M. D. X-ray scattering methods for the study of polymer interfaces. *Critical Reviews in Analytical Chemistry* **1993**, *24* (*3*), 179-241.

[66] Bras, W.; Ryan, A. J. Sample environments and techniques combined with small angle X-ray scattering. *Advances in Colloid and Interface Science* **1998**, *75*, 1-43.

[67] Yang, L. Using an in-vacuum CCD detector for simultaneous small- and wide- angle scattering at beamline X9. *J. Synchrotron Rad*. **2013**, *20,* 211-218.

[68] Allaire, M.; Yang, L. Biomolecular solution X-ray scattering at the National Synchrotron Light Source. *J. Synchrotron Rad*. **2011**, *18*, 41-44.

[69] Phinjaroenphan, R. *et al*. SAXS/WAXS capability and absolute intensity measurement study at the SAXS beamline of the Siam Photon Laboratory. *J Phys: Conference Series* **2013**, *425*, 1-4.

[70] Bras, W. *et al.* Simultaneous time-resolved SAXS and WAXS experiments using synchrotron radiation. *Nuclear Instruments and Methods in Physics Research* **1993**, *A326*, 587 -591.

[71] Kline, R. J.; McGehee, M. D.; Toney, M. F. Highly oriented crystals at the buried interface in polythiophene thin-film transistors. *Nature Mater*. **2006**, *5*, 222-228.

[72] Sirringhaus, H. *et al*. Two-dimensional charge transport in self-organized, high-mobility conjugated polymers. *Nature* **1999**, *401*, 685-688.

[73] Kline, R. J. *et al*. Dependence of regioregular poly(3-hexylthiophene) film morphology and field-effect mobility on molecular weight. *Macromolecules* **2005**, *38*, 3312-3319.

[74] Hlaing, H. *et al*. Nanoimprint-induced molecular orientation in semiconducting polymer nanostructures. *ACS Nano*, **2011**, *5* (*9*), 7532-7538.

[75] Zhang, R. *et al*. Nanostructure dependence of field-effect mobility in regioregular poly(3-hexylthiophene) thin film field effect transistors. *J. Amer. Chem. Soc.* **2006**, *128*, 3480-3481.

Chapter 3

Effects of Pressure on Interfacial Surface Contacts and Current Voltage Characteristics of Organic Solar Cells

3.1 Introduction

Enhanced interfacial contacts in bi-layered and multi-layered structures in bulk heterojunction Organic Photovoltaic (OPVs) device fabrications have attracted widespread interests for large-area solar energy conversion[1]. This is due to their attractive combinations of efficiency (~5-7%) and potential for low temperature fabrication with relatively cheap organic materials. An OPV structure consists of an inorganic Indium-Tin Oxide (ITO/Glass) as anode, Poly (3,4-ethylenedioxythiophene:poly (styrenesulphonate) (PEDOT.PSS) as hole transport layer (HTL) and Poly(3-hexylthiophene):Phenyl-C61 butyric acid methyl ester (P3HT:PCBM) bulk heterojunctions as the photoactive layer. The electron transport layer (ETL), Lithium Fluoride (LiF) and a back contact cathode of Aluminum complete the device. These HTL and ETL layers

facilitate the separation of excitons into electrons and holes and conduct them to the respective electrodes. This gives high organic photovoltaic device performance.[2-4]

Prior work on the different HTL materials for organic photovoltaics (OPVs) and Organic Light Emitting Devices (OLEDs) have been carried out by Du *et al*.,[5] Tong *et al*.,[6] and Agyei-Tuffour *et al*.[7] These studies have identified the performance of different HTL materials on the current-voltage behavior of OLEDs and OPVs. The inorganic HTLs: (Vanadium pentoxide (V_2O_5), Nickel oxide (NiO), Tungsten trioxide (W_2O_3) and Molybdenum trioxide (MoO_3)) although recorded improved and stable power conversion efficiencies in OLEDs,[8-10] subjecting these layers to pressure effects often result in layer and particle sink-in largely due to their mechanical properties (Young's moduli, Poisson ratio and stiffness).[6] On the contrary, the organic based HTLs such as Poly (3,4-ethylenedioxythiophene:poly (styrenesulphonate) (PEDOT.PSS) due to its high and tunable work function,[11,15] has predominantly been used as hole injection layer (HIL) in OLEDs[12] and as hole collecting layer (HCL) in OPVs.[13,14]

However, although the solution processing of PEDOT.PSS is potentially, a scalable route and economical in large area OPV manufacturing,[16] it may during deposition, result in uneven coverages leading to blisters formation. The blisters form as result of the presence of dust particles in the clean room that are trapped onto the substrate prior to film deposition. The trapped particle therefore reduces the interfacial contacts and may result in the inconsistent performance of fabricated devices. In order to improve the interfacial contacts, compliant HTL materials can be used and with the application of moderate pressures on the deposited films, even greater contacts and planarized films can be achieved. It is also possible to transfer layers using lamination processes with the ultimate aim of closing voids, improving interfacial contacts, and enhancing the transport of charges across the interfaces in the layered OPV device.

Therefore, in this paper, we present the results of lamination/stamping pressure on the interfacial contacts in bulk heterojunction OPVs with PEDOT.PSS as the HTL material. The effects of the applied pressures are studied in bi-layer systems and devices usually adopted in OPV fabrications with the aid of a poly di-methyl siloxane (PDMS) stamps. The effects of the film's Young's moduli, adhesion energy and pressure on interfacial contacts and void lengths are also modeled using analytical and finite element approaches. The implications of the results are discussed to influence the design of stamping, lamination and other pressure assisted fabrication processes.

3.2. THEORY

3.2.1 Modeling of Surface Contacts

Organic thin films subjected to loading (pressure) may exhibit elastic and or plastic deformation depending on the nature of the film. For example, the mechanical properties of the films and the trapped particles may influence the deformation. For instance, the Young's moduli of the films and the trapped particles may lead to the classification of the materials into rigid, semi rigid and compliant materials. These classifications can therefore greatly compromise the deformation of the films to achieve improved interfacial contacts. In the case of a compliant organic thin films and trapped particles; silicone, PDMS, photoresist and textile polymer, etc., for example, deformation in the layers and or in the layers around trapped particles usually mimic's the cantilever beam displacement behavior. The beam deflection may lead to improved contacts between the layers and around the trapped particle. When the films and trapped particles are rigid (ITO, MoO_3, Silicon, Aluminum, Iron, quartz), interfacial contact improvements can be difficult to achieve and occasionally, layer or trapped particle sink-in occurs compared to semi rigid

materials; Poly-[2-methoxy-5-(2-ethylhexyloxy)-1,4-phenylenevinylene] (MEH-PPV, P3HT:PCBM). The trapped particle sizes usually range from ~ 0.1 to ~ 20 μm in diameter.[17,18] These are often trapped at the interfaces between the layers and can therefore, influence the contact areas in the OPV layers. Prior work has also shown that, increasing pressure results in increased surface contact while the void lengths (S) decrease with increase in pressure. These resulted in improved contacts at the interfaces between adjacent layers in organic photovoltaic cells (OPVs),[16] and in organic light emitting devices (OLEDs).[5, 15]

Prior work on analytical models [18-22] have reported the study of contact profiles in cases where the trapped particles are interlocked before the application of pressure. Considering a PEDOT.PSS film that forms a blister with radius, "*r",* and upon sandwiching a trapped particle as in Figure 1, Du *et al*.,[5] Malyshev-Salganik *et al.*[21] and Wan-Mai *et al.*[22] idealized the contact as that associated with a penny crack in bending by considering the relationship between the surface energies, stored energies and other variables to determine the adhesion energy (γ) between the layers.

$$\gamma = \frac{2Ew^3h^2}{3\left(1-\nu^2\right)r^4}, \qquad (1)$$

where *E* is the Young's modulus and ν is the Poisson's ratio of the PEDOT.PSS film; *w, h,* are respectively, the thickness and height of the trapped particle or blister formed. When the thickness of the film compared with the height of the trapped particle or radius of the blister is much smaller, then, the film will undergo stretching and bending and these will account for the total energy stored in the film (U_T) when the membrane's moment of area (II) denoted by *I,* is according to the equation:

$$U_T = \frac{6EIh^2}{s^3} - \gamma w(L-s), \tag{2}$$

Prior work by Agyei-Tuffour *et al.*[7] have also shown that the void (s) and contacts length ratios (L_c/L) are related in the following expressions:

$$s = \left(\frac{3Ew^3h^2}{2\gamma}\right)^{\frac{1}{4}} \tag{3}$$

and

$$\frac{L_c}{L} = 1 - \frac{1}{L}\left(\frac{3}{2}\frac{Ew^3h^2}{\gamma}\right)^{1/4} \tag{4}$$

Similarly, the contact length can also be written as a function of the applied pressure according to Du *et al.*[5] and Asare *et al.* [28]as:

$$\frac{L_c}{L} = 1 - \left[\frac{3\left(\frac{E}{\left(1-v^2\right)}\right)w^3h}{2PL^4}\right]^{\frac{1}{4}} \tag{5}$$

Since the properties of the thin layer materials are known, the contact length ratio and the void lengths can be accurately predicted. The adhesion energies can also be estimated for the different interfaces in the organic electronic structures.[5,6,7] Du *et al.*[5] and Tong *et al.*[6] conducted experimental studies to verify the predicted adhesion energies from the above analytical models for some common organic thin films that are relevant to OPVs and OLEDs fabrication. Similar study on cold-welded metallic thin films has also been reported.[24] Numerical simulation results

based on the analytical model has also been validated with experimental results by Cao *et al.*[15], Akande *et al.*[24] and Asare *et al.*[28]

3.3 Adhesion and Contacts Modeling: Finite Element Analysis

Finite element modeling with ABAQUS CAE 6.12 software package (ABAQUS™, Simulia, Pawtucket, RI, USA) was used to model interfacial contacts and void lengths profiles around the interlocked particles (blisters). The simulations considered the contacts profiles associated with a blister of height, ~1 μm which is commonly the diameters of migrating airborne dust particles in the clean room according to prior work by Du *et al.*[5] and Moreau *et al.*[14,17]

The influence of the surface morphology (surface roughness) was considered in modeling the pressure effects with four nodal element mesh. Fine meshing was used at locations of contacts that may have extensive displacements and stress distributions. The possibility of displacement and rotation about the bottom part of the substrate was eliminated by fixing the substrate. Lateral movements were equally eliminated because the outer edge of the model was also fixed as reported by prior work.[5, 7, 28] By assuming that, all the thin film materials are isotropic, a uniform pressure was applied on the stamp and the deformation was simulated for the blisters, trapped particles and the thin film layers (P3HT:PCBM), the HTL (PEDOT:PSS) and the Transparent conducting oxide (TCO) layer, ITO.

3.4 EXPERIMENTAL PROCEDURES

3.4.1 Photovoltaic Device Fabrication and Characterization

In order to verify the predicted results by the analytical and finite element simulations, an experimental work was conducted on OPV devices with the aid of pressure and PDMS stamp. The model photovoltaic devices were fabricated using the

Glass/ITO/PEDOT:PSS/P3HT:PC60BM)/LiF/Al architecture. The devices' response to applied pressures was studied by monitoring the changes in the current-voltage behavior of the OPV device. AFM analysis of the surface morphology and roughness were measured with a 1:1 aspect ratio and a 3 μm x 3 μm scan size. This was done with the atomic force microscope (AFM, Nanoscope IV, Bruker, Plainview, NY, USA).

In the fabrication, firstly, the patterned indium tin oxide (ITO) was ultrasonically cleaned with acetone, ethanol and deionized water in succession. The substrates were further cleaned in an Ultra-Violet Ozone system for 10 minutes before an ~40 nm thick PEDOT:PSS was deposited at 3500 rpm for 1 minute. The resultant composite was heat treated at 120^{o}C for 10 minutes in air and followed by the active layer deposition. 20 mg/ml concentration of P3HT:PCBM in chlorobenzene was deposited at 700 rpm spin speed for 180 s. The three-layered composite OPV system was transferred into an argon filled glove box and annealed at 140^{o}C for 4 minutes. Afterwards, an ~ 0.2 nm protective layer of LiF and a 150 nm Al back contact layers were thermally deposited to produce devices of ~ 0.105 cm^{2}

The photovoltaic characteristics of the resulting devices were characterized for the as-fabricated and also after pressure application using PDMS stamps (ϕ = 30 mm, δ = 5 mm) and static loads. Prior work by Du *et al.*[5] and Agyei-Tuffour *et al.*[7,29] show that, pressure applications greater than 10 MPa often results in particle sink-in, layer damage and reduced photoconversion efficiency and therefore, an ~ 10 MPa pressure was adopted in this work to access the pressure effects. In all, four (4) devices were fabricated and tested for this study and the averages of the results are reported. All measurements were carried out in ambient conditions as reported in our prior work.[5,7,29]

3.5 Results and Discussion

3.5.1 Surface characterization of compliant OPV layers

Figure 3.1(a)-(b) presents the surface morphologies (2D and 3D) of the OPV layer materials acquired from the AFM measurements. The average surface roughness (R_a) values are also presented in Table 3.1. These show that the PEDOT.PSS layer (Figure 3(a) had $R_a \sim 0.8\pm0.1$ nm while the P3HT:PCBM layer (Figure 3.2(b) had $R_a \sim 0.7\pm0.1$ nm. The AFM results show that, the surface morphology makes it suitable in selecting different pairs of materials for OPV fabrication. For instance in the soft contact lamination processes, the pressure applied on the bilayer device joins the films together physically and this process improves the adhesion between the layers. From Table 3.1, the adhesion energies between the glass substrate, PEDOT:PSS and P3HT:PCBM are 9.3, 2.9 and 0.5 J/m^2 respectively (Tong *et al.*[6]), and thus contribute greatly to the strong interfacial bonding upon pressure application. The surface contacts obtained would also depend on the degree roughness and the applied pressures.

Should the surface be rough prior to applied pressure, then, trapped particle sink-in, thin film layer sink-in and multiple partial contacts phenomena can occur and these often results in low device efficiency due to short circuiting from the multiple surface contacts. These phenomena also lead to the degradation of charge transfers across the interfaces. Contrarily, smooth surface contacts require less pressure to attain remarkable interfacial contacts. Charge transport across the interface generally improves. However, higher pressures on smooth surface contacts may equally result in layer or trapped particle sink-in as stated above. [6,31]

Figure 3.3 presents the transmittance of the PEDOT.PSS (Figure 3.3(a)) and the absorbance of the P3HT:PCBM (Figure 3.3(b)) upon annealing and pressure assisted treatment. The transmittance of the PEDOT:PSS layer on glass show better results for a wide range of

wavelength as a function of applied pressure. The region of absorption of the P3HT:PCBM also covers the UV and Visible ranges of the electromagnetic spectrum and indicates that, there exist an active interaction between the P3HT and PCBM components upon blending. This reduces the absorbance of the P3HT/PCBM blend in the pressure-less condition (Figures 3(a) and 3(b)). However, upon the application of pressure and annealing, the absorbance in the P3HT/PCBM polymer blend increased due to the reduction in the surface roughness and the improved polymer crystallinity.

The current results therefore suggest that, AFM analyses of OPV layers can be used for the ranking of adhesion between different surface pairs relevant to device's electronic structure. This is also important in the selection of materials for possible device applications like lamination and cold-welding in which device parts are separately fabricated and components assembled with pressure. The strongly adhering interfaces are thus good candidates for contact layers. Hence, the effects of the pressure on these surface evolutions, roughnesses and morphologies on light's absorption and transmission at the interfaces between the OPV device layers is very significant.

3.5.2. Adhesion and Contacts Modeling: Analytical Modeling

The analytical models showing the contact and void lengths are presented in Figures 3.4 (a) and 3.4 (b). From the predictions, contact length increase and void length reduction were associated with increase in the applied pressure. It is notable that, an ~99.95% contact lengths was achieved. Hence, increasing the pressure further beyond 10 MPa resulted in no significant reduction in the void lengths. The contact length ratio (Figure 3.5(a)) and the void length ratios (Figure 3.5(b)) also shown to depend strongly on the characteristics of the upper layer thin films and the trapped particles. The young's moduli, the poisson ratio and the adhesion energies of the

upper layers and trapped particles are the major materials characteristics according to prior work by Agyei-Tuffour *et al.*,[7] Cao *et al.*[18] and Akande *et al.*[24] The contact length ratio increase with increasing Young's moduli (Figure 3.5(a) and reduction in void length with increasing Young's moduli. The void length ratios, s, also decreased with increasing adhesion energy, (γ), (Figure 3.6(a)) while the contact length ratios, L_c/L, increased with increasing adhesion energy (Figure 3.6(b)). These results agree with prior work in which applied pressures and annealing of compliant OPV layers were reported to reduce nanovoid sizes, increase interfacial contacts and resulted in enhanced current-voltage response in organic light emitting devices (OLEDs) and in bulk heterojunction photovoltaic cells (OPVs).[6,7] The impact of the pressure on the adhesion energy could also be very significant in the engineering of robust interfaces. It is very useful in predicting Mode I fracture mechanism as well as in predicting the stresses that may exist in rigid structures.

The analytical model therefore suggest that, to achieve improved contacts whilst preventing layer or trapped particle sink-in, compliant and semi-rigid trapped particle will require moderate and or intermediate pressures. However, excessive pressure can result ultimately in the damage of organic electronic devices and therefore, the best balance of improved contacts and applied pressures should be the major goal.

In addition, high Young's moduli of the upper layers often leads to void length increases due to the high stiffness and reduced displacement potential upon the application of pressure. This suggests that, stamps adopted in pressure assisted fabrication of OPVs should be made of lower modulus materials. Hence, soft lamination processes can be assured with stamps made of poly-di-methyl-siloxane (PDMS) due to it soft and flexible nature. Soft stamps should be used during the pressure-assisted fabrication of organic photovoltaic cells.

3.5.3. Pressure and Surface Roughness Effects: Finite Element Modeling

Figures 3.7 shows the evolution of contact profiles around trapped particles, the meshing of thin film layer materials, geometry of the evolved contacts and the formation of blisters during pressure application on the PDMS stamps. The results show that the surface contacts depend on the surface roughness and the applied stresses. In the case of rigid particle and rough contact surfaces, multiple surface contacts can occur, giving rise to partial contacts, even in regions remote from the dust particles. Such partial contacts may degrade the charge transport between adjacent layers. In contrast, the surface contacts between smooth layers and compliant or semi rigid trapped particles result in simpler contact profiles (Figures 3.8(a-b)). The initially high stresses also reduce with increase deformation. Hence, smooth surface morphologies required lower pressures to achieve enhanced contacts, while rougher surface morphologies result in multiple partial contacts due to the surface topographies. Furthermore, increased sink-in of the dust particles was observed to occur with increased pressure (greater than ~10 MPa) Figure 3.8(c), which may lead ultimately to the damage of organic photovoltaic cells during pressure assisted fabrication.[23,25,26]

3.5.4 Current-voltage characteristics of photovoltaic cells

Plots of current density against voltage (I-V) are presented in Figure 3.9 for photovoltaic cells with PEDOT.PSS hole transport layers. The effects of pressure application (~ 10 MPa) are also presented in the same figure. The results show that pressure application leads to immense improvement in current-voltage behavior (Figure 3.9) of the organic photovoltaic cells.

In the case of the OPV devices, ~18% increase in the short circuit current (I_{sc}) with a corresponding 7.20% increase in the fill factor was recorded. The efficiency of the device also increased from ~3.5% to ~ 4.4%. This represents an increase of ~25% increase in the efficiency

of the OPV device. The variations in the device performances are shown in the errors presented in Figure 3. 9. The uneven film deposition by spin coating and the non-uniform application of pressure /dead weights could be the reasons for the observed dispersion. These could be minimized by the adoption of a mechanical tester that has the potential to carefully control the pressure applications. It is important to note however that the devices with PEDOT.PSS HTLs experienced significantly increased contact that led to the observed increase in photo-conversion efficiency. Hence, the nature of the OPV layers (PEDOT:PSS, P3HT:PCBM) which are largely compliant leads to an improved interfacial contacts that can enhance the transport of charges across the interfaces.

3.5. Implications

The study shows that, the power conversion efficiencies and performance of OPVs are improved by the application of pressure. The effects of pressure caused the closing up of voids and the corresponding increase in the contact lengths. In any case, the contact lengths increase under pressure, while the void lengths decrease under pressure, resulting in increased contact area across the interfaces in the OPV structures. Hence, the higher power conversion efficiency of ~25% increase is attributed largely to the increased contact area due to the application of pressure. The improvement could also be due to a reduction in the sheet resistance of the polymers as a result of the annealing and pressure application.

The current work, therefore, suggests that the current-voltage characteristics of OPV can be enhanced by the application of controlled levels of pressure in lamination and stamping processes. Such pressure may be applied after using conventional spin-coating and thermal evaporation techniques to deposit the individual layers in the OPV structures. However, great care is needed to ensure that the applied pressure does not result in excessive sink-in, which can

lead to damage of the device. The required balance of improved contact without excessive sink-in should also be guided by computational models and additional experiments. There is also a need to explore a range of deposition methods for the fabrication of organic layers in polymer based devices. These include: spray coating; self-assembled monolayers and other evaporation techniques that must be optimized prior to pressure application.[5,7] Post-deposition processes, such as annealing and pressure application, should also be carried out in controlled environments (glove boxes and/or clean rooms).

Hence, the improvement in the device efficiency observed after pressure application can be attributed to the combined effects of improved surface contacts, as well as the pressure, which led to elongated polymer chains, and ultimately to enhanced crystallinity in the active layer.[29] Such developments could facilitate the development of fast, low-cost stamping and roll-to-roll processes,[27] in OPV devices fabrication. The current work suggests that these are possible, provided sufficient pressures are applied, without inducing significant damage (sink-in) in the layered structures of the devices.

3.6 Summary and Concluding Remarks

This paper presents the results of a combined analytical, computational and experimental study of interfacial surface contacts and current-voltage behavior, induced via pressure assistance on the OPV layers and devices. The models, using the adhesion energies, the Young's moduli of the OPV layers, trapped particles and the surface roughness characteristics of the layers were carried out to assess the influence of pressure application. The predictions from the models were also verified with experimental results. The void length reduction and the contact length increase are associated with increases in the applied pressure.

The pressure increases also results in improved power conversion efficiencies for devices with PEDOT.PSS HTL subjected to ~10 MPa pressure. The improvements are attributed to the combined effects of increased surface contacts and increased polymer crystallinity that occur during pressure application and annealing.

The current results suggest that pressure-induced contacts may be used to enhance the current-voltage response and power conversion efficiencies of organic photovoltaic cells. However, excessive pressure must be avoided to reduce the possibility of device damage due to sink-in of trapped particles. The surface roughness of the device layers should also be reduced to improve the adhesion and surface contacts in the OPV layers.

3.7 References

1. 1. S. B. Darling, F. You, T. D. Veselka, A. Velosa:, *Ener. & Envir. Sci.*, **4,** 3133–3139, (2011).
2. S. A. Choulis, A. Patwardhan, M. K. Mathai, V. -E. Choong and F. So, *Adv. Funct. Mater,* **16 (8)**, 1075–1080, (2006).
3. T. M. Brown, J. S. Kim, R. H. Friend, F. Cacialli, R. Daik and W. J. Feast:, *Appl. Phys. Lett.*, **75** (12), 1679–1681, (1999).
4. V. Shrotriya, G. Li, Y. Yao, C-W. Chu and Y. Yang, *Appl. Phys. Lett.*, **88**, 073508, (2006).
5. J. Du, V. C. Anye, E. O. Vodah, T. Tong, M. G. Zebaze Kana and W. O. Soboyejo, *Jr. Appl. Phys.*, **115**, 233703, (2014).
6. T. Tong, B. Babatope, S. Admassie, J. Meng, O. Akwogu, W. Akande and W. O. Soboyejo, *J. Appl. Phys.*, **106**, 083708, (2009).
7. B. Agyei-Tuffour, E.R. Rwenyagila, J. Asare, O.K. Oyewole, M.G. Zebaze Kana, D.M. O'Carroll, W.O. Soboyejo, *Adv. Mater. Res.* Vol. **1132,** 204-216, (2016).
8. K. J. Reynolds, J. A. Barker, N. C. Greenham, R. H. Friend, and G. L.Frey, J. Appl. Phys. 92, 7556 (2002).
9. H. You, Y. Dai, Z. Zhang, and D. Ma, J. Appl. Phys. 101, 026105 (2007).
10. W.-J. Shin, J.-Y. Lee, J. C. Kim, T.-H. Yoon, T.-S. Kim, and O.-K. Song,, Org. Electron. 9, 333–338 (2008).
11. C. J. Brabec, V. Dyakonov, J. Parisi, N.S. Sariciftci (Eds.), *Springer-Verlag*, Heidelberg, (2003).
12. G. Yu, J. Gao, J. C. Hummelen, F. Wudl, A. J. Heeger, *Science*, **270,** 1789, (1995).

13. S. E. Shaheen, C. J. Brabec, N. S. Sariciftci, F. Padinger, T. Fromherz, J. C. Hummelen, *Appl. Phys. Lett.,* **78,** 841, (2001).
14. C.J. Brabec, J.C. Hummelen, N.S. Sariciftci, , *Adv. Mater.,* **11**. (2001).
15. S. Sapp, S. Luebben, Y. B. Losovyj, P. Jeppson, D. L. Schulz, and A. N. Caruso, , *Applied Physics Letters* **88**, 152107, (2006).
16. L. Fengmin, S. Shuyan, G. Xiaoyang, Z. Yun and X. Zhiyuan, *Sol. Energ. Mater. & Sol. Cells*, **94**, 842–845, (2010).
17. W. M. Moreau: Semiconductor Lithography: Principles, Practices and Materials (*Plenum Press*, New York, 1988).
18. Y. Cao, C. Kim, S. R. Forrest, and W. Soboyejo, *Jr. Appl. Phys.*, **98**, 033713, (2005).
19. D. Maugis, M. Barquins and R. Courtel, *Metaux-Corrosion-Industrie*, **605,** 1-10, (1976).
20. International Organization for Standardization, ISO 14644-1:1999, Clean rooms of and Associated Controlled Environments-Part I: Classification of Air Cleanliness (ISO, Switzerland, (1999)).
21. B. M. Malyshev and R. L. Salganik, *Int. J. Fract*., **26**, 261–275, (1984).
22. K. Wan and Y. Mai, *Int. J. Fract*. **74**, 181–197, (1995).
23. T. M. Tong:, PhD Thesis (Princeton University, 2012).
24. W. O. Akande, Y. Cao, N. Yao, and W. Soboyejo. *J. Appl. Phys.,* **107**, 043519, (2010).
25. B. V. Derjaguin and V. M. Muller and Y. P. Toporov:, *J. Col. Inter. Sci.* **53**, 314–325. (1975).
26. J. A. Greenwood, *Proc. R. Soc. Lond.* A **453**, 1277-1297, (1997).
27. S. R. Forrest**,** *Nature*, **428**, 911–918, (2004).

28. J. Asare, S. A. Adeniji, O. K. Oyewole, B. Agyei-Tuffour, J. Du, E. Arthur, A. A. Fashina, M. G. Zebaze Kana and W. O. Soboyejo, AIP Adv., **6**, 065125, and (2016).
29. B. Agyei-Tuffour, E.R. Rwenyagila, J. Asare, M.G. Zebaze Kana, W.O. Soboyejo, *Jr. Mater. Res.*, (2016). DOI: 10.1557/jmr.2016.344
30. W. D. Callister: Materials Science and Engineering: An Introduction (*Wiley, New York*, 2003)
31. Y. Guo, X. J. Ma and Z. H. Su, *Macromolecules*, **46**, 2733–2739 (2013).
32. W. Soboyejo: Mechanical Properties of Engineered Materials (*CRC, New York*, 2003).
33. W. D. Callister: Materials Science and Engineering: An Introduction (*Wiley, New York*, 2003).

Tables

Table 3.1 Mechanical Properties of organic photovoltaic materials used in the finite element simulations.

Material	Young's Modulus [GPa]	Poisson's Ratio	Reference
Glass	69	0.3	33
ITO	116	0.35	13
PEDOT.PSS	1.56	0.3	20
MoO_3	64.6	0.3	13
P3HT:PCBM	6.02	0.3	20
Al	70	0.3	20
PDMS	0.003	0.48	13 and 23
Particle	70	0.3	16

Table 3.2, Short circuit current density (I_{sc}), open-circuit voltage (V_{oc}), fill factor (FF) and power conversion efficiency (PCE) based on PEDOT.PSS devices with and without the influence of pressure.

OPV Device	V_{oc} (V)	I_{sc} (mA/cm^2)	FF (%)	PCE (%)	Pressure effect (%)
PEDOT.PSS (No pressure)	0.72	10.71	54.0	3.79	-
PEDOT.PSS (pressure)	0.74	11.98	56.5	5.02	32.5

Figures

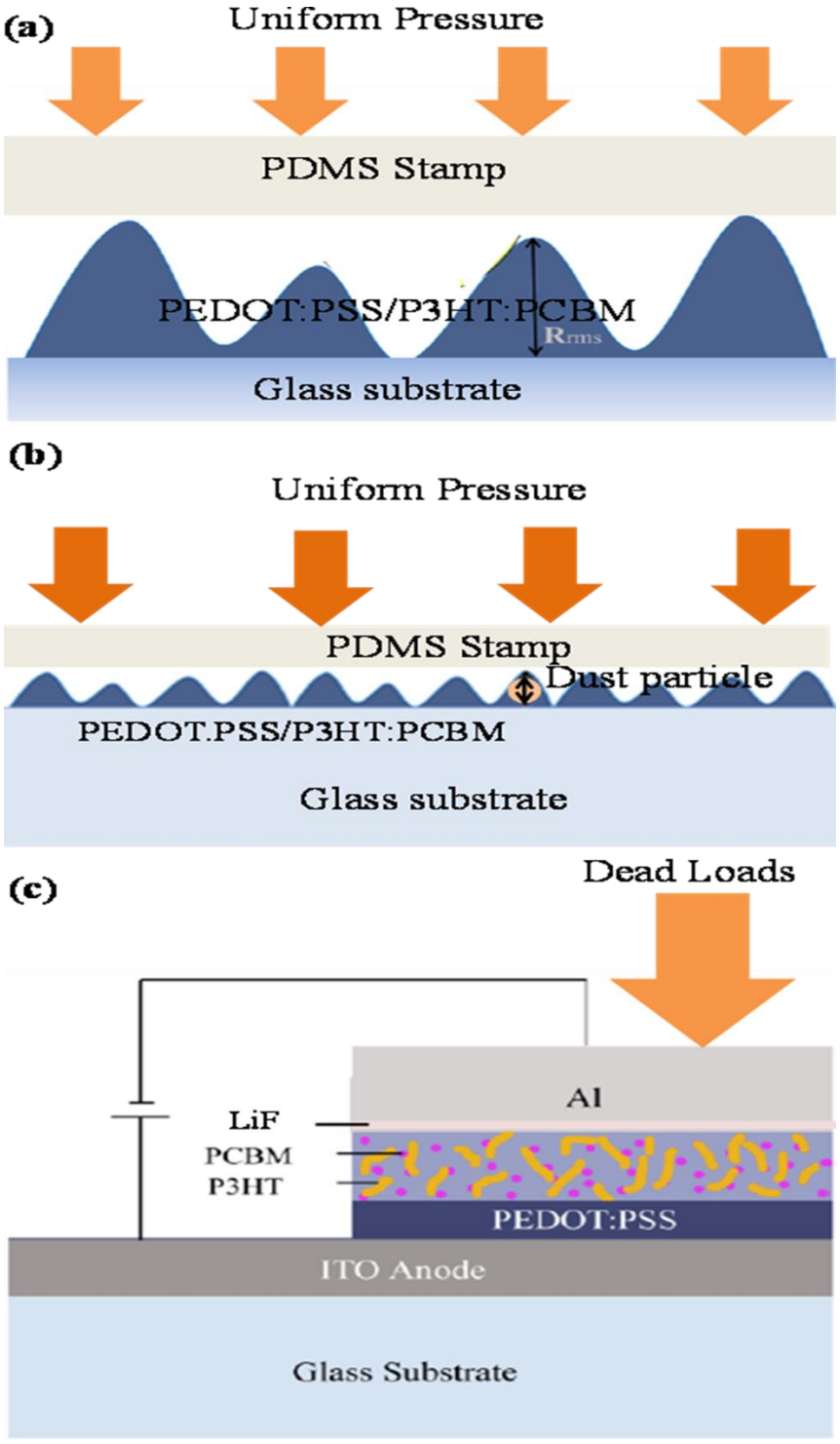

Figure 3.1 Bilayered and multilayered nanostructures adopted in the pressure assisted organic photovoltaic cell fabrication: (a) rough surface contacts with blister height, (b) smooth surface

contact with trapped particle and (c) complete device showing multilayers with pressure application.

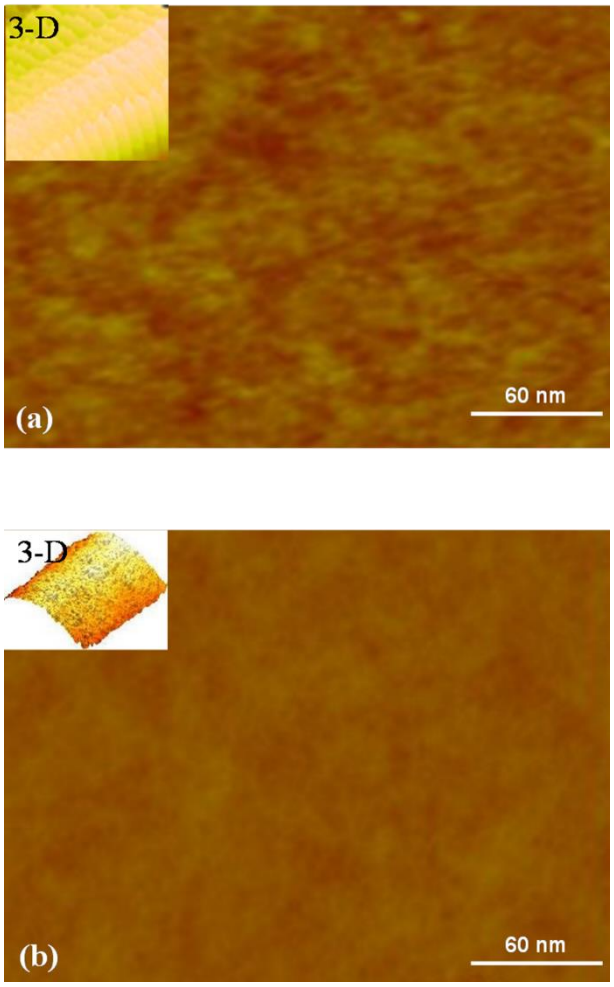

Figure 3.2 The surface morphology of the OPV layered structures acquired from the atomic force microscope in the tapping mode: (a) compliant PEDOT.PSS film as hole transport layer material and (b) bulk heterojunction P3HT:PCBM film as the active layer. Both films are susceptible to blister formation and readily deform around trapped particles (cantilever behavior) upon pressure application. All images were taken over a 3 μm x 3 μm area.

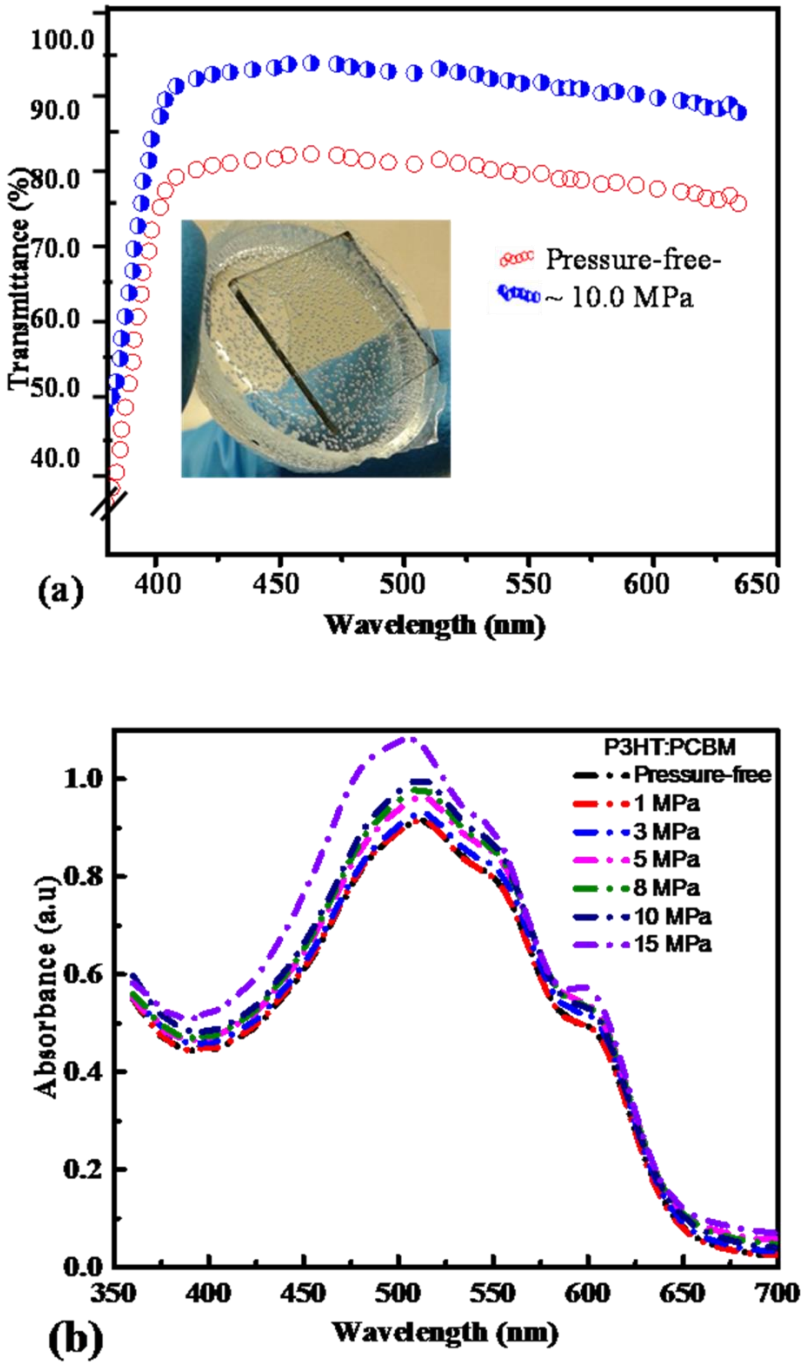

Figure 3.3 shows the optical properties of the OPV thin layer films: (a) transmittance of PEDOT:PSS and (b) absorbance of P3HT:PCBM upon pressure application. (Ref 29) (Ref 7)

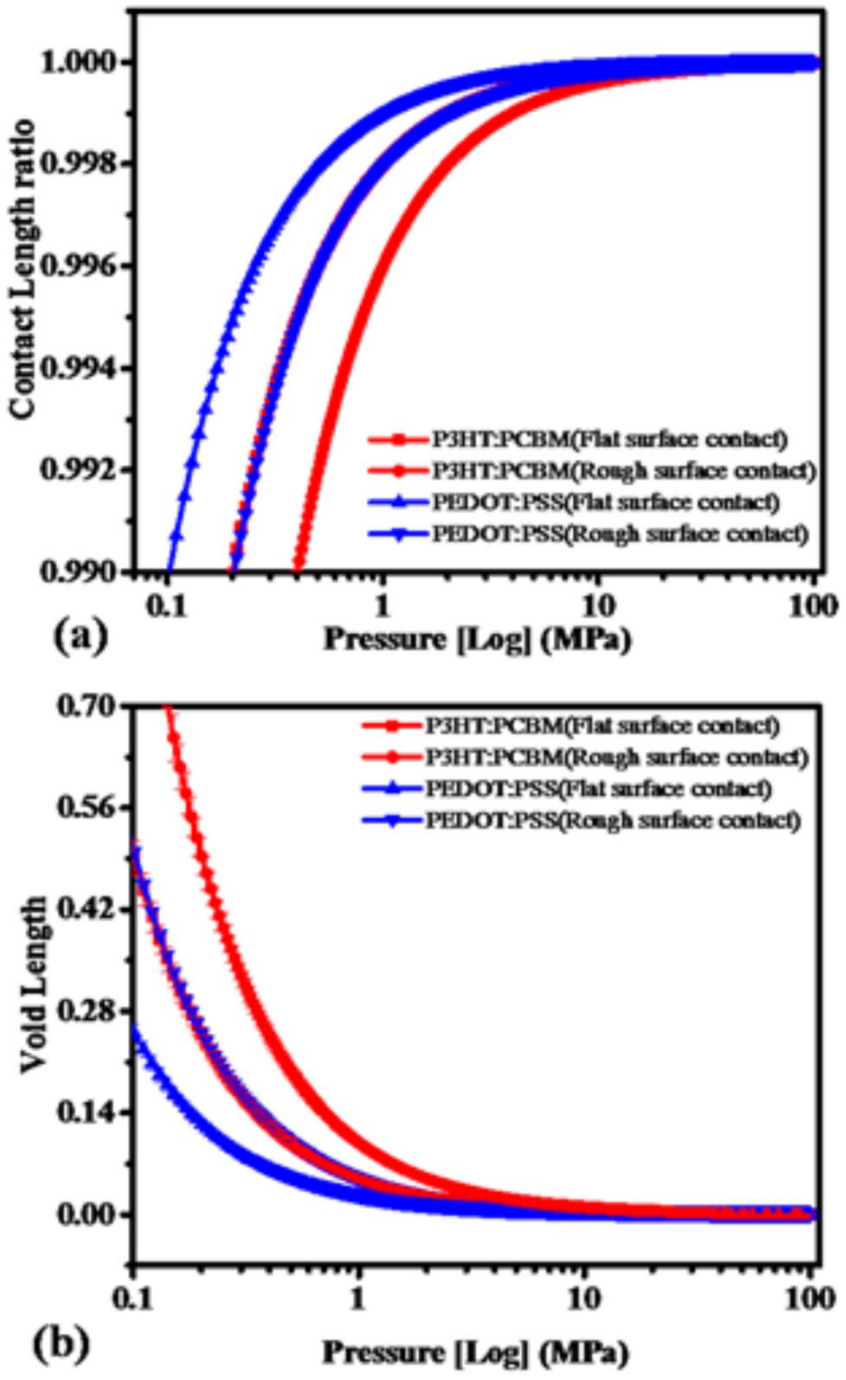

Figure 3.4 Surface contact effects and pressure application on the compliant P3HT:PCBM and PEDOT:PSS upper layers adopted in the OPV device as active layer and hole transport layer respectively: (a) contact length ratios of predicted by the analytical model; (b) void length ratios.

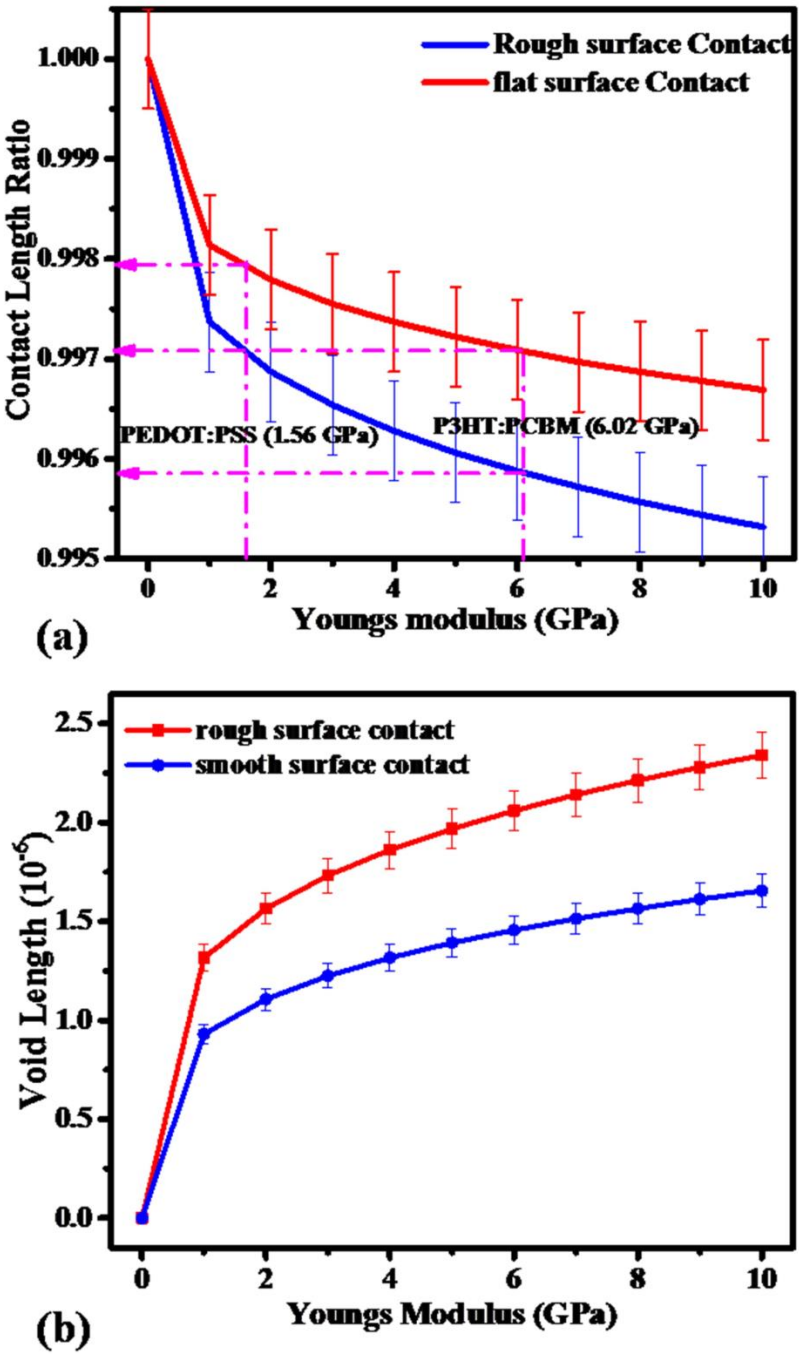

Figure 3.5 Mechanical properties (Young's moduli) of P3HT:PCBM and PEDOT:PSS and surface contacts on: (a) contact length ratios and (b) void length ratios of the upper layer films.

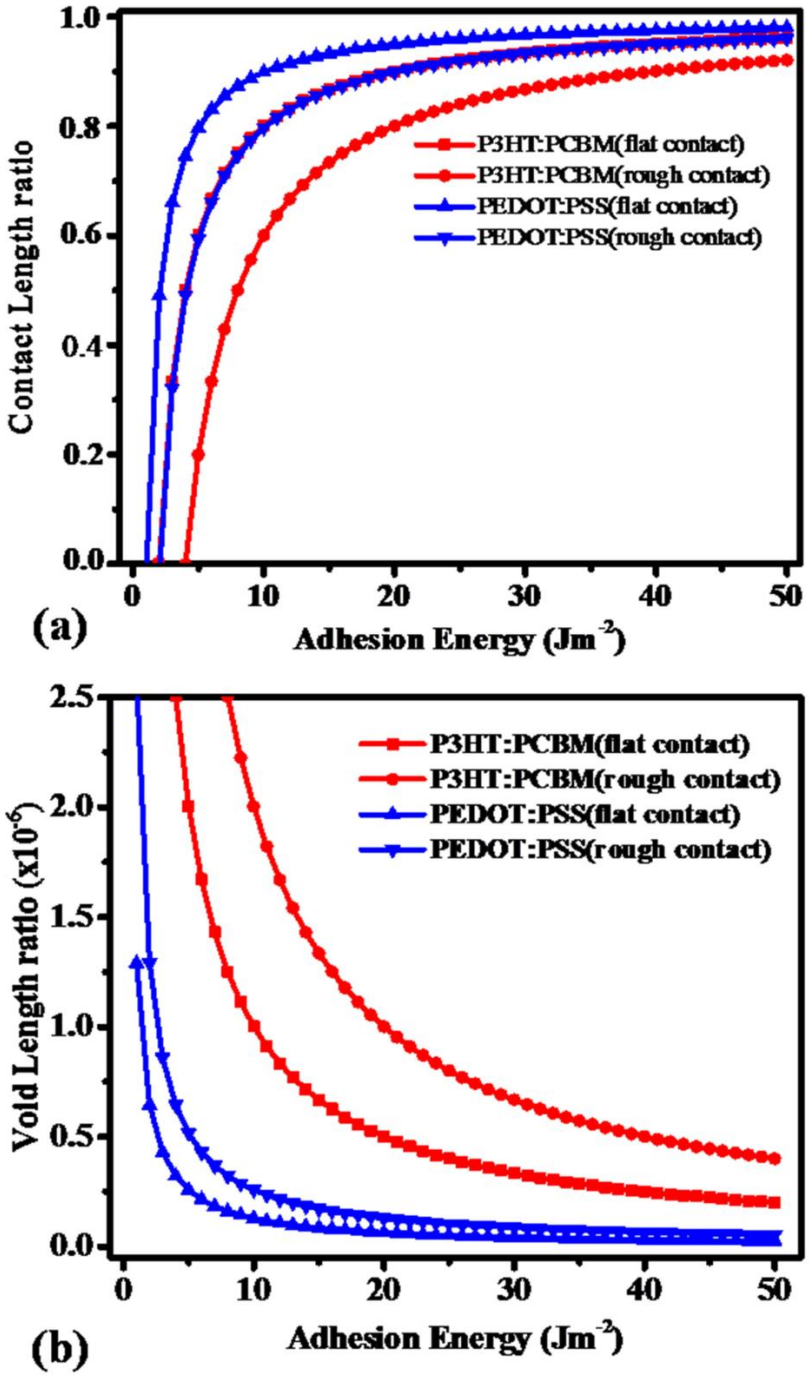

Figure 3.6 shows the influence of adhesion energies on surface contacts profiles: (a) contact length ratios and (b) void length ratios of the upper layer films.

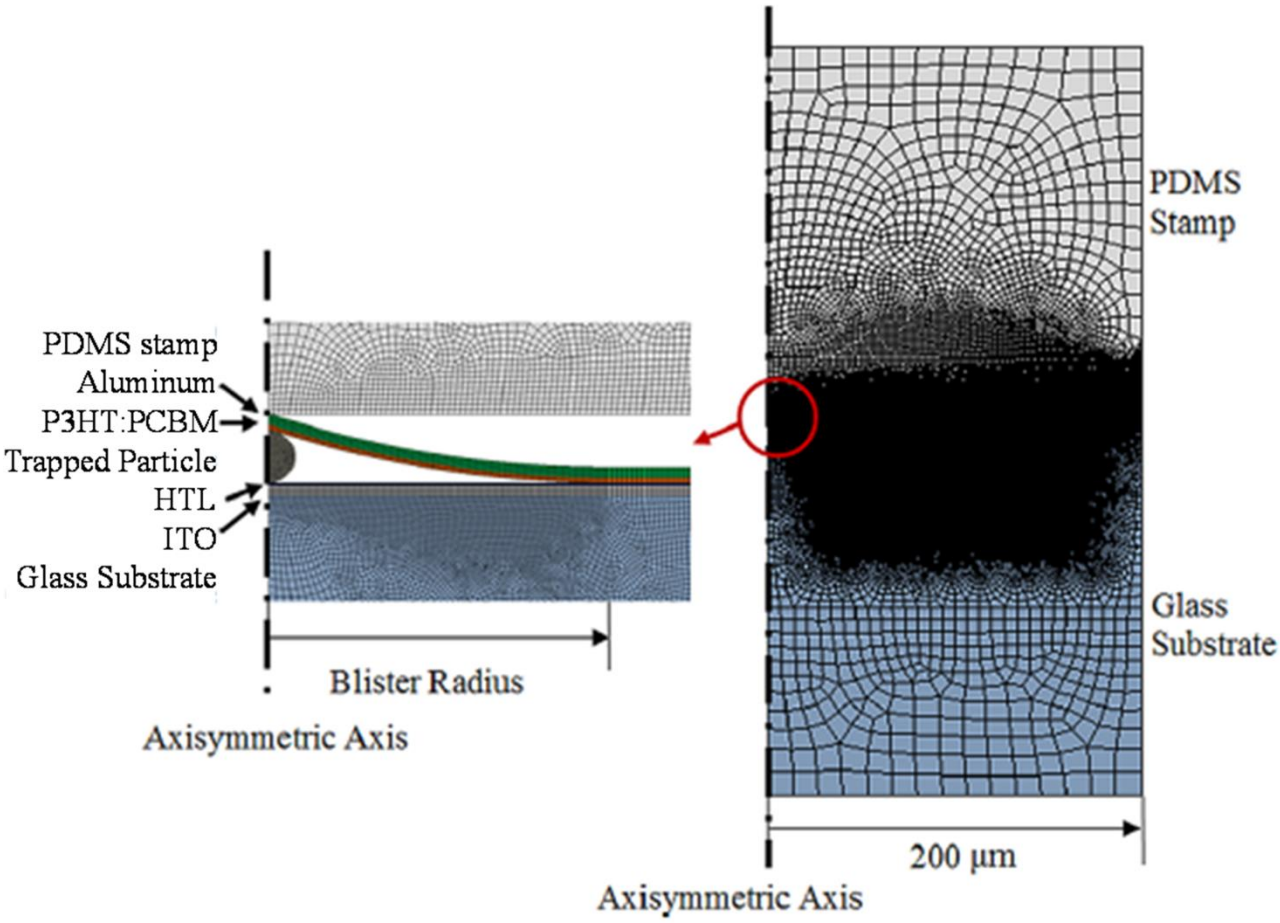

Figure 3.7 Finite element model of surface contact during OPV layer deposition with a trapped particle between the any two layers. The geometry and mesh show the formation of blisters and the evolution of contact during pressure application on the PDMS stamp (Ref. 5).

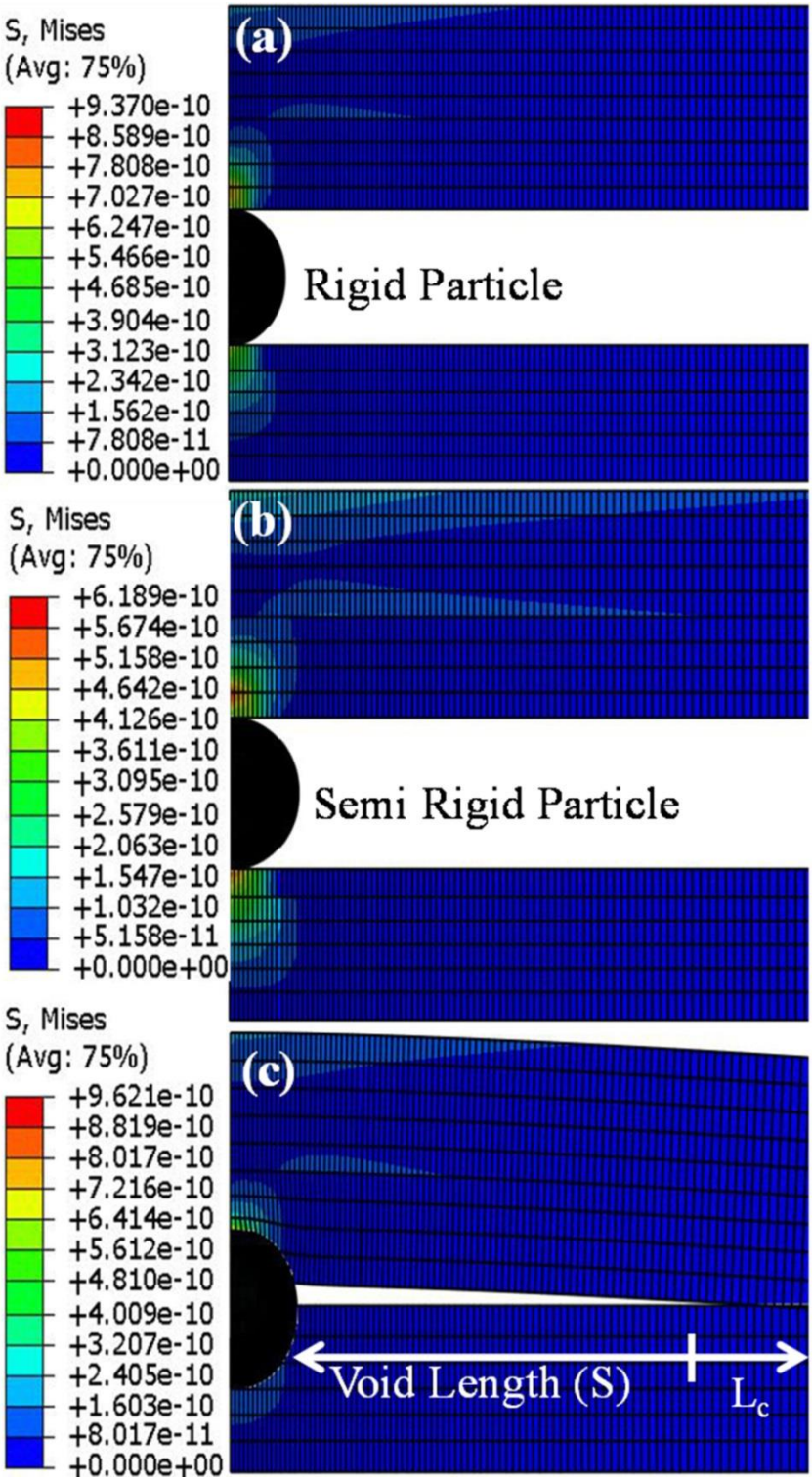

Figure 3.8 Stress distributions induced by rigid, semi rigid and compliant dust particles trapped between Organic Photovoltaic Devices (OPV) layered structures.

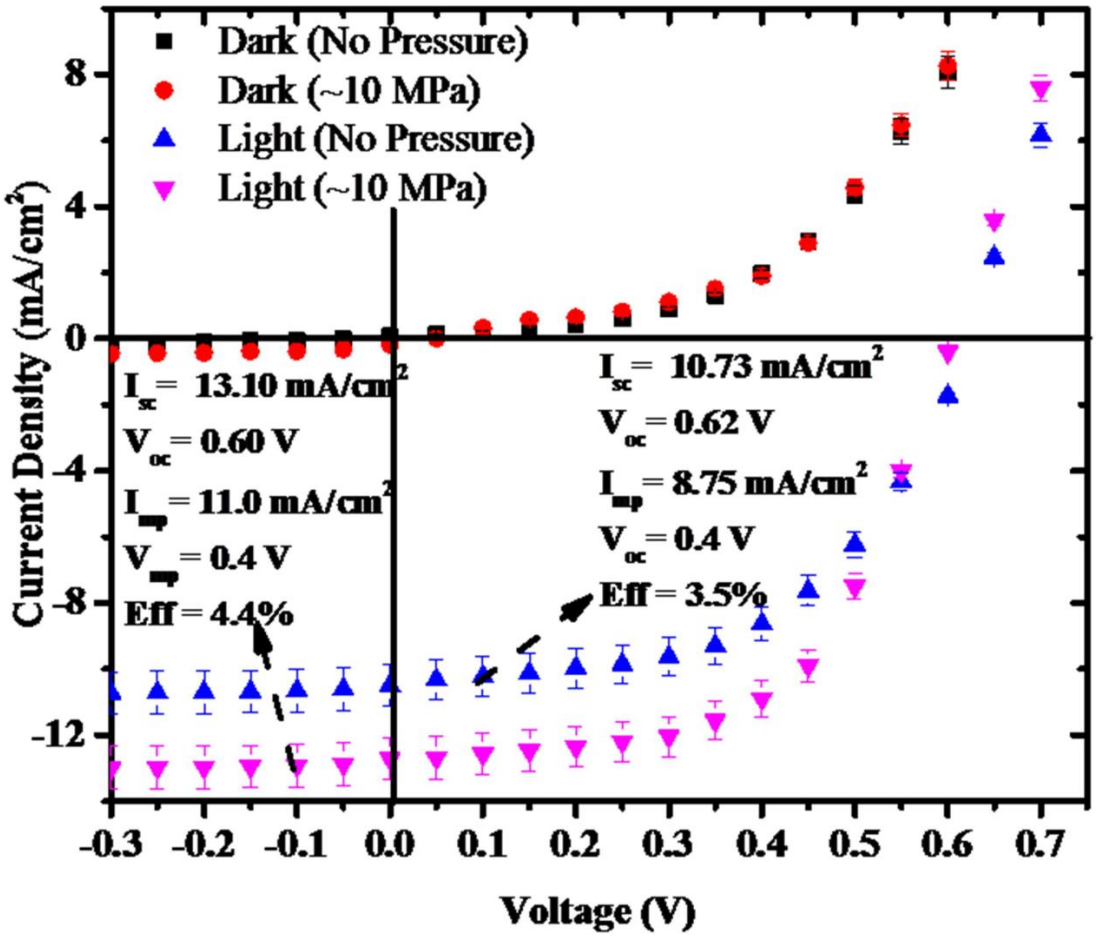

Figure 3.9 Power conversion efficiency and current-voltage characteristics of organic photovoltaic devices under pressure application.

Chapter 4

Investigation of nanoscale morphological changes in conjugated polymer photovoltaics cells during pressure application

4.1 Introduction

Large area solar energy conversion is possible using Organic Photovoltaic (OPV) cells due to the availability of low cost and sustainable energy materials sources. Blends of Conjugated polymers and fullerene have been used to produce Organic Photovoltaic cells from low cost sustainable energy materials sources.[1-7] OPV's with bulk heterojunction structures consisting of mixtures of P3HT polymers and fullerene based acceptors have recorded efficiency values ranging from ~6-7%.[4,5,8] However, these efficiencies degrade with time, making it challenging to adopt OPV's in practical applications. The relatively high hole mobilities of ~10^{-4} cm^2 $V^{-1}s^{-1}$ [9,10] and high electric field mobilities (~0.1 - 0.2 cm^2 $V^{-1}s^{-1}$)[11-14] of bulk heterojunctions OPVs have been attributed to improved charge hopping characteristics on the composite bulk-heterojunction structures,[15] as well as the effects of active layer crystallinity.[16-21] There is, therefore, a considerable interest in

the development of a fundamental understanding of how the structure and morphology of P3HT:PCBM blends contribute to their electrical and optical properties.[8]

Prior work has shown that the application of pressure during fabrication can have a significant effect on the performance of organic optoelectronic devices. These include studies of pressure effects on OPVs[22] and Organic Light Emitting Devices (OLEDs)[23-29] that show significant improvements in performance, following the application of pressure during the fabrication of devices on the soft and/or hard substrates.[28,31,32] The improvements in OLED performance have been attributed largely to increased surface contacts that enable improved charge and light transport across interfaces in these structures.[23-30] Prior work by Loo et al.[16,17,33] and Freichet et al.[18,19] have also shown the processing of bulk heterojunction layers with controlled crystallinity can be used to improve the efficiencies of bulk heterojunction solar cells.[33] However, we are not aware of prior work that relates pressure induced changes in the structure of bulk heterojunction solar cells to their optoelectronic performance.

Hence, the objective of this paper is to relate the pressure-induced changes in the nano- and micro-scale morphologies of blends of P3HT/PCBM to the current-voltage characteristics of bulk heterojunction solar cells. Pressure is applied using soft poly-di-methyl-siloxane (PDMS) stamps to improve the surface contacts, following the fabrication of models bilayers and multilayered OPVs with bulk heterojunction structures. The pressure-induced changes in polymer microstructure are characterized using Atomic Force Microscopy (AFM) and Grazing Incidence Wide Angle X-ray Scattering (GIWAXS). The implications of the results are discussed for the fabrication of bulk heterojunction OPVs with improved efficiencies.

4.2. MATERIALS AND METHODS

4.2.1 OPV Device fabrication and characterization

Single layer bulk heterojunction OPV devices (Figure 1), with P3HT:PCBM active layers, were fabricated from patterned ITO/glass substrates, (Sigma Aldrich, St. Louis, MO, R_s of 8-12 Ωsq^{-1}, and 120 nm thick). The ITO patterned substrate was washed for 10 minutes in a sparkleen detergent, in acetone, and in iso-propanol (IPA) in succession using the ultrasonicator and finally in the Ultra Violet Ozone Cleaning Systems (UVOCS, Lansdale, PA). Approximately 40 nm of Poly (3,4-ethylenedioxythiophene):poly(styrene-sulfonate) (PEDOT:PSS) was deposited under the conditions of 3000 rpm spin speed for 3 minutes. The film was dried and baked at 110 ^oC for 3 minutes on a hot-plate.

P3HT:PCBM blend of concentration, 20 mg/ml (1:1 ratio) in chlorobenzene, was deposited (at 700 rpm spin speed for 3 minutes) onto the PEDOT.PSS/ITO patterned glass substrates. (Rieke Metals Inc. USA and 1-Material Inc. Canada). The composite film (P3HT:PCBM/PEDOT.PSS/ITO/Glass) was then annealed at 140^oC for 4 minutes in an argon filled glove box in which the annealing temperature was monitored with a thermoresistor. About 0.2 nm of LiF was thermally evaporated unto the films before a back contact of aluminum films (with thickness of 150 nm) was thermally deposited. The device area of ~0.105 cm^2 was defined with the help of a shadow mask. The polydimethylsiloxane (PDMS) stamps were fabricated by blending the silicone elastomer base with a curing agent in a 10:1 weight ratio (Sylgard 184 Silicone, Dow Corning Corporation, Midland MI). The mixture was thoroughly mixed to ensure that air bubbles were removed and poured into a mold of 30 mm in diameter and 5 mm thickness. The mixture was cured in an oven at 100^oC for 35 minutes. The devices were loaded with PDMS stamp/dead weights and allowed for 5 minutes and tested. This was repeated for the

different pressure values (1 MPa, 3 MPa, 5 MPa, 8 MPa, 10 MPa and 15 MPa). In all, eight (8) devices were fabricated for each applied pressure and the current-voltage (I-V) behavior of the devices was recorded before and after the application of pressure.

4.2.2 Nano- and micro-structural evolution and polymer chain alignment

The effects of pressure on the nano-/micro-structures of the polymer blends were studied in an argon filled glove box. The polymer blend films on the glass substrate were stacked with PDMS stamp/dead weights for 5 minutes. This was repeated for the different pressure values (1 MPa, 3 MPa, 5 MPa, 8 MPa, 10 MPa and 15 MPa). The pressured films on glass substrate (1 cm × 1.25 cm) were annealed at 140^{o}C on a hot plate.

The changes in the nano-/micro- structures of the films were characterized using the Atomic Force Microscope (AFM, Dimension 3100, Digital Instruments, Nanoscope IV, Bruker, Plainview, NY, USA) and Grazing Incidence Wide Angle X-ray Scattering (GIWAXS) at the Brookhaven National Lab, Upton, NY, USA.

The surface morphological evolutions of the polymer blend films subjected to annealing and pressure was characterized with an AFM. The probes were made of silicon tips and the surface scans of the morphology were acquired over a 3 μm x 3 μm area in the tapping mode.

Finally, the polymer crystallinity, polymer chain alignments and the changes in the morphologies of the structures formed were observed in the films that were subjected to annealing and pressure application, prior to GIWAXS experiments at the Synchrotron, X9 undulator. These experiments were conducted with X-ray beams; 13.5 keV of energy, wavelength (λ) of 0.918 Å and an incident angle of 0.12^{o}. The scattering images in (two-dimensions) were captured with a charge couple device (CCD) and the GIWAXS detector positioned at 270 mm. Using silver behenate powder as the standard, the acquired data was converted to q-space.[20,21]

4.2.3 Optical characterization of P3HT and P3HT:PCBM films

Photoluminescence (PL), Ultraviolet-visible (UV-vis) and Raman spectroscopy techniques were used for the optical characterization of the polymer thin films. The absorption spectra of the pressured and pressure-less films were collected using a UV-Vis spectrophotometer (S.I. Photonics, Tucson-Arizona, USA). The (PL) characteristics of the thin films were also characterized using a Nd:YVO_4 laser with an excitation wavelength of 532 nm.

4.3 Results and Discussion

4.3.1 Effects of pressure on surface roughness and morphology

The effects of pressure on the surface morphologies of the films are presented in Figures 4.2 (a-f) using AFM images of the surfaces subjected to different pressure levels. The images show that, the film roughness generally decreased with increased applied pressure. Note that the pressure-less (Figure 4.2(a)) on a glass substrate had high surface roughness (R_a) of ~21.31±0.2 nm. The R_a for the pressured films (between 1 MPa and 5 MPa) was ~16.29±0.5 nm, while that of the films with 8 MPa and 10 MPa pressure were ~8.25±0.1 nm. Finally, the films produced with applied pressure values of 15 MPa or more had relatively smooth surfaces with R_a values of ~4.42±0.2 nm.

Observations from the AFM images show evidence of surface morphological changes with increasing applied pressure. The increased application of pressure appears to reduce surface roughness at the nano- and micro-scales and suggest that, the higher the pressure applied, the smoother the resulting films. The AFM results in Figure 4.2 show that the surface contacts depend on the surface roughness and the applied pressures. In the case of rough contact surfaces, multiple surface contacts can occur, giving rise to possible layer sink-in and short circuiting in

devices. Such layer sink-ins and partial contacts may degrade the charge transport between adjacent layers. In contrast, the surface morphologies at high applied pressures show relatively smooth surfaces. These should result in improved contacts between adjacent layers that will enhance charge transport across the interfaces.[31,32]

Therefore, the results indicate that, when the pressure applied is low, the morphology is coarser and higher pressures lead to smoother morphologies due to the fact that the polymer chains are stretched and they become orderly aligned. This results in improved crystallinity in the polymer blends.

4.3.2 Effects of pressure on absorption, photoluminescence and Raman spectra

Figure 4.3 presents the absorbance of the annealed and pressure assisted films. The region of absorption was in the visible range (350 nm <λ<650 nm) for P3HT and UV range for the PCBM (λ < 350 nm). The blended film (P3HT:PCBM), therefore, exhibited a wide absorption range between that of P3HT and PCBM.

The absorbance profile gives an indication of the intermolecular arrangements related to the crystalline and amorphous regions of the P3HT polymer. According to Miller et al,[2] peak positions of ~515 nm can be linked to the π-π* transition, while peak position of ~555 and ~605 nm can be linked to the stacking sequence of the polymer chains. Furthermore, from the Spano's model, [28, 29] the degree of interactions between the H-atoms in the conjugated polymer affects their crystallinity. Hence, crystalline regions form due to weak interactions and, therefore, the coupling of the polymer chains may produce bands in the absorption spectrum. These bands are a measure of the free exciton bandwidth. Inferences can also be made to determine the conjugation length of an individual polymer chain. Therefore, a reduction in the exciton bandwidth results in increases in the conjugation length and the chain order. The above arguments suggest that, the

chain alignments and conjugation lengths of P3HT polymer increase with annealing and the application of pressure (higher crystallinity). However, when P3HT is blended with PCBM, the free exciton bandwidth increases and leads to a reduction in the P3HT conjugation length and ultimately to a quenching of the absorption spectra. [2, 34, 35] This indicates that, the two components can interact actively upon blending. This reduces the absorbance of the P3HT/PCBM blend in the pressure-less condition (Figures 4.3(a) and 4.3(b)).

Furthermore, upon the application of pressure, the absorbance of the P3HT and the P3HT/PCBM polymer blends increased with increasing applied pressure (Figures 4.3(a) and 4.3(b)). Similar trends were also observed in the photoluminescence spectra.

Presented in Figure 4.4 for P3HT and P3HT:PCBM films subjected to applied pressure. P3HT exhibits high PL intensity, while PCBM greatly diminishes the PL response (Figures 4.4 (a-b)). The blend of P3HT with the PCBM shows the characteristics PL response of the two components. This is as a result of the increased interactions between the PCBM and the P3HT in the blend.[36,37] Clearly, the PL intensity for the pressured films increased with increasing pressure. However, the intensities of the polymer blends were weaker than those of pristine P3HT. This was due to the quenching effects of the PCBM.

A number of Raman peaks were observed in Figure 5. The 1380 cm^{-1} peak corresponds to C-S-C ring deformation, 1440 cm^{-1} corresponds to C-C bond stretching and 1520 cm^{-1} peak corresponds to C-L-C ring stretching respectively.[2] The scattering modes in the films before and after annealing could be estimated by Gaussian fitting the Raman spectra.[38,39] Hence, we can infer that annealing and pressure application increases the crystallinity of P3HT : PCBM. This is often observed in P3HT polymer stacking, where there is a segregation of the blend into PCBM-rich regions and the polymer stacking chains.[14,39]

4.3.3. Pressure effects on polymer chain alignment

The GIWAXS results obtained from the polymer blends are presented in Figures 4.6(a)-(f) for the different applied pressures. These show three strong reflection spots of P3HT:PCBM blends displayed on the GIWAXS 2D pattern. The diffraction peaks are also shown in the out-of-plane (Figure 4.7(a)), the (200) and the (300) peaks in an enhanced mode in Figure 4.7(b) and the stacking of the polymer chain in the edge-on-configuration in Figure 4.7(c). The lattice spacing associated with the crystal orientations for the P3HT:PCBM blends (Figure 4.7) show the polymer chain arrangements as well as the π-π* stacking distance in the dominant crystallographic directions; (100) in the out-of-plane and (010) in the in-plane.[36–41] The 1D line profiles of the out-of-plane direction identified three profound peaks at 0.408 $Å^{-1}$ and 0.806 $Å^{-1}$ and 1.215 $Å^{-1}$ and are assigned, respectively, to the (100), (200) and (300) oriented crystallites of P3HT. There were no identifiable peaks in the in-plane directions of the 1D line profiles.

There were no clear shifts in the positions of the reflection peaks with increasing pressure. However, enhanced intensities were observed and varied from ~500 a.u to ~25,000 a.u for the corresponding pressure range of 0 to ~15 MPa. This clearly shows that, the chains get steadily elongated in the pressure range between 0 MPa and ~10 MPa. Pressures values greater than 10 MPa increased the intensity levels greatly, implying a higher degree of crystallinity. However, the onset of layer sink-in and device damage is high beyond 10 MPa pressure. [23, 33]

The diffraction patterns shown in the GIWAXS measurements indicate that the polymer chains would align in the edge-on configuration. This is due to the interfacial interactions between the P3HT and the substrate.[21,31,32] Therefore, with the relatively high adhesion energy between the substrate (PEDOT.PSS) and the polymer blend (P3HT:PCBM) of ~2.9 J/m^2,[32] our findings confirm that, the polymer chains predominantly align in the edge-on orientations.

Furthermore, since this chain configuration in the polymer promotes hole transport, [31, 33] the application of pressure can be adopted (during OPV fabrication) to improve the elongation of the polymer chains and current-voltage characteristics of the bulk heterojunction OPVs. The current-voltage characteristics are discussed in the next section.

4.3.4 Current-Voltage characteristics of pressure assisted P3HT:PCBM-based organic photovoltaic cells

Plots of current density against voltage (I-V) are presented in Figure 4.8 and Table 4.1 for photovoltaic cells subjected to annealing and pressure application (0-15 MPa). The results show that pressure application leads to a significant improvement in current-voltage characteristics of the organic photovoltaic cells. In the case of the devices with no pressure application (OPV_0), the short circuit current (I_{sc}) was ~4.21 $mAcm^{-2}$, while the V_{oc} recorded was ~0.30 V resulting in a PCE of 0.05 %. However, upon pressure application, the I_{sc} increased to ~10.0 $mAcm^{-2}$ with a corresponding increase in the V_{oc} of 0.66 V. The devices; (OPV_1, OPV_3, and OPV_5) recorded marginal increases in PCE's. Pressures greater than 5 MPa thus (OPV_8, OPV_{10} and OPV_{15}) resulted in significant increases in the I-V characteristics. For example, OPV_8, OPV_{10} and OPV_{15} recorded I_{sc} of ~ 6.0, ~8.82 and ~10.00 $mAcm^{-2}$ respectively with their V_{oc} fairly constant at ~0.66 V. These represent efficiencies of ~2.45%, ~3.91% and ~4.65%. A significant increase of ~ 60% was recorded between OPV_8 and OPV_{10} and ~ 20% between OPV_{10} and OPV_{15} devices. The low performance of the control device stems from the fact that during the deposition of the solution based layers (PEDOT.PSS/ P3HT:PCBM) through spin coating technique, the films usually results in uneven coverage and may form blisters. The blisters results in partial/ reduced overall surface contacts between the layers. In this situation, charge hopping/tunneling mechanism dominates the performance of the device and because charge hopping/tunneling is an energy intensive process, the interfacial charge transport is limited. Upon pressure application,

the voids are closed, the blisters are flattened and the total surface contacts increase tremendously to allow for improved charge transport across the interface.

It is noteworthy that, the improvements in photoconversion efficiencies were associated with significant increases in the contact lengths.[22,23] The observed increases were due to the combination of pressure application, reduction in surface roughness and the improvement in the edge-on orientations of the P3HT polymers interspersed with PCBM crystallites. The polymer chains were stretched in the direction of the applied pressure, which reduced the lamellae spacing between the polymer units. Hence, the high degree of crystallinity in the polymer led to enhancements in the current-voltage response.

4.3.5 Implications

The above results have significant implications on the design and fabrication of organic photovoltaic devices with improved photoconversion efficiencies. First, they suggest that the PL intensity of the pressured films increases with increasing applied pressure. There was also a significant reduction in the PL quantum response of the PCBM/ P3HT blends. These occur due to improved charge mobility between P3HT polymers and the fullerene molecules. The improved photoconversion efficiencies are also associated with changes in polymer crystallinity. Hence, the controlled application of pressure can be used to significantly improve the photoconversion efficiencies of OPVs with bulk heterojunction structures. Further work is needed to optimize the processing parameters for the fabrication of such structures. These are clearly the challenges for future work.

4.4 Summary and Concluding Remarks

Organic Photovoltaic devices with enhanced efficiencies can be achieved by the manipulation of the nano- and micro-structures of the active layers in bulk heterojunction solar

cells. The results of the current experimental study of the changes in the structure of the P3HT/PCBM blends suggest that annealing and pressure application can be used to control the surface morphology, crystallinity and current-voltage characteristics of bulk heterojunction solar cells. Pressure application also results in the stretching of the polymer chains, predominantly in the edge-on configurations, with reduced lamellae spacing. The edge-on configuration induces polymer crystallinity, as well as significant enhancements in the current-voltage characteristics, and photoconversion efficiencies of the bulk heterojunction solar cells.

4.5 References

1. S. B. Darling, F. You, T. D. Veselka, A. Velosa: Assumptions and the levelized cost of energy for photovoltaics, *Ener. & Envir. Sci.*, **4** 3133–3139 (2011).
2. S. Miller, G. Fanchini, Y-Y Lin, C. Li, C-W Chen, W-F Su, and M. Chowolla, Investigation of nanoscale morphological changes in organic photovoltaics during solvent vapor annealing, *J. Mater. Chem.*, **18**, 306-312, (2008)
3. *Organic Photovoltaics: Mechanisms, Materials, and Devices*, ed. S.-S. Sun and N. S. Sariciftci, Taylor & Francis, London, (2005).
4. G. Li, V. Shrotriya, J. S. Huang, Y. Yao, T. Moriarty, K. Emery and Y. Yang, High-efficiency solution processable polymer photovoltaic cells by self-organization of polymer blends, *Nat. Mater.*, **4**, 864, (2005).
5. M. Reyes-Reyes, K. Kim and D. L. Carroll, High-efficiency photovoltaic devices based on annealed poly(3-hexylthiophene) and 1-(3-methoxycarbonyl)-propyl-1-phenyl-(6,6)61 blends. *Appl. Phys. Lett.*, **87**, 083506, (2005).
6. N. S. Sariciftci, L. Smilowitz, A. J. Heeger and F. Wudl, Photoinduced Electron Transfer from a Conducting Polymer to Buckminsterfullerene, *Science*, , **258**, 1474, (1992).
7. G. Yu, J. Gao, J. C. Hummelen, F. Wudl and A. J. Heeger, Polymer Photovoltaic Cells: Enhanced Efficiencies via a Network of Internal Donor-Acceptor Heterojunctions, *Science*, , **270**, 1789, (1995).
8. S.-H. Lee, J.-H. Kim, T.-H. Shim, J.-G. Park, Effect of Interface Thickness on Power Conversion Efficiency of Polymer Photovoltaic Cells, Electron. Mater. Lett. 5, **47**, (2009).

9. B. Ray and M. A. Alam, Random vs regularized OPV: Limits of performance gain of organic bulk heterojunction solar cells by morphology engineering, *Sol. Ener. Mat. & Sol. Cells*, **99**, 204–212, (2012).
10. S. Pandey, W. Takashima, S. Nagamatsu, T. Endo, M. Rikukawa, and K. Kaneto, Regioregularity vs regio-randomness: effect on photocarrier transport in poly(3-hexylthiophene). *Jpn. J. Appl. Phys.* **39(2)**, 94–97, (2000).
11. Z. Bao, A. Dodabalapur, and A. Lovinger, Soluble and processable regioregular poly(3-hexylthiophene) for thin film field-effect transistor applications with high mobility. *Appl. Phys. Lett.*, **69**, 4108 (1996).
12. H. Sirringhaus, N. Tessler, and R. H. Friend, Integrated optoelectronic Devices Based on Conjugated Polymers, *Science*, **280**, 1741, (1998).
13. A. Ullmann, J. Ficker, W. Fix, H. Rost, W. Clemens, I. McCulloch, M. Giles, High Performance Field –Effect Transistors and Integrated Inverters, Mat. Res. Soc., Symp. Proc. 665, **265** (2002).
14. O. Akogwu, W. Akande, T.Tong, and W. Soboyejo, Dendrite growth in annealed polymer blends for use in bulk heterojunction solar cells, *J. Appl. Phys.* **110**, 103517, (2011).
15. C. Deibel, V. Dyakonov, Polymer–Fullerene Bulk Heterojunction Solar Cells, *Rep. Prog. Phys.* **73**, 096401, (2010)
16. E. Pavlopoulou, C. S. Kim, S. S. Lee, Z. Chen, A. Facchetti, M. F. Toney, and Y-Lin Loo, Tuning the Morphology of All-Polymer OPVs through Altering Polymer−Solvent Interactions *Chem. Mater.* **26**, 5020−5027, (2014).

17. A. M. Hiszpanski, R.M. Baur, B. Kim, N. J. Tremblay, C. Nuckolls, A. R. Woll, and Y.-Lin Loo, Tuning Polymorphism and Orientation in Organic Semiconductor Thin Films via Post-deposition Processing, *J. Am. Chem. Soc*., **136,** 15749−15756, (2014).
18. D. S. Germack, C. K. Chan, R. J. Kline, D. A. Fischer, D. J. Gundlach, M. F. Toney, L. J. Richter, and D. M. DeLongchamp, Interfacial Segregation in Polymer / Fullerene Blend Films for Photovoltaic Devices, *Macromolecules*, **43**, 3828–3836 (2010).
19. C. H. Woo, B. C. Thompson, B. J. Kim, Michael F. Toney, and Jean M. J. Freichet, The Influence of Poly(3-hexylthiophene) Regioregularity on Fullerene-Composite Solar Cell Performance, 16324, **9,** *J. Amer. Chem. Soc.* 2008, *130*, 16324–16329, (2008).
20. C. E. Petoukhoff, D. M. O'Carroll, Absorption-induced scattering and surface plasmon out-coupling from absorber-coated plasmonic metasurfaces, *Nature Comm*. **6**, 7899, (2015).
21. Z. Shen, D. M. O'Carroll, Nanoporous Silver Thin Films: Multifunctional Platforms for Influencing Chain Morphology and Optical Properties of Conjugated Polymers, *Adv. Funct. Mater*. **25**, 3302-3313, (2015).
22. B. Agyei-Tuffour, E.R. Rwenyagila, J. Asare, O.K. Oyewole, M.G. Zebaze Kana, D.M. O'Carroll, W.O. Soboyejo, Influence of Pressure on Contacts Between Layers in Organic Photovoltaic Cells, *Adv. Mater. Res*. Vol. **1132,** pp 204-216, (2016).
23. J. Du, V. C. Anye, E. O. Vodah, T. Tong, M. G. Zebaze Kana and W. O. Soboyejo, Pressure-assisted fabrication of organic light emitting diodes with MoO_3 hole-injection layer materials, *Jr. Appl. Phys.*, **115**, 233703, (2014).
24. J. H. Kim, S. Seo, and H. H. Lee, Nanovoid nature and compression effects in organic light emitting diode, *Appl. Phys. Lett.* **90,** 143521, (2007).

25. M. Fina, D. Liu, L. Ren, and S. S. Mao, Improving organic light emitting diode performance with patterned structures, *Appl. Phys. A* **105**, 323–327, (2011).
26. X. Fan, J. Sun, F. Wang, Z. Chu, P. Wang, Y. Dong, R. Hu, B. Z. Tang, and D. Zou, Photoluminescence and electroluminescence of hexaphenylsilole are enhanced by pressurization in the solid state, *Chem. Commun.* , 2989–2991, (2008).
27. Z. Y. Jiang and X. A. Cao, Stress-induced current and luminescence modulations in an organic light-emitting device, *Appl. Phys. Lett*. **97**, 203304, (2010).
28. C. Kim and S. Forrest, Fabrication of organic light-emitting devices by low-pressure cold welding ,*Adv. Mater*. **15**, 541–545, (2003).
29. Y. Cao, C. Kim, S. R. Forrest, and W. Soboyejo, An Investigation of the Effects of Layer Thickness and Dust Particles on Cold Welding in Organic Electronics Fabrication, *J. Appl. Phys*. **98**, 033713, (2005).
30. J. Du, T. Tong, W. Akande, A. Tsakiridou, and W. Soboyejo, Pressure Effects on the Lamination of Organic Light-Emitting Diodes, *J. Disp. Technol.* **9**, 601–606 (2013).
31. Y. Guo, X. J. Ma and Z. H. Su, Interfacial Interactions between Poly(3-hexylthiophene) and Substrates, *Macromolecules*, **46**, 2733–2739 (2013).
32. T. Tong, B. Babatope, S. Admassie, J. Meng, O. Akwogu, W. Akande and W. O. Soboyejo: Adhesion in Organic Structures, *J. Appl. Phys.*, **106**, 083708, (2009).
33. W. Zhou, J. Shi, L. Lv, L. Chen and Y. Chen, A mechanistic investigation of morphology evolution in P3HT-PCBM films induced by liquid crystalline molecules under external electric field, *Phys. Chem. Chem. Phys*., **17**, 387-397, (2015).
34. K. Tremel, S. Ludwigs, Morphology of P3HT in Thin Films in Relation to Optical and Electrical Properties, *Adv Polym Sci.* **265**, (2014): 39–82, DOI: 10.1007/12_2014_288

35. M. Bockmann, T. Schemme, D. H. de Jong, C. Denz, A Heuer and N. L. Doltsinis, **Structure of P3HT crystals, thin films, and solutions by UV/Vis spectral analysis,** *Phys. Chem. Chem. Phys.*, 17, 28616, (2015)

36. S. E. Shaheen, C. J. Brabec, N. S. Sariciftci, F. Padinger, T. Fromherz, and J. C. Hummelen, 2.5% efficient organic plastic solar cells, *Appl. Phys. Lett.* **78,** 841 (2001).

37. T. Martens, J. D'Haen, T. Munters, Z. Beelen, L. Goris, J. Manca, M.D'Olieslaeger, D. Vanderzande, L. De Schepper, and R. Andriessen, Disclosure of the nanostructure of MDMO-PPV: PCBM bulk hetero-junction organic solar cells by a combination of SPM and TEM, *Synth. Met.* 138, **243** (2003).

38. M. Baibarac, M. Lapkowski, A. Pron, S. Lefrant and I. Baltog, SERS spectra of poly(3-hexylthiophene) in oxidized and unoxidized states", *J. Raman Spectrosc*., **29**, 825, (1998).

39. M. V. Klein, in Light Scattering in Solids, ed. M. Cardona, Springer-Verlag, Berlin, vol. **8**, (1975),

40. M. Campoy-Quiles, T. Ferenczi, T. Agostinelli, P. G. Etchegoin, Y. Kim, T. D. Anthopoulos, P. N. Stavrinou, D. C. Bradley, and J. Nelson, Morphology evolution via self-organization and polymer:fullerene solar cell blends, *Nature Mater.* **7**, 158, (2008).

41. D. Chirvase, J. Parisi, J. C. Hummelen, and V. Dyakonov, Influence of nanomorphology on the photovoltaic action of polymer:fullerene composites, *Nanotechnology* **15**, 1317 (2004).

42. M. Nakazono, T. Kawai, and K. Yoshino, Effects of heat treatment on properties of poly(3-alkyl)thiophene, *Chem. Mater*. **6,** 864 (1994).

43. F. Zhang, M. Svensson, M. Andersson, M. Maggini, S. Bucella, E. Menna, and O. Inga, Soluble polythiophenes with pendant fullerene groups as double cable materials for photodiodes, *Adv. Mater.* **13**, 1871, (2001).

44. N. Camaioni, G. Ridol, G. Casalbore-Miceli, G. Possamai, and M. Maggini, The Effect of a Mild Thermal Treatment on the Performance of Poly(3-alkylthiophene)/Fullerene Solar Cells. *Adv. Mater.*, ***14,*** 1735–1738, (2002).

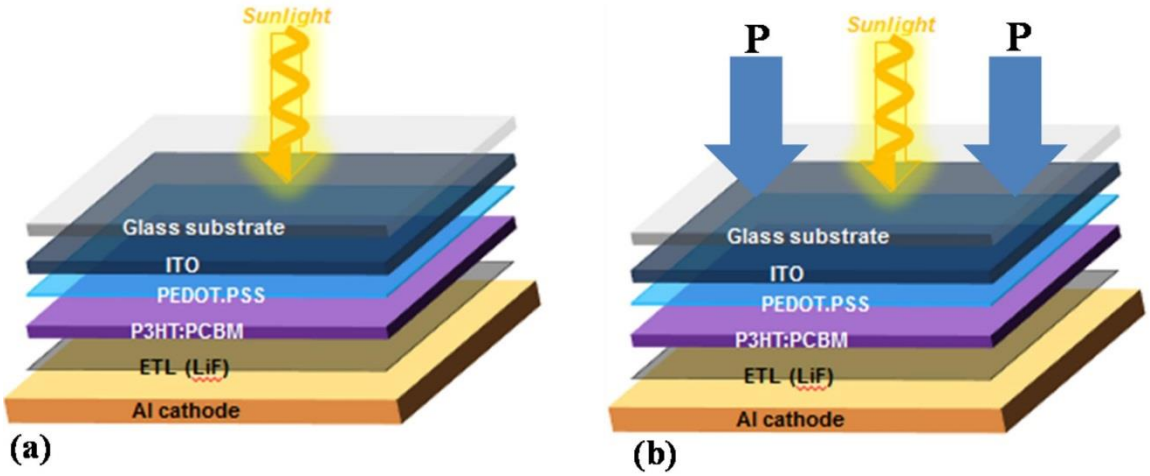

Figure 4.1 Organic photovoltaic cell layered structures: (a) without pressure and (b) with pressure.[22]

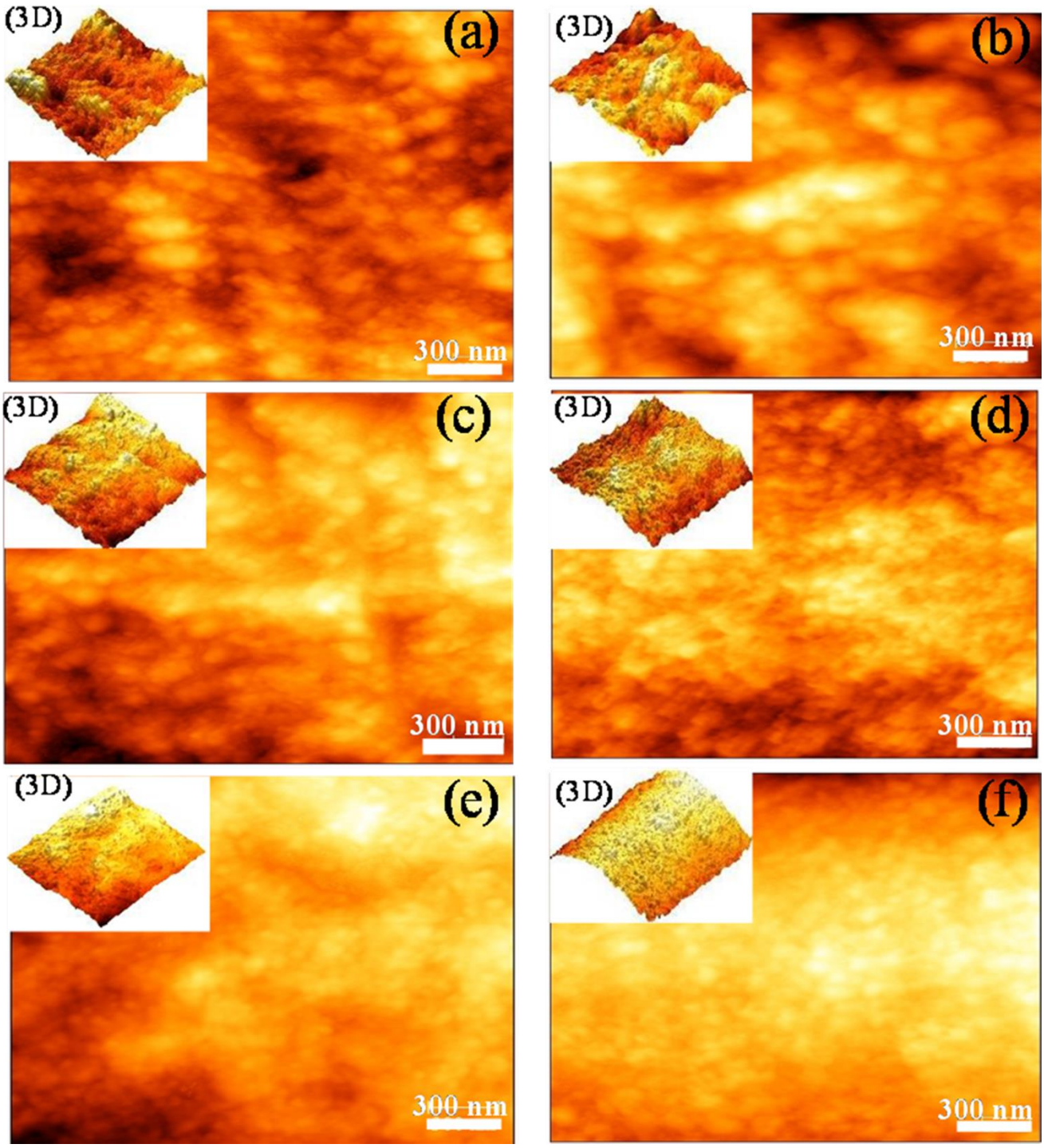

Figure 4.2 Surface morphology of P3HT:PCBM annealed and pressure assisted films : (a) pressureless film, (b) 1 MPa, (c) 3 MPa, (d) 5 MPa, (e) 8 MPa and (f) 10 MPa

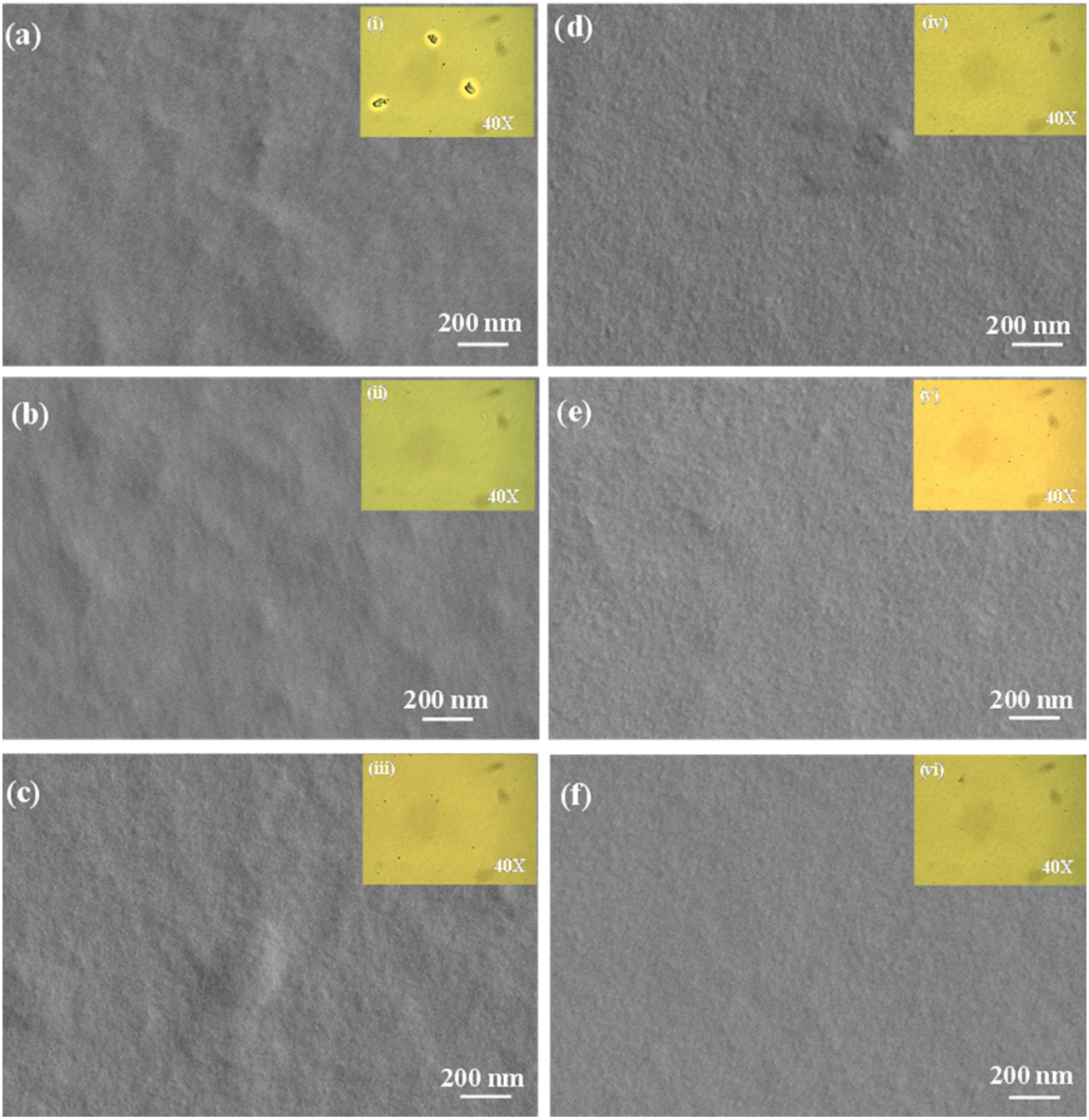

Figure 4.3 SEM images showing progressive growth of dendrites observed in P3HT:PCBM blends over a range of temperatures: (a) 25^{o}C, (b)50 ^{o}C, (c)70 ^{o}C, (d) 100 ^{o}C, (e) 150 ^{o}C, and (f) 200 ^{o}C.

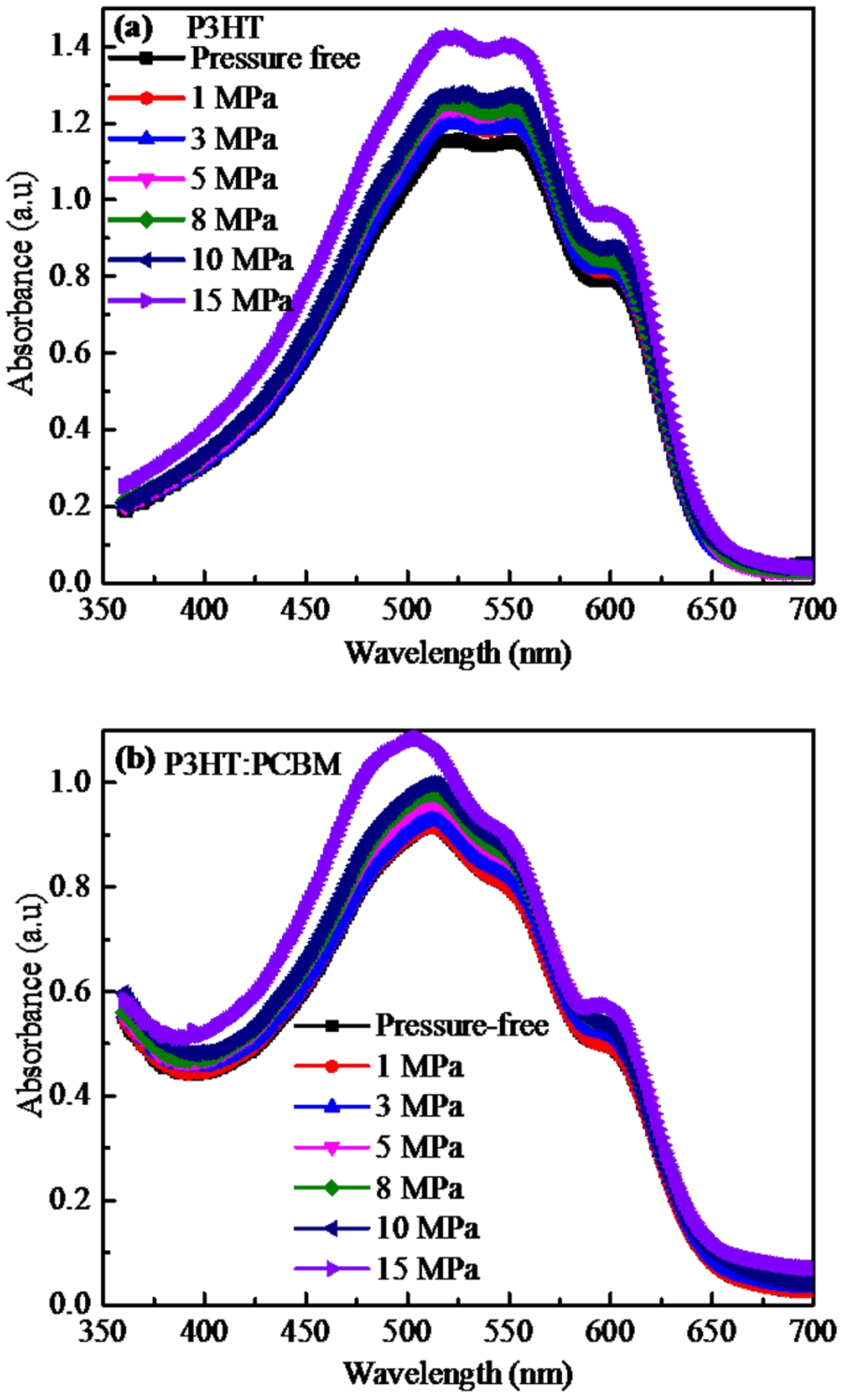

Figure 4.4 The optical properties and UV-vis absorption spectra of pressure assisted films: (a) P3HT and (b) P3HT:PCBM films.

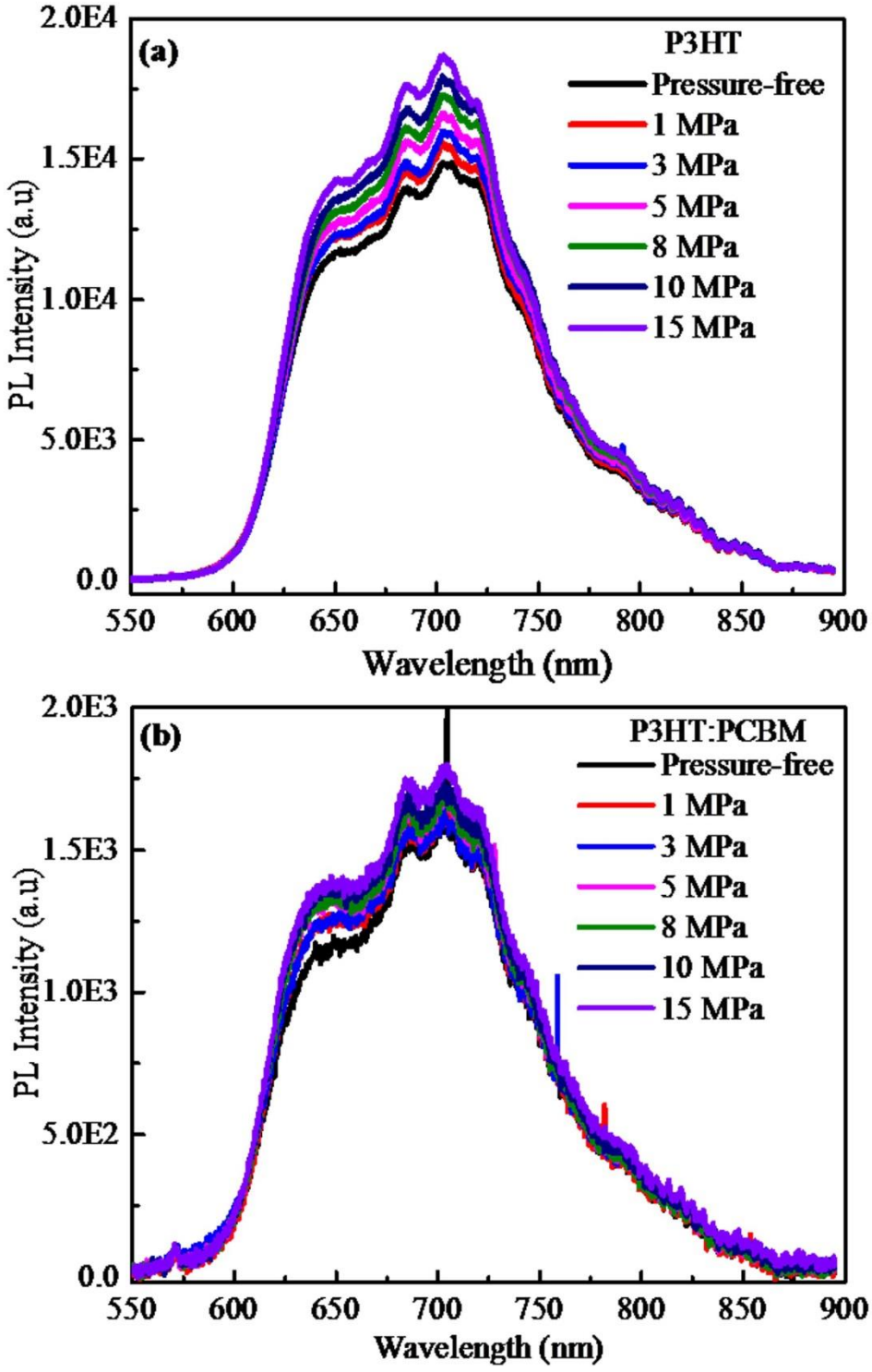

Figure 4.5 Photoluminescence (PL) spectra of the P3HT film, the blend film and the blends with pressure applied films: (a) P3HT and (b) P3HT:PCBM films.

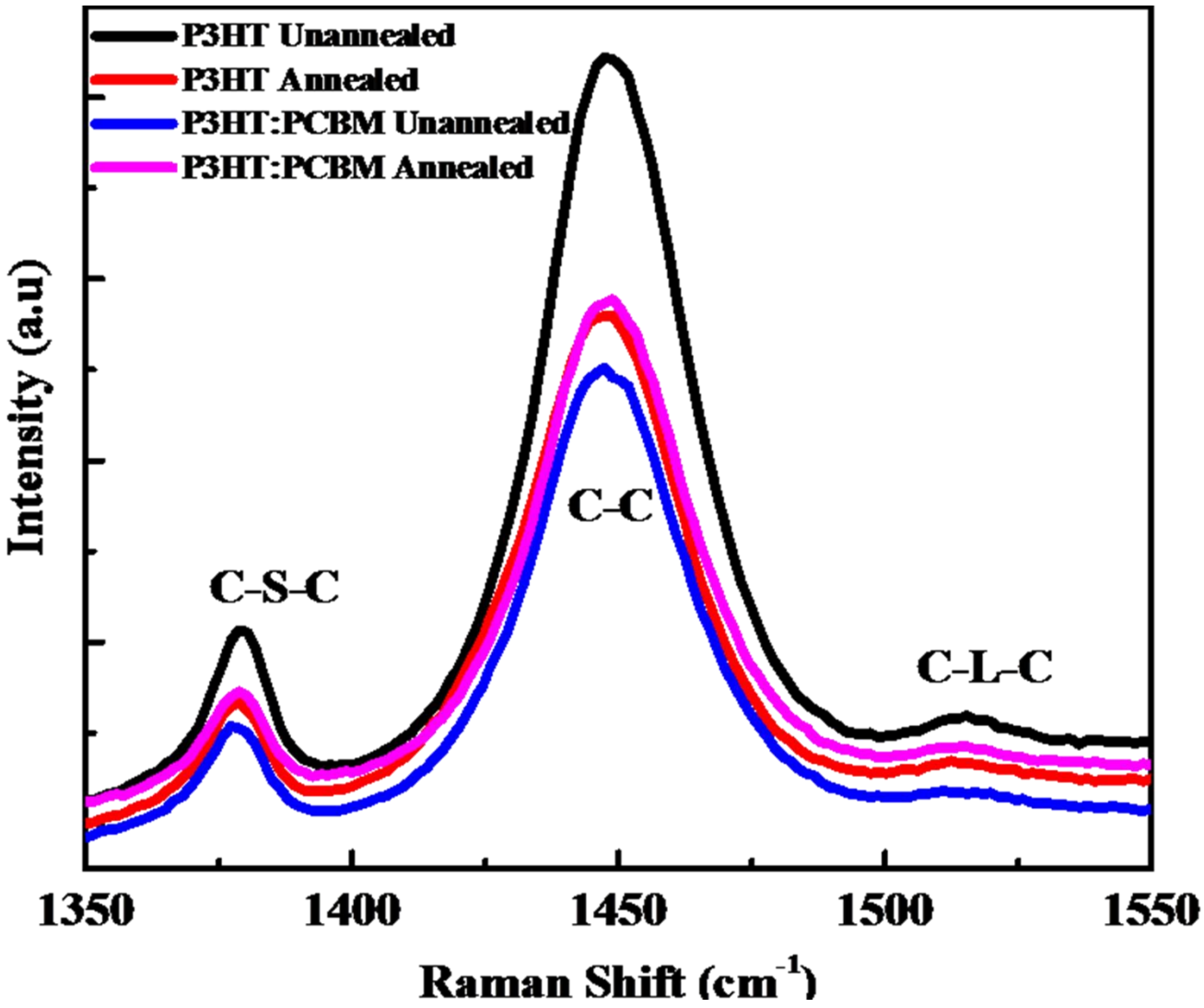

Figure 4.6 Raman spectra of P3HT and P3HT:PCBM films with and without annealing.

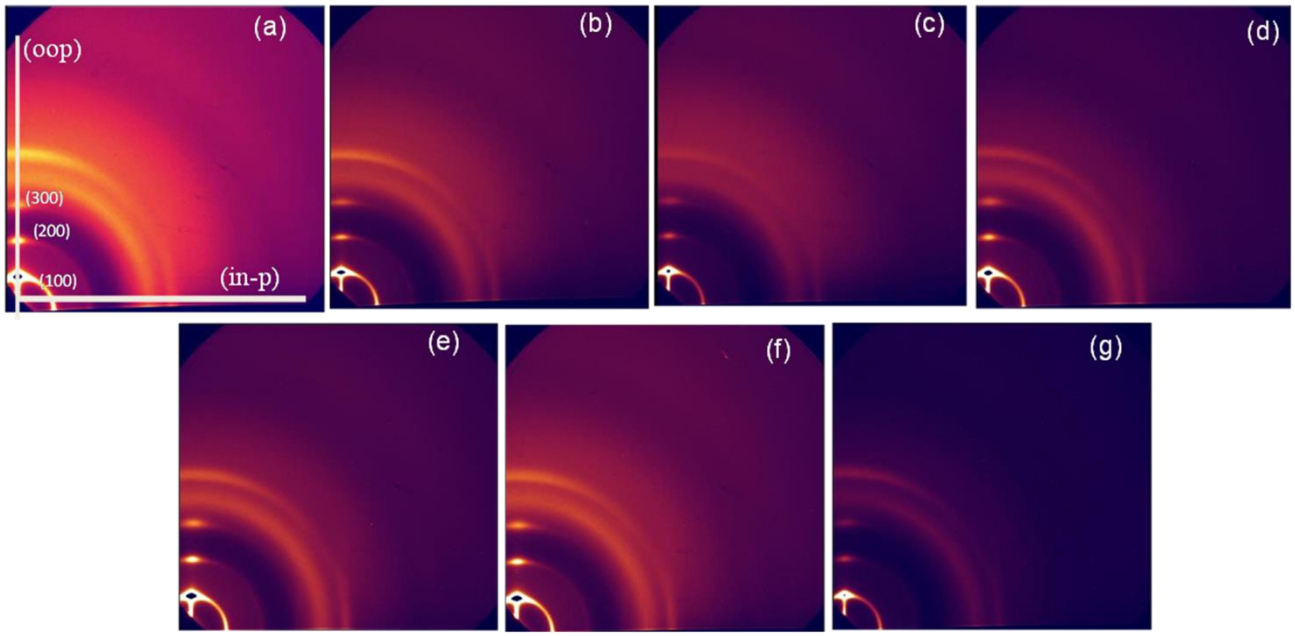

Figure 4.7 Two-dimensional GIWAXS images of the P3HT:PCBM films with different pressure application, (a) no pressure, (b) 1 MPa, (c) 3 MPa, (d) 5 MPa, (e) 8 MPa, (f) 10 MPa and (g) 15 MPa.

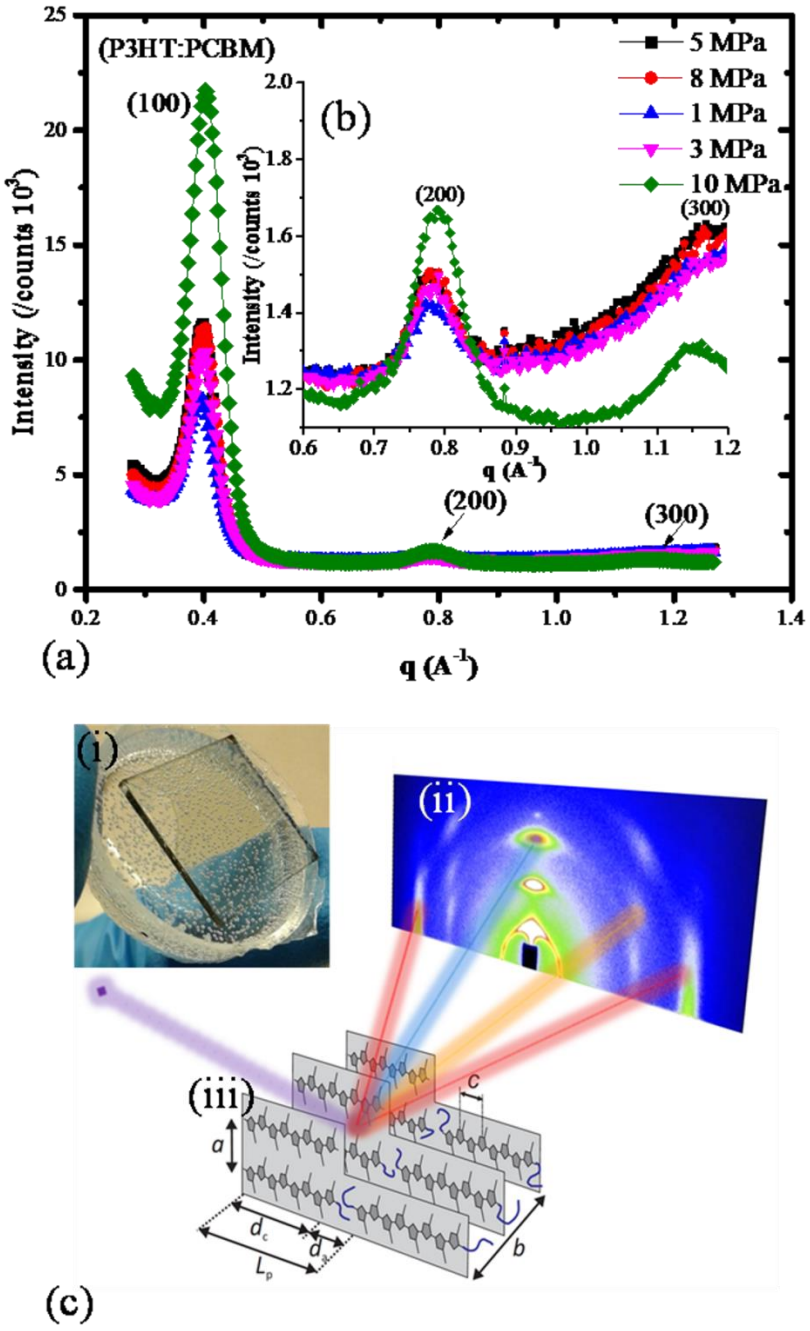

Figure 4.8 Line Profiles of the GIWAXS analysis; (a) in-plane profile (b) enhancement in the out-of-plane peaks and (c) schematic representation of the P3HT chains adopting an edge-on orientation.[21,31,33] The inserts show the schematics of the x-ray scattering imaging, the P3HT unit structure and the thin films with PDMS stamps used in the pressure application.

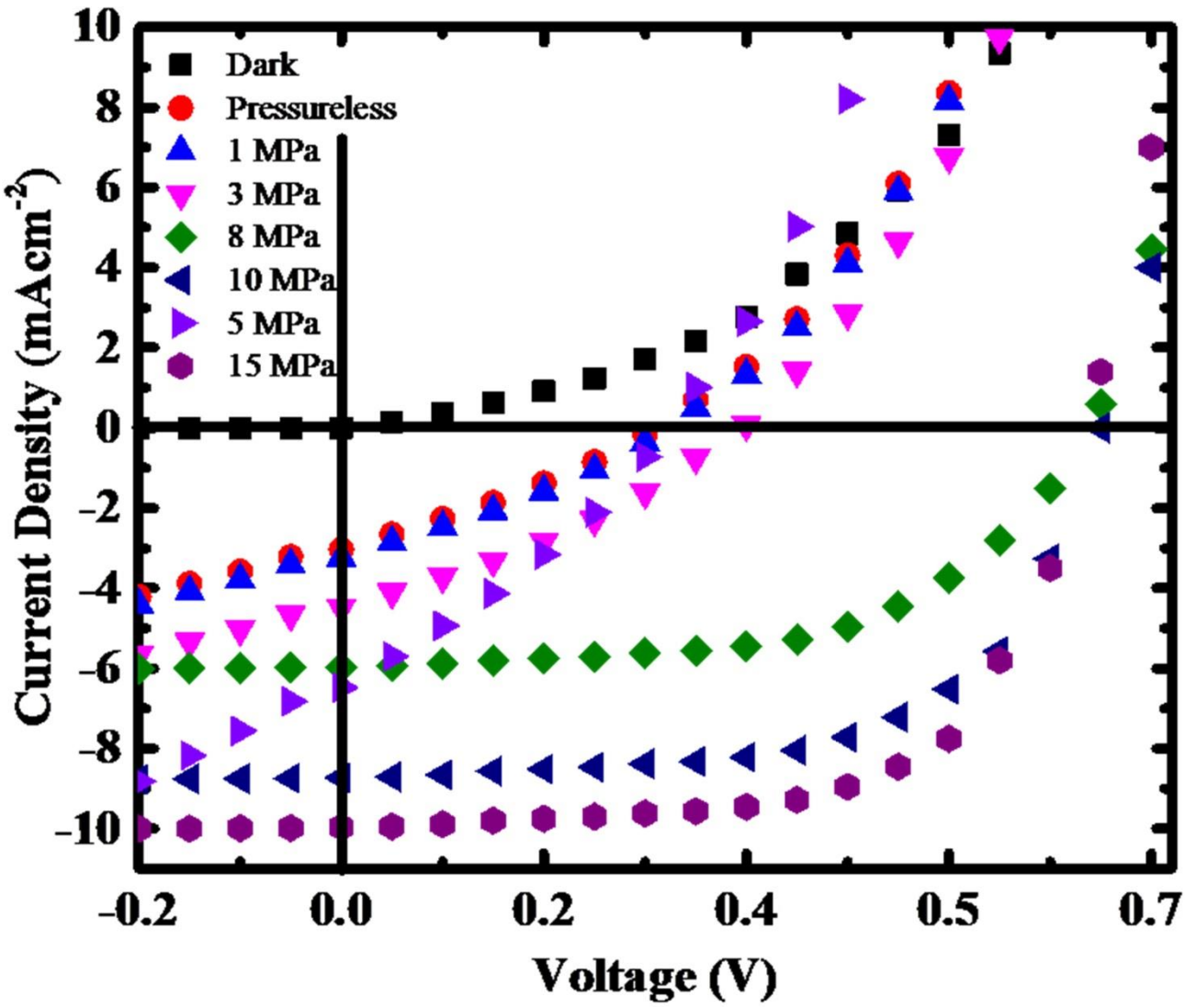

Figure 4.9 Current-voltage characteristics of the pressure assisted P3HT:PCBM based devices: (a) Pressure-less film (OPV_0), (b) 1 MPa (OPV_1), (c) 3 MPa (OPV_3), (d) 5 MPa (OPV_5), (e) 8 MPa (OPV_8), (f) 10 MPa (OPV_{10}) and (g) 15 MPa (OPV_{15}) films.

Chapter 5

Pressure Assisted Fabrication of Hybrid Photovoltaic cells

5.1 Introduction

Organic photovoltaic (OPVs) cells are promising low cost candidates for large-area solar energy conversion[1]. This is due to their attractive combinations of efficiencies (~5-10%) and potential for low temperature fabrication with relatively cheap organic materials. A typical OPV cell consists of an active layer material that is sandwiched between a transparent anode and a metallic cathode. The Hole Transport layer (HTL) is also sandwiched between the transparent anode and the active layer material. This facilitates the extraction of photo-generated holes and ensures that electrons flow into the opposite cathode. This results in improved performance of solar energy conversion efficiency.[2-4]

The most commonly used HTL layer is poly (3,4 ethylenedioxythiophene : poly (styrenesulphonate) (PEDOT.PSS) which is usually available in aqueous suspension and amenable to solution processing. However, this material is acidic and can therefore corrode both the substrate material and the processing equipment.[5, 10]. Furthermore, PEDOT.PSS is hygroscopic and its conductivity can change in the presence of moisture.[6] The work function of PEDOT.PSS is also sensitive to oxygen exposure[7] and it degrades significantly at temperatures

greater than 250^{o}C.[8-9]. Again, manufacturing additives to PEDOT.PSS have deleterious effects[10] while its electrical properties can degrade with exposure to oxygen and water.

Since the Lowest Unoccupied Molecular Orbital (LUMO) of PEDOT.PSS is only approximately 0.6 eV above the LUMO of P3HT, electrons can diffuse into the PEDOT.PSS layer and recombine with holes, thereby decreasing the device performance[11].

In contrast, inorganic anode HTL materials, based on transition metallic oxides, are generally more stable under ambient conditions[4]. They are therefore potential alternatives to PEDOT.PSS. Well known HTL layers include: nickel oxide (NiO),[11] vanadium pentoxide (V_2O_5), and molybdenum trioxide (MoO_3).[12] However, NiO and V_2O_5 materials need to be deposited under high vacuum and, therefore, cannot be easily scaled up for large-area manufacturing. However, MoO_3 can be deposited under ambient conditions.[13]

It is also known to enhance the injection of holes in organic light emitting diodes (OLEDS),[14-15] and more recently, as an HTL layer in OPV cells.[16-19] Furthermore, OPV cells with thermally evaporated MoO_3 have been shown to have improved reliability under ambient conditions.[17] However, thermal evaporation technique is limited to processing in small batches and not scalable for large-area manufacturing.[17]

Solution processing of MoO_3 is a possible route to scalable and inexpensive manufacturing.[16] However, it may result in uneven coverage, and the resulting devices do not always have consistent performance.[16] Furthermore, no current MoO_3 deposition techniques are compatible with nanostructured substrates,[20] which are often used in PV devices. This is because they tend to require planarized surfaces. This could be achieved by the application of pressure to the deposited layers. It may also be achieved by the transfer of planarized layers via lamination. This can be done to promote improved contacts, adhesion and charge transport across the

interfaces between MoO_3 layers and adjacent P3HT:PCBM or indium tin oxide (ITO) layers.

Hence, this paper explores the effects of pressure on the adhesion and contacts of deposited organic films with PEDOT.PSS and MoO_3 HTL materials. Applied pressures between 1 and 15 MPa were used to study the potential effects of pressure on contacts between layers that are relevant to the organic photovoltaic cells with PEDOT.PSS or MoO_3 improved HTL layers. The effects of pressure were also modeled using analytical and finite element approaches. The models show clearly that applied pressure and adhesion increased the contacts between the adjacent layers. The current-voltage characteristics of the organic photovoltaic cells are shown to improve with increased pressure, while those of the organic-inorganic solar cell do not change significantly with increased pressure. The implications of the results are discussed for the pressure-assisted fabrication of organic and organic-inorganic solar cells.

5.2. Models

5.2.1. Analytical Modeling of Surface Contacts and Adhesion

Dust particles in a typical semiconductor clean room environment include silicon, iron, aluminum, quartz, textile polymer, silicone, and photoresist.[22] The typical airborne dust particle diameter ranges from ~ 0.1 to 20 μm.[23-24] These are trapped at interfaces between adjacent layers during the fabrication of organic electronic devices. They can, therefore, affect the evolution of contact areas between adjacent layers. Prior work has also shown that applied pressure reduces the void lengths at interfaces between adjacent layers in organic photovoltaic cells [25] or cold welded interfaces in organic light emitting devices.[22, 25]

A number of analytical models[26,27] have been used to the study the contact profiles of the initial interfaces around trapped dust particles before the application of pressure. If we consider the contacts a membrane suspended on top of a particle, a blister with a radius, *a*, forms**,** as

shown in Figure 5.13. Malyshev and Salganik,[26] have solved this problem by idealizing the contact as that associated with a penny crack in bending. They obtained the following relationship between the adhesion energy, γ, and other key variables:

$$\gamma = \frac{2Et^3h^2}{3\left(1-\nu^2\right)a^4}, \tag{1}$$

where E is the Young's modulus and υ is the Poisson's ratio of the membrane material; t is the thickness of the membrane and h is the height of the blister under the beam. The height is also assumed to be equal to the diameter of the interposed particle. If the thickness of the suspended membrane is much smaller than the height and the radius of the blister, then membrane stretching dominates the mechanical energy instead of membrane bending.

It is clear from equation 1 that adhesion energies are needed for the estimation of contact lengths. These were obtained from prior atomic force microscopy (AFM) measurements in the literature.[28] The force microscopy measurements of adhesion force-displacement were combined with adhesion theories by Derjaguin, Muller and Toporov (DMT model),[29] and Johnson, Kendall and Roberts (JKR)[29-33] to obtain the adhesion energies from:

$$\gamma_{DMT} = -\frac{F_{adhesion}}{2\pi R} \tag{2}$$

$$\gamma_{JKR} = \frac{2F_{adhesion}}{3\pi R} \tag{3}$$

where $F_{adhesion}$ is the measured adhesion force and R is the effective contact radius. This is given by Tong *et al.*,[28] as:

$$R = \left(\frac{1}{R_{tip}} + \frac{1}{R_{rms}}\right)^{-1} \tag{4}$$

where R_{tip} and R_{rms} are radius of AFM tip and root-mean-squared (rms) roughness of the substrate. Since F_{ad} and R are known, we can estimate the adhesion energies of each of the interfaces in the layers of organic electronic structures.[28] The adhesion energies that were used in this study are presented in Table 5.1. Similarly, the Young's moduli of the dust particles that were used in the current work were obtained from prior reports in the literature (Table 6.2).

Considering a simple structure with a sandwiched dust particle between two layers of organic electronic materials, (Figure 6.1), the contact length can be estimated from Equation 1. In this problem, the dust particle of height is *h* before deformation, and l_1 and l_2 are the thicknesses of the two adjacent layers, where 1 and 2 designate layers 1 and layer 2, respectively. Prior to the deposition of the top layer (layer 1), it is assumed that the particle sits on layer 2, as shown below in Figure 1a. However, after deposition, provided that the thickness of layer 1 is greater than the height of the dust particle, the top layer covers the particle completely (Figure 2.13(a)).

The contact in Figure 6.1(a) can be idealized as an axisymmetric contact of a cantilever beam, as shown in Figure 1b in which the beam has a length, *L*, width, *w*, and thicknesses, t_1 and t_2. The resulting structure after the deposition of layer 1 is an s-shaped cantilever beam. The elastic energy, U_e, stored in the beam is given by:[31,32]

$$U_e = \frac{6EIh^2}{s^3} \tag{5}$$

where E is the Young's modulus, I is the second moment area of the beam, h is the height of the dust particle (after the deposition), and *s* is the void length (the length of the region in which there is no contact between the two layers). The surface energy, U_s, due to adhesion in the region of contact is given by:

$$U_s = -\gamma A_c \tag{6}$$

where γ is the adhesion energy. The contact area, A_c, can now be expressed as:

$$A_c = w \times L_c = w \times (L - s), \tag{7}$$

where L_c is the contact length. Thus, the surface energy becomes:

$$U_s = -\gamma w(L - s) \tag{8}$$

The total energy, U_T, of the system is the sum of the elastic energy stored in the beam, U_E, (equation 5) and the surface energy, U_S, (equation 6). This is gives:

$$U_T = U_S + U_E \tag{9}$$

$$U_T = \frac{6EIh^2}{s^3} - \gamma w(L - s) \tag{10}$$

The minimum total energy can be found by differentiating equation (10) with respect to *s*. This gives:

$$\frac{dU_T}{ds} = -\frac{18EIh^2}{s^4} + \gamma w \tag{11}$$

At equilibrium, $\frac{dU_T}{ds} = 0$, Hence, the adhesion energy is obtained by setting equation 11 to zero and rearranging the result to give:

$$\gamma = \frac{18EIh^2}{s^4 w} \tag{12}$$

where *I* is the second moment of area which is given by:

$$I = \frac{wt^3}{12} \tag{13}$$

Hence, substituting equation 13 into 12 now gives the adhesion energy, γ, and void length, *s*, as:

$$\gamma = \frac{3Et^3h^2}{2s^4} \tag{14}$$

and

$$s^4 = \frac{3Et^3h^2}{2\gamma} \tag{15}$$

Since the void length is related to the entire length of the beam, L, and the contact region of the two layers, L_c, the nominal contact length is given by:

$$s = \left(\frac{3Et^3h^2}{2\gamma} \right)^{1/4} = L - L_c \tag{16}$$

Hence, rearranging Equation 15 now gives the contact length ratio L_c/L to be:

$$\frac{L_c}{L} = 1 - \frac{1}{L}\left(\frac{3}{2}\frac{Et^3h^2}{\gamma} \right)^{1/4} \tag{17}$$

5.2.2. Numerical Modeling of Adhesion and Contacts

The modeling of contact and void lengths around the dust particles was also modeled numerically using the ABAQUS CAE 6.12 software package (ABAQUS™, Simulia, Pawtucket, RI, USA). The finite element simulations considered the contacts associated with different heights between 0.020 and 0.024 μm. A length of 200 nm, was used in the simulations, while the thicknesses of the P3HT:PCBM, PEDOT:PSS, MoO_3 and ITO layers were 120 nm, 40 nm, 3 nm and 120 nm, respectively. The thickness of the aluminum cathode layer was 150 nm. For simplicity, frictionless contact was assumed between the dust particle and the stamp, and also between the dust particle and the substrate.

However, rough contacts were used for the modeling of the two approaching layers.[5] This was used to account for the effects of layer roughness. It is also ensured that no relative sliding (between the two surfaces) after the contact occurred between the substrate and the stamping materials. The axisymmetric boundary condition (BC1) was applied at the symmetry axis and the

lowest part of the substrate was fixed to have no displacement and rotation (BC2). Also, the outer edge of the model was fixed to have no lateral movement for continuity. Then, the top of the stamp moved downward, as a result of the uniformly distributed pressure that was applied to the uppermost part of the stamp. The simulations were carried out for sandwiched dust particles between the active P3HT:PCBM layer and the PEDOT:PSS or MoO_3 layers. The parameters used in the finite elements simulations for sandwiched dust particles between PEDOT:PSS and MoO_3 based devices are presented in Table 3.3.

5.3 Experimental Procedures

5.3.1 Photovoltaic device fabrication and characterization

Model solar cell devices with the following layer architectures were fabricated: ITO/PEDOT:PSS/P3HT:PC60BM)/LiF/Al and ITO/MoO_3/(P3HT:PC60BM)/LiF/Al. These were used to investigate the influence of pressure on the current-voltage performance characteristics of the devices (Figure 5.2). First, patterned indium tin oxide (ITO) (8-12 Ω/sq resistance, Sigma Aldrich, St Louis MO, USA) was sequentially cleaned with acetone, ethanol and deionized water sequentially. After oven drying, the ITO surface was then treated with Ultra-Violet zone for 10 minutes. MoO_3 (Sigma Aldrich, St. Louis, MO, USA) was then thermally evaporated onto the ITO layers with an Edwards 306A evaporation system, (Edwards, Sussex, UK) at a deposition pressure of $4x10^{-6}$ mbar and a rate of 0.1 nm/s. Alternatively, PEDOT:PSS (Baytron P from H.C Stark, Inc.) solution was spin-coated onto the ITO at 3500 rpm for 60 s. This was then annealed at 120^{o}C for 10 minutes in air. The active layer was subsequently spin-coated at 700 rpm for 180 s. This was done from a solution of P3HT:PCBM (Rieke Metals Inc. and 1-Material Inc. Canada) (20 mg/mL, 1:1 weight ratio) in chlorobenzene. The P3HT:PCBM active layer was then annealed at 140^{o}C for 4 minutes in an argon filled glove box. The LiF (0.5 nm) and Al (150 nm)

layers were then thermally deposited in a deposition chamber at a vacuum pressure lower than $4x10^{-6}$ mbar.

The photovoltaic characteristics of the resulting devices were characterized with a Newport AM1.5 solar simulator that was operated at $100mWcm^{-2}$. This was done on devices with surface areas ~ 0.105 cm^2. The current-voltage characteristics were measured in the as-fabricated condition and also after the application of pressures ranging from 1 and 15 MPa using PDMS stamps and static loads.

X-ray photoelectron spectroscopy (XPS) spectra were collected from the deposited MoO_3 and the spin coated PEDOT:PSS films. This was done in a vacuum chamber that was pumped down to the base pressure ~10^{-8} mbar. This was done under excitation using a twin-anode Al *K-α* X-ray radiation source (*hν* ~ 1.486 keV) with an X-ray spot size of 15 μm and a spherical sector analyzer with multichannel detectors (Thermo Scientific, UK). During XPS, the samples were mounted on stainless steel stubs using double-sided adhesive tape. All of the XPS data were corrected for sample charging during X-ray irradiation using adventitious hydrocarbon referencing: E_b(C1s) = 284.8 eV. The surface morphology and surface roughness were also characterized with an atomic force microscope (AFM, Nanoscope III, Digital Systems) with a scan size of 3 μm x 3 μm and an aspect ratio of 1:1.

5.4. Results and Discussion

5.4.1 Layer Characterization of PEDOT.PSS and MoO_3

The presence of the thin PEDOT:PSS and MoO_3 layers was confirmed by the XPS results presented in Figures 5.3(a-c) and Figure 5.3(a-c). These show the full spectra for the PEDOT:PSS and the MoO_3, with the core level of PEDOT:PSS (S2p and O1s) and Mo ($Mo3d_{5/2}$ and $Mo3d_{3/2}$). The $Mo3d_{5/2}$ and $Mo3d_{3/2}$ peaks were located at 232.3 eV and 235.4 eV,

respectively. This coincides with the characteristic peaks of Molybdenum. The MoO_3 peaks observed for $Mo3d_{5/2}$ and O1s were not skewed, which suggested that good film conductibility could be achieved [34]. Furthermore, the S2p orbitals occurred at 164.2 eV and 168.5 eV. These are known to improve the optical properties and the electrical conductivities PEDOT:PSS as HTL material [38].

The surface morphologies obtained from the atomic force microscopy characterizations are presented in Figures 5.4 (a) and 5.4 (d). The average surface roughness values are also presented in Table 2.1. These show that the ITO coated glass (Figure 5.4(a)) had an average roughness of ~2.9±0.5 while the PEDOT.PSS layer (Figure 5.4(b)) has average surface roughness of ~ 0.8±0.1 nm, while the MoO_3 layer had an average roughness of ~ 0.7±0.3 nm (Figure 5.4(c)). The Al layer had an average roughness of ~ 2.4±0.4, respectively (Figure 5.4(d)). These roughnesses can have significant effects on the reflection, absorption and transmission of light at interfaces in the organic solar cells.

5.4.2 Analytical Modeling of Pressure Effects

The predictions of the void/contact length ratios obtained from the analytical models are presented in Figures 5.5(a) and 5.5(b). These show that, the contact length ratios increase with increasing pressure (Figure 5.5(a)), while the corresponding void length ratios decrease with increase pressure (Figure 5.5(b)). No significant reduction in the void length ratio was observed beyond about 99.95%, upon the application of pressure. The contact length ratios (Figure 5.5(c)) and the void length ratios (Figure 5.5 (d)) also depend strongly on the moduli of the upper layers that deformed around the trapped particles. Finally, the void length ratios, s, decreased with increasing adhesion energy, γ, (Figure 5.5(e)) while the contact length ratios, L_c/L, increased with increasing adhesion energy (Figure 5.5(f)).

The above results are consistent with results from prior work by Cao *et al*. [24] and Akande *et al*.,[36] who also reported significant improvements in the contact length ratios for the contacts between layers that relevant to the pressure assisted cold welding of layers in organic light emitting devices. However, the authors are not aware of any similar published analytical models of pressure effects on the contacts between adjacent layers that are relevant to organic photovoltaic cells. In any case, the results are consistent with prior experimental work on bulk heterojunction photovoltaic cells in which the application of pressure was shown to result in improved current-voltage characteristics that were attributed to the reduction of nanovoid sizes.[21] Hence, the results from the analytical model suggest that increased pressure increases the contacts between the active P3HT:PCBM layer and the Al cathode. However, excessive pressure can also lead to sink-in of the dust particles (Figures 5.6 and 5.7), which can result ultimately in the damage of organic electronic devices. Hence, moderate/intermediate pressures are needed to obtain the best balance of improved contact without excessive sink-in that can damage the device.

Furthermore, since the void length increases with increasing Young's modulus of the upper layer that wraps around the dust particles, suggests that lower modulus materials should be used for the stamps used in the pressure-assisted fabrication of organic photovoltaic cells. Hence, soft lamination processes can be assured with stamps made of poly-di-methyl-siloxane (PDMS) should be used for pressure application during the pressure-assisted fabrication of organic photovoltaic cells.

5.4.3 Finite Element Modeling of Pressure and Surface roughness Effects.

Typical predictions of stress distributions and surface contacts profiles are presented in Figures 5.6(a) – 5.6(f) for layer contact around dust particles. The results show that the surface

contacts depend on the surface roughness and the applied stresses. In the case of rough contact surfaces, Figure 5.6(a) – 5.6(f) show that multiple surface contacts can occur, giving rise to partial contacts even in regions remote from the dust particles. Such partial contacts may degrade the charge transport between adjacent layers. In contrast, the surface contacts between smooth layers result in simpler contact profiles (Figures 5.7(a-f)). The initially high stresses also reduce with increase deformation. Hence, the current results show that flat surface contacts required lower pressures to achieve good contact length ratios, while rougher surface contacts result in multiple partial contacts due to the surface topographies. Furthermore, increased sink-in of the dust particles (Table 2.2) was observed with increased pressure (greater than 10 MPa), which may lead ultimately to the damage of organic photovoltaic cells during pressure assisted fabrication.[21,24,36]

5.4.4 *Current-Voltage characteristics of Photovoltaic cells*

Plots of current density against voltage (I-V) obtained under AM1.5 illumination of 100mW/cm^2 presented in Figure 5.8 for solar cells with PEDOT.PSS or MoO_3 HTL layers. The effects of pressure application (≤ 10 MPa) are also presented in the same figure. The results show that pressure application leads to an improvement in current-voltage characteristics (Figure 6.8) of both types of solar cells.

In the case of the devices with PEDOT:PSS HTLs, the short circuit current (I_{sc}) also increased by more than 15% (from ~ 10.4 to ~ 12.0 mA/cm^2) while the fill factor increased from about 54.0 to ~56.5%, resulting in an efficiency increase from 3.8% to ~ 5.0%. This represents an increase of ~ 32.5% in the efficiency of the PEDOT:PSS based device. In the case of the MoO_3 device, an increase of ~ 5.9% (from ~7.48 - ~ 7.92mA/cm^2) was observed in the short-current upon pressure application, while the V_{oc} remained fairly the same. The power conversion

efficiency also increased by ~ 7.6% upon the application of pressure slightly lower than the PEDOT.PSS based device. It is important to note here that the devices with PEDOT.PSS HTL layers experienced increased contact compared to those containing MoO_3 active layers. Hence, the compliant nature of the PEDOT.PSS leads to an increase in surface contact (and reduced void size that can enhance charge transport. In contrast, hard and stiff layer leads to reduced surface contacts upon the application of pressure. This might explain the trends observed in the effects of pressure presented in Figure 6.8.

5.4.5 Implications

This study shows obviously that, the power conversion efficiencies and short circuit currents of OPVs are improved by the application of pressure for the different hole-injection layer based devices. The effects of pressure are attributed to the closing up of voids or the corresponding increase in the contact lengths. In any case, the contact lengths increase under pressure, while the void lengths decrease under pressure, resulting in increased contact area across the interfaces in the OPV structures. Hence, the higher power conversion efficiency in the OPVs that were fabricated using pressure-assisted processes is attributed largely to the increased contact area due to the application of pressure.

Hence, the current work suggests that the current-voltage characteristics of OPV can be enhanced by the application of controlled levels of pressure in lamination/-stamping processes. Such pressure may be applied after using conventional spin-coating and thermal evaporation techniques to deposit the individual layers in the OPV structures. However, great care is needed to ensure that the applied pressure does not result in excessive sink-in, which can lead to damage of the device. The required balance of improved contact without excessive sink-in should also be guided by computational models and some more experiments.

However, further work is clearly needed to explore the potential of other transition metal oxides as hole-injection layers in organic photovoltaic devices with the respective pressure effects. These include: V_2O_5, NiO or WO_3, that have been shown to have the potential to effectively replace PEDOT:PSS in organic photovoltaics (OPVs),[4,34] organic light emitting devices (OLEDs),[37-39] and organic thin film transistors (OTFTs).[40]

In addition to the above, the need to explore a range of deposition methods for the fabrication of organic layers in polymer based devices cannot be overemphasized. These include spin-coating, spray coating, self-assembled monolayers and thermal evaporation techniques that must be optimized prior to pressure-assisted fabrication. Such developments could facilitate the development of fast, low-cost stamping and roll-to-roll processes, [41] for the fabrication of organic photovoltaic devices. The current work suggests that these are possible, provided sufficient pressures are applied, without inducing significant damage (sink-in) in the layered structures of the devices.

5.5 Summary and Concluding Remarks

This paper presents the results of a combined analytical/computational and experimental study of pressure induced contacts between layers in organic photovoltaic cells with poly (3-hexylthiophene):phenyl-C61-butyric acid methyl ester (P3HT:PCBM) as the active layer and poly (3,4-ethylenedioxythiophene: poly styrenesulphonate (PEDOT.PSS) or molybdenum trioxide (MoO_3) as HTL layers. The contacts between the layers were modeled using analytical concepts and finite element models. The potential effects of surface roughness and dust particles were also considered along with the effects of pressure and adhesion energy.

The results show that, increased pressure is associated with decreasing void length or increased contact length. Increased pressure also results in improved power conversion

efficiency (from 3.79 to 5.02% for devices with PEDOT:PSS HTL and from 2.75 to 2.96% for devices with MoO_3 HTL subjected to 10 MPa pressure. The improvements are partly attributed to the increased surface contacts that occur with increasing pressure. However, these effects are reduced when the HTL materials are stiffer.

The current results suggest that pressure-induced contacts may be used to enhance the current-voltage characteristics and power conversion efficiencies of organic photovoltaic cells. However excessive pressure must be avoided to reduce the possibility of device damage due to sink-in of dust particles. The surface roughness of the device layers should also be reduced to improve the contacts between the layers.

5.6 References

1. S. B. Darling, F. You, T. D. Veselka, A. Velosa: Assumptions and the levelized cost of energy for photovoltaics, *Energy and Environmental Science* **4** 3133–3139 (2011).

2. S. A. Choulis, A. Patwardhan, M. K. Mathai, V. -E. Choong and F. So: Interface modification to improve hole-injection properties in organic electronic devices, *Advanced Functional Materials,* **16 (8)**, 1075–1080, (2006).

3. T. M. Brown, J. S. Kim, R. H. Friend, F. Cacialli, R. Daik and W. J. Feast: Built-in field electroabsorption spectroscopy of polymer light-emitting diodes incorporating a doped poly(3,4-ethylene dioxythiophene) hole injection layer, *Applied Physics Letters,* **75** (12), 1679–1681, (1999).

4. V. Shrotriya, G. Li, Y. Yao, C-W. Chu and Y. Yang: Transition metal oxides as the buffer layer for polymer photovoltaic cells, *Applied Physics Letters*, **88**, 073508, (2006). DOI: 10.1063/1.2174093

5. A. Cravino, P. Schilinsky and C. J. Brabec: Characterization of Organic Solar Cells: the importance of device layout, *Advanced Functional Materials*, **Vol. 17**, 3906–3910, (2007). DOI: 10.1002/adfm.200700295

6. Y. Kim, A. M. Ballantyne, J. Nelson and D. D. C. Bradley: Effects of Thickness and Thermal Annealing of the PEDOT:PSS Layer on the Performance of Polymer Solar Cells, *Org. Electron.,* **10**, 205–209, (2009).

7. A. W. Hains and T. J. Marks: High efficiency Hole extraction/electron-block layer to replace poly (3,4-ethylenedioxythiophene):poly(styrene sulfonate) in bulk-heterojunction polymer solar cells, *Applied Physics Letters*, **92**, 023504, (2008).

8. M. P. de Jong, L. Van Ijzendoorn, M. J. A Jandde Voigt: Stability of the interface between indium-tin-oxide and poly (3,4-ethylenedioxythiophene)/poly(styrenesulfonate) in polymer light-emitting diodes. *Appl. Phys. Lett*.**77**, 02255, (2000).

9. E. Vitoratos, S. Sakkopoulos, E. Dalas, N. Paliatsas, D. Karageorgopoulos, F. Petraki, S. Kennou S. A. Choulis: Thermal degradation mechanisms of PEDOT:PSS, *Organic Electronics* **10**, 61–66, (2009).

10. N. Sun, G. Fang, P. Qin, Q. Zheng, M. Wang, X. Fan, F. Cheng, J. Wan, X. Zhao, J. Liu, D. L. Carroll and J. Ye: Efficient flexible organic solar cells with room temperature sputtered and highly conductive NiO as hole-transporting layer, *J. Phys. D: Appl. Phys*., **43**, 445101, (2010).

11. J. Kettle, H. Waters, M. Horie and S-W Chan: Effect of hole transporting layers on the performance of PCPDTBT:PCBM organic solar cells. *J. Phys. D: Appl. Phys*. **45,** 125102, (2012).

12. R. Betancur, M. Maymo, X. Elias, L. T. Vuong and J. Martorell: Sputtered NiO as electron blocking layer in P3HT:PCBM solar cells fabricated in ambient air, *Solar Energy Materials and Solar Cells.*, **95,** 735–739, (2011).

13. J. Liu, X. Wu, S. Chen, X. Shi, J. Wang, S. Huang, X. Guo and G. He**:** Low-temperature MoO_3 film from a facile synthetic route for an efficient anode interfacial layer in organic optoelectronic devices, *J. Mater. Chem., C*, 2, 158-163, (2014).

14. H. You, Y. F. Dai, Z. Q. Zhang and D. G. Ma: Improved performances of organic light-emitting diodes with metal oxide as anode buffer. *Journal of Applied Physics.*, **101,** 026105, (2007).

15. W. J. Shin, J. Y. Lee, J. C. Kim, T. H. Yoon, T. S. Kim and O. K. Song: Bulk and interface properties of molybdenum trioxide-doped hole transporting layer in organic light-emitting diodes. *Organic Electronics*, **9**, 333–338, (2008).

16. L. Fengmin, S. Shuyan, G. Xiaoyang, Z. Yun and X. Zhiyuan: Efficient polymer photovoltaic cells using solution-processed MoO_3 as anode buffer layer, *Solar Energy Materials and Solar Cells*, **94**, 842–845, (2010).

17. Y. M. Sun, C. J. Takacs, S. R. Cowan, J. H. Seo, X. Gong, A. Roy and A. J. Heeger: Efficient, air-stable bulk heterojunction polymer solar cells using $MoO_{(x)}$ as the anode interfacial layer. *Advanced Materials*, **23**, 2226–2230, (2011).

18. J. H. Li, J. S. Huang and Y. Yang: Improved hole-injection contact for top-emitting polymeric diodes. *Applied Physics Letters*, **90**, 173505 (2007).

19. P. R. Brown, R. R. Lunt, N. Zhao, T. P. Osedach, D. D. Wanger, L.Y. Chang, M.G. Bawendi and V. Bulovic, Improved current extraction from ZnO/PbS quantum dot heterojunction photovoltaics using a MoO_3 interfacial layer, *Nano Letters*, **11,** 2955–2961, (2011).

20. Y.-C. Tseng, Q. Peng, L. E. Ocola, J. W. Elam and S. B. Darling: Enhanced block copolymer lithography using sequential infiltration synthesis. *Journal of Physical Chemistry C*., **115**, 17725–17729 (2011).

21. J. Du, V. C. Anye, E. O. Vodah, T. Tong, M. G. Zebaze Kana and W. O. Soboyejo: Pressure-assisted fabrication of organic light emitting diodes with MoO_3 hole-injection layer materials. *J. Appl. Phys.*, **115**, 233703, (2014).

22. International Organization for Standardization, ISO 14644-1:1999, Clean rooms of and Associated Controlled Environments-Part I: Classification of Air Cleanliness (ISO, Switzerland, 1999).

23. W. M. Moreau: Semiconductor Lithography: Principles, Practices, and Materials (Plenum Press, New York, 1988).

24. Y. Cao, C. Kim, S. R. Forrest, and W. Soboyejo: An Investigation of the Effects of Layer Thickness and Dust Particles on Cold Welding in Organic Electronics Fabrication. *J. Appl. Phys*,. **98**, 033713, (2005).

25. T. M. Tong: Adhesion and Interfacial Fracture: From Organic Light Emitting Devices and Photovoltaic Cells, PhD Thesis (Princeton University, 2012).

26. B. M. Malyshev and R. L. Salganik: The strength of adhesive joints using the theory of cracks *Int. J. Fract*., **26**, 261–275, (1984).

27. K. Wan and Y. Mai: Fracture mechanics of a shaft-loaded blister of thin flexible membrane on rigid substrate, *Int. J. Fract*. **74**, 181–197, (1995).

28. T. Tong, B. Babatope, S. Admassie, J. Meng, O. Akwogu, W. Akande and W. O. Soboyejo: Adhesion in Organic Structures, *Journal of Applied Physics*. **106**, 083708, (2009).

29. B. V. Derjaguin and V. M. Muller and Y. P. Toporov: Effect of contact deformations on the adhesion of particles, *J. Colloid Interface Sci.* **53**, 314–325. (1975)

30. K. L. Johnson, K. Kendall and A. D. Roberts: Surface energy and the contact of elastic solids, *Proc. R. Soc. Lond. A.* **324**, 301-313 (1971)

31. A. Bietsch and B. Michel: Conformal contact and pattern stability of stamps used for soft lithography. *J. Appl. Physics*. **88 (7)**, 4310-4318 (2000)

32. J. A. Greenwood: Adhesion of Elastic Spheres, *Proc. R. Soc. Lond*. A **453**, 1277-1297, (1997).

32. D. Maugis and M. Barquins and R. Courtel: Griffith's crack and adhesion of elastic bodies *Metaux-Corrosion-Industrie*, **605,** 1-10 (1976).

33. D. S. Grierson, E. E. Flater and R. W. Carpick: Accounting for the JKR–DMT transition in adhesion and friction measurements with atomic force microscopy, *J. Adhesion Sci. Technol*., **Vol. 19**, No. 3–5, pp. 291– 311 (2005).

34. Y-C. Tseng, A. U. Mane, J. W. Elam and S. B. Darling: Ultrathin molybdenum oxide anode buffer layer for organic photovoltaic cells formed using atomic layer deposition, *Solar Energy Materials and Solar Cells*, **Volume 99**, 235–239, (2012). doi:10.1016/j.solmat.2011.12.004

35. S.-S. Sun and L. R. Dalton, Introduction to Organic Electronic and Optoelectronic Materials and Devices (Optical Science and Engineering) 1st Edition, pp CRC, Press, (2008).

36. W. O. Akande, Y. Cao, N. Yao, and W. Soboyejo: Adhesion and the cold welding of gold-silver thin films. *J. Appl. Phys*. **107**, 043519, (2010).

37. K. J. Reynolds, J. A. Barker, N. C. Greenham, R. H. Friend, and G. L. Frey, Inorganic solution-processed hole-injecting and electron-blocking layers in polymer light-emitting diodes *J. Appl. Phys.* **92**, 7556, (2002).

38. H. You, Y. Dai, Z. Zhang, and D. Ma: Improved performances of organic light-emitting diodes with metal oxide as anode buffer. *J. Appl. Phys.* **101**, 026105, (2007).

39. W.-J. Shin, J.-Y. Lee, J. C. Kim, T.-H. Yoon, T.-S. Kim and O.-K. Song: Bulk and interface properties of molybdenum trioxide-doped hole transporting layer in organic light-emitting diodes, *Organic Electronics*, **9**, 333–338, (2008).

40. C.-W. Chu, S-H. Li, C.-W. Chen, V. Shrotriya, and Y. Yang: High-performance organic thin-film transistors with metal oxide/metal bilayer electrode. *Appl. Phys. Lett*. **87**, 193508, (2005).

41. S. R. Forrest: The path to ubiquitous and low-cost organic electronic appliances on plastic**.** *Nature,* **428**, 911–918, (2004).

42. W. Soboyejo: Mechanical Properties of Engineered Materials (CRC, New York, 2003).

43. W. D. Callister: Materials Science and Engineering: An Introduction (Wiley, New York, 2003).

Table 5.1 Short circuit current density (I_{sc}), open-circuit voltage (V_{oc}), fill factor (FF) and power conversion efficiency (PCE) based on MoO_3 devices with and without the influence of pressure.

OPV Device	V_{oc} (V)	I_{sc} (mA/cm^2)	FF (%)	PCE (%)
PEDOT.PSS (No pressure)	0.72	10.71	54.0	3.79
PEDOT.PSS (pressure)	0.74	11.98	56.5	5.02
MoO_3 (No pressure)	0.67	7.48	54.9	2.75
MoO_3 (pressure)	0.68	7.92	55.0	2.96

Figures

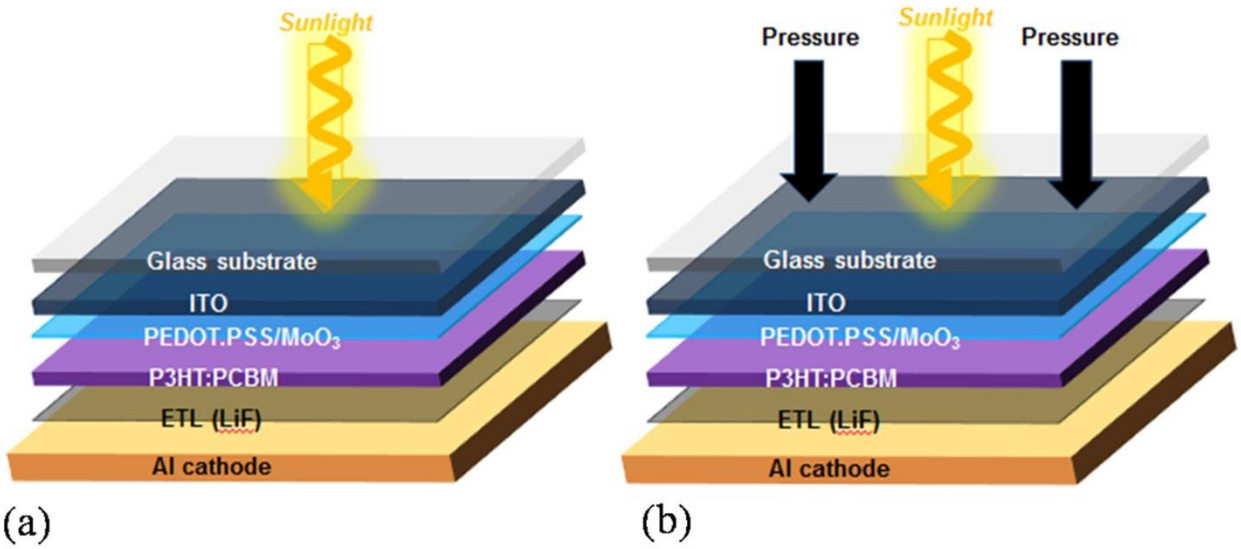

Figure 5.1 Organic photovoltaic cell layered structures based on PEDOT.PSS and MoO_3 HTL layer materials (a) without pressure and (b) with pressure.

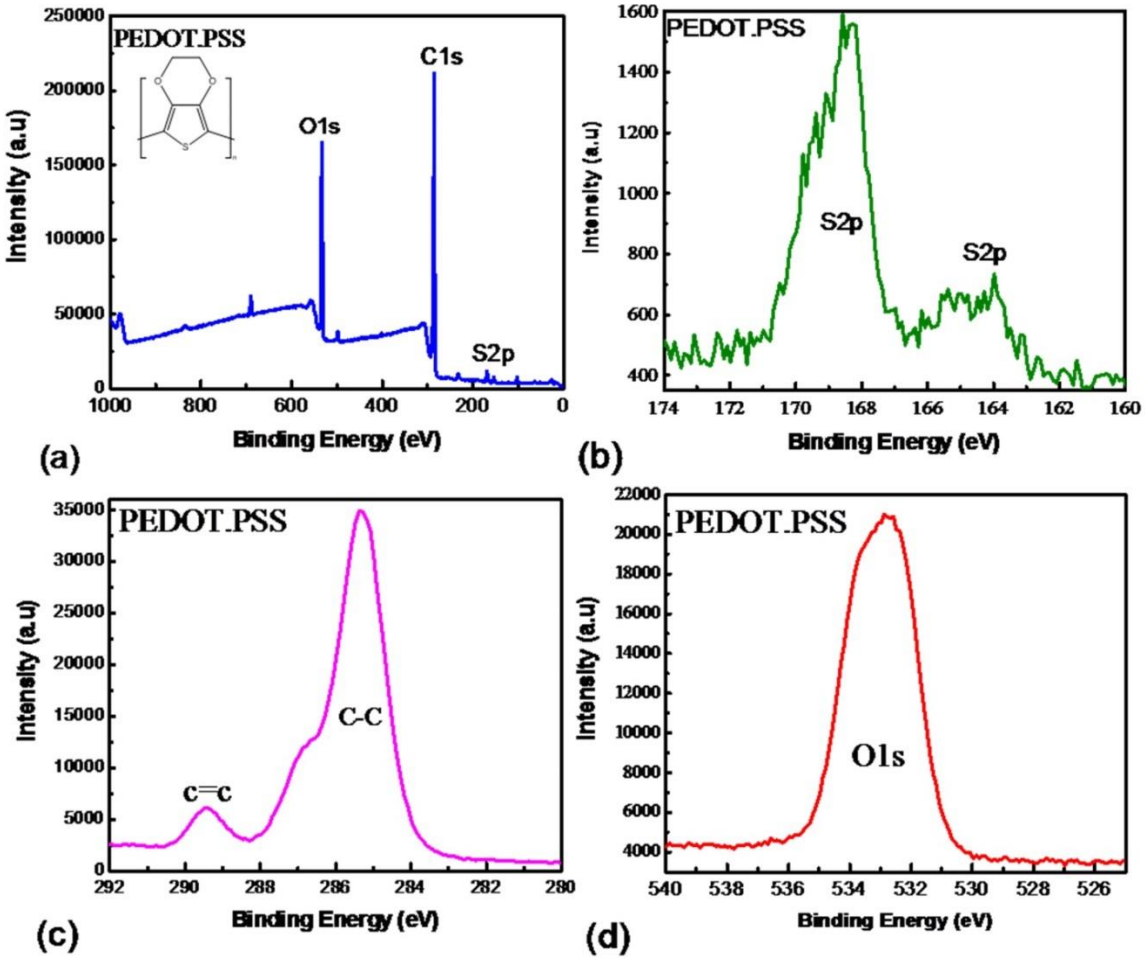

Figure 5.2 XPS spectra of the PEDOT.PSS films. (a) Full scanned spectra, (b) S2p core level of the polymer), and (b) C1s level carbon (single and double bonds of the aqueous solution PEDOT.PSS (d) O1s core level of the oxygen atoms in the PEDOT.PSS film

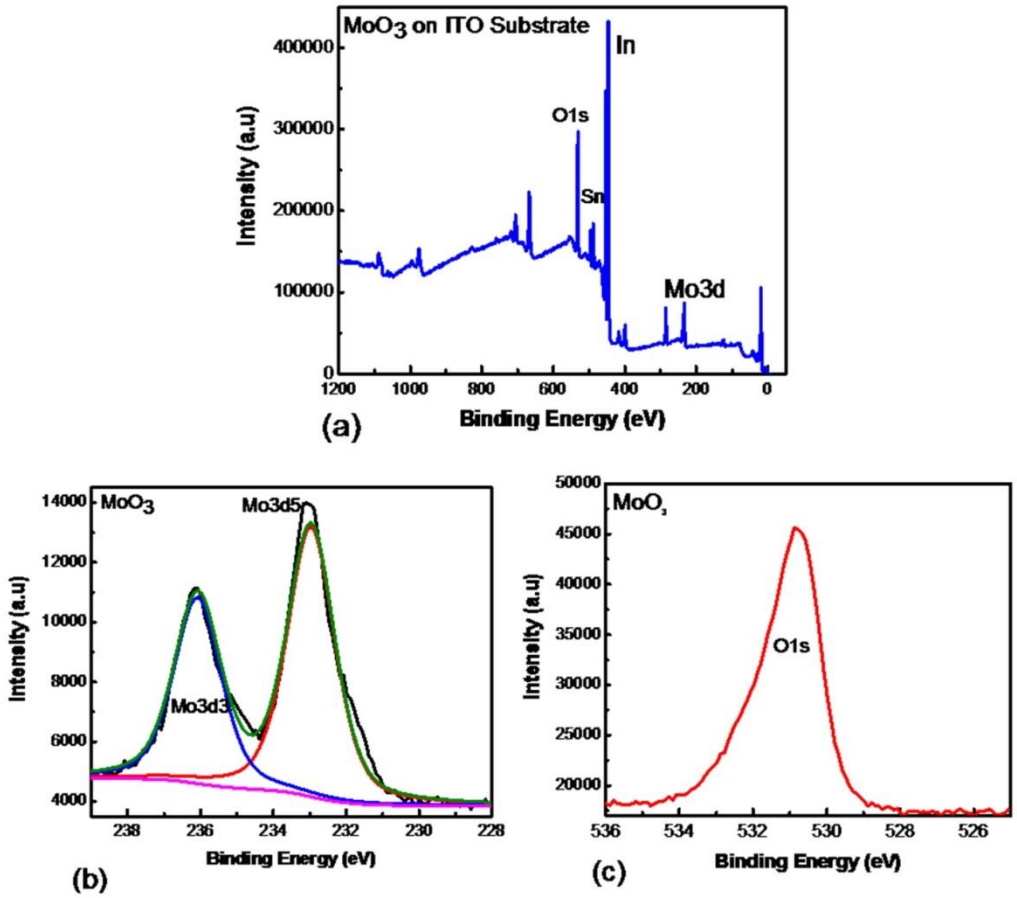

Figure 5.3 XPS spectra of the MoO_3 films on ITO substrate. (a) Full scanned spectra, (b) Mo 3d core level of the thermally evaporated MoO_3 and (c) O1s core level of the MoO_3.

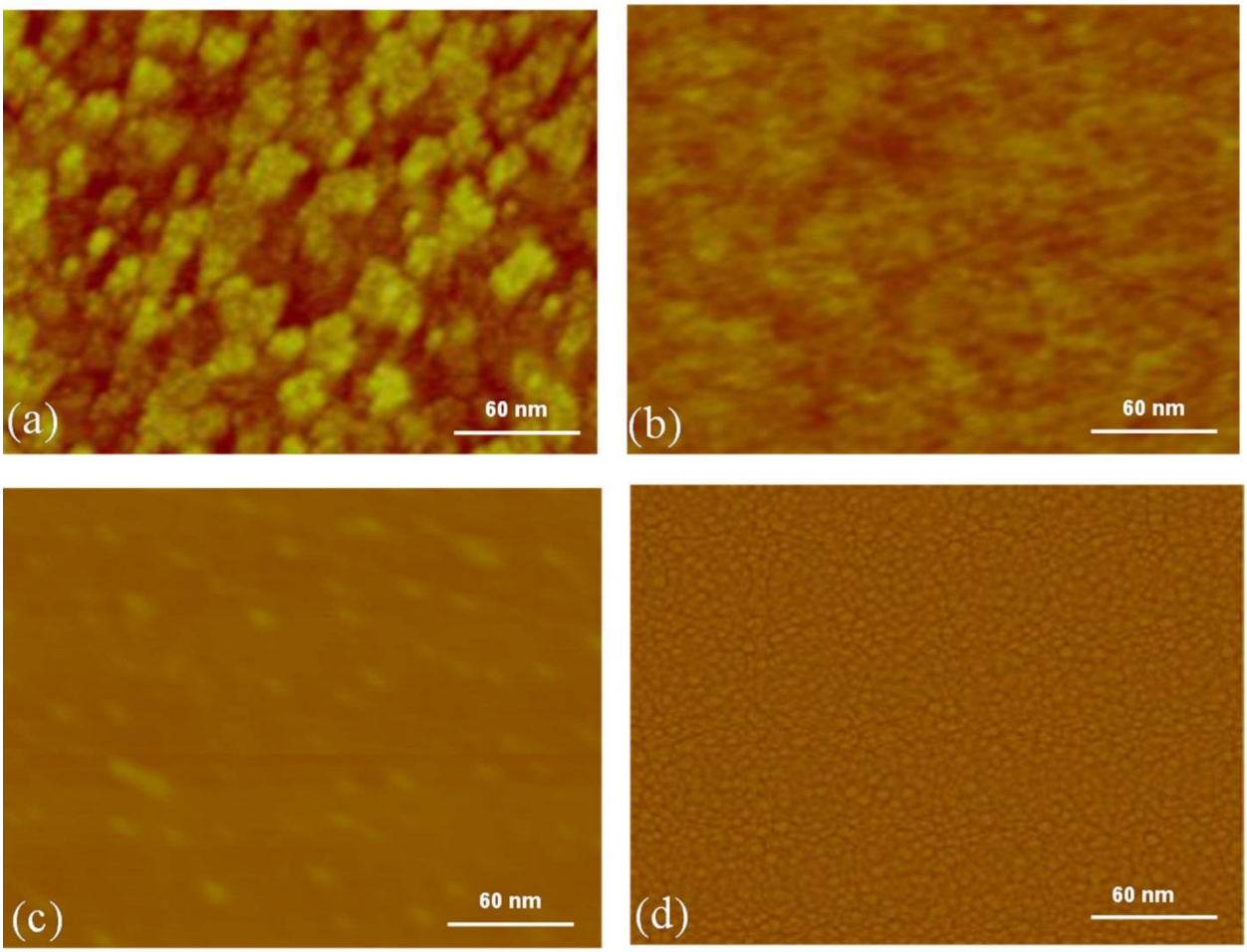

Figure 5.4 Sample AFM images (tapping mode 3µm x 3µm) for different layers in OPV structures: (a) ITO-coated glass, (b) PEDOT:PSS on glass, (c) MoO_3 on glass, (d) Al on glass

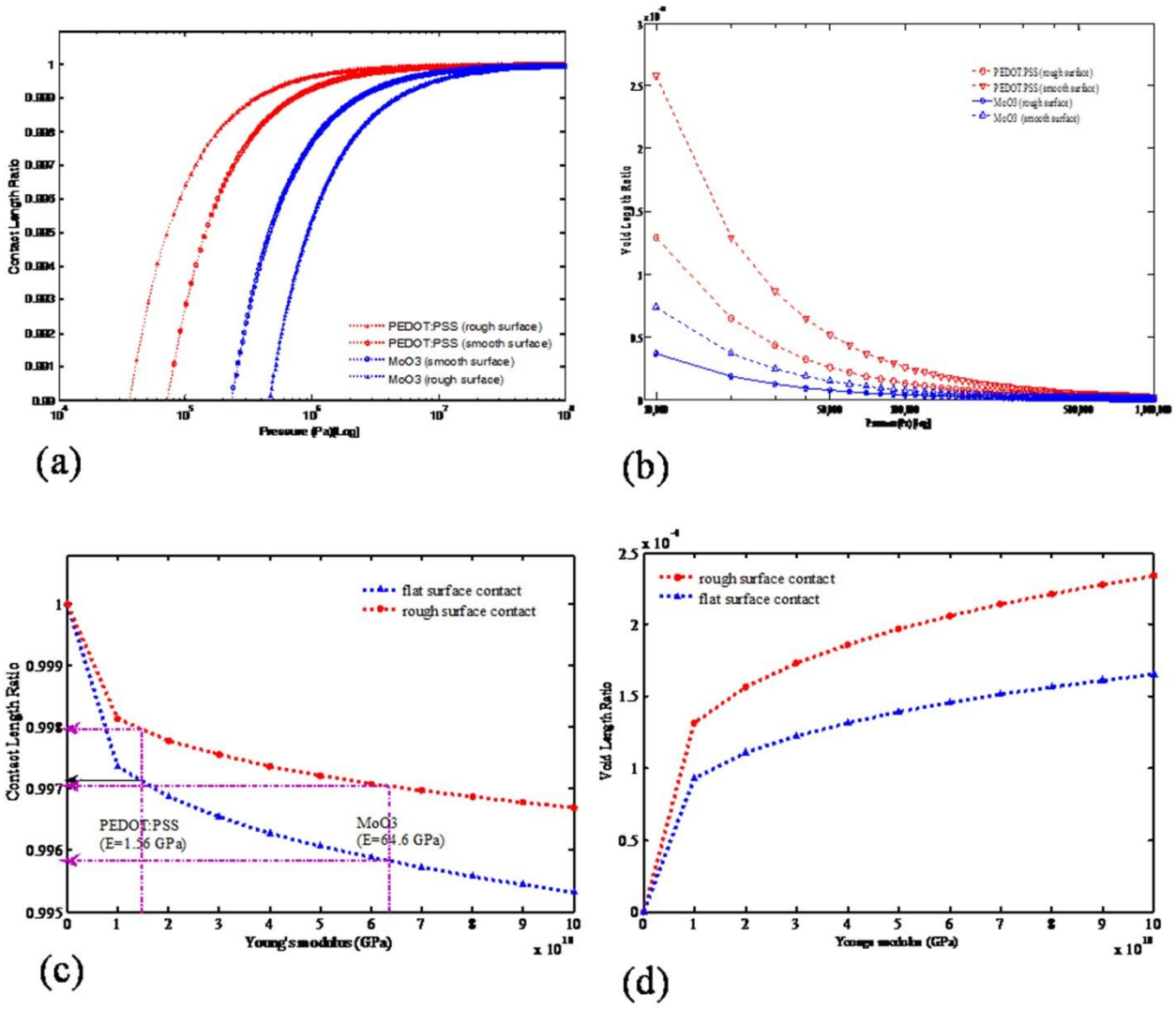

Figure 5.5 Effects of pressure, young's moduli and surface contacts on: (a) contact length ratios predicted by the analytical model; (b) void length ratios due to pressure, (c) contact length ratios due to Young's moduli of PEDOT:PSS and MoO_3 and (d) void length ratios due to young's moduli of PEDOT:PSS and MoO_3 upper layer films.

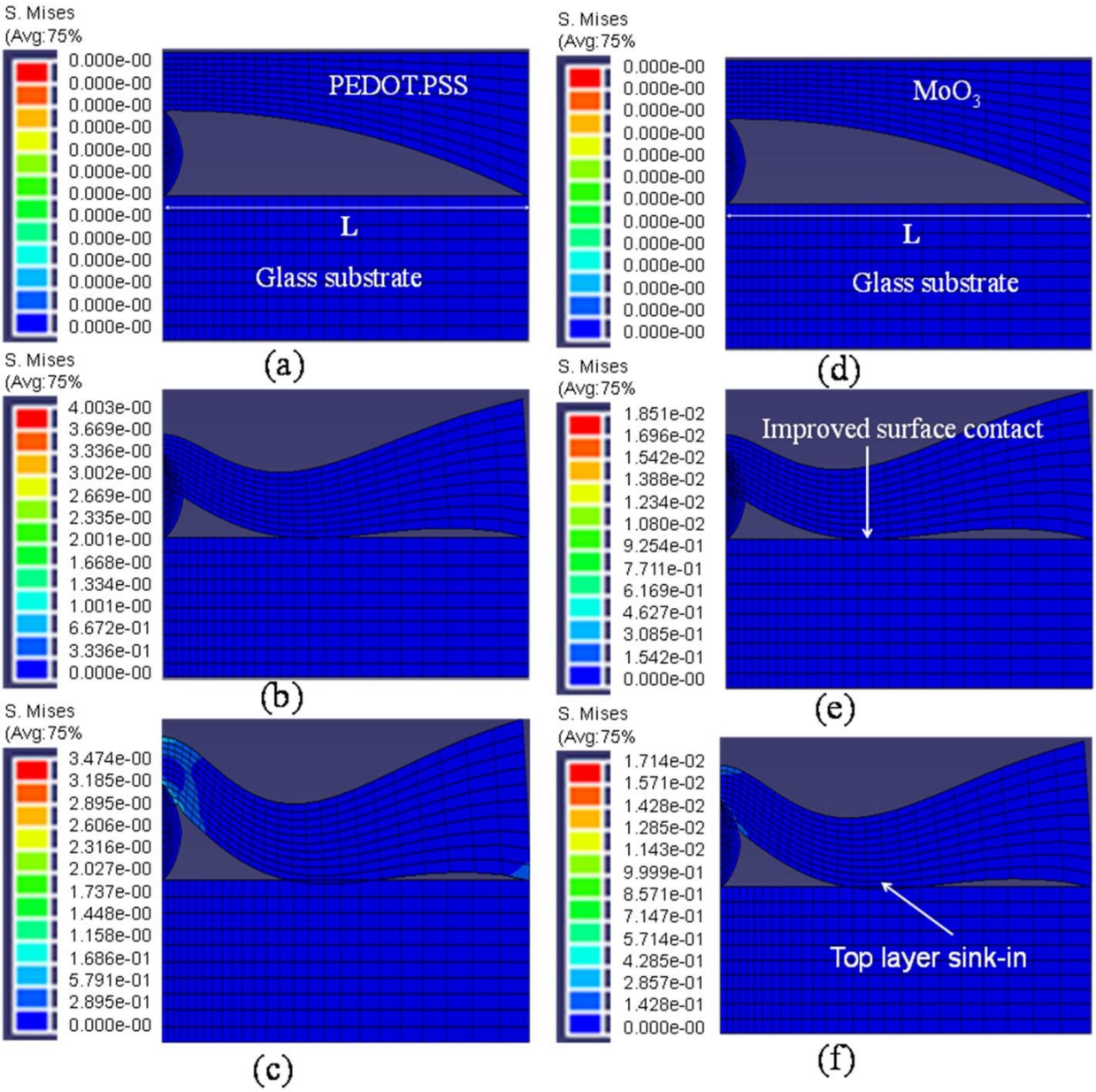

Figure 5.6 Finite element simulation of bi-materials pairs for the rough surface contact based on PEDOT.PSS and MoO_3 devices with dust particle sandwiched between the HIL materials and the glass substrate; (‘a’ and ‘e’) no pressure, (‘b’ and ‘e’) moderate pressure, (‘c’ and ‘f’) high pressure application.

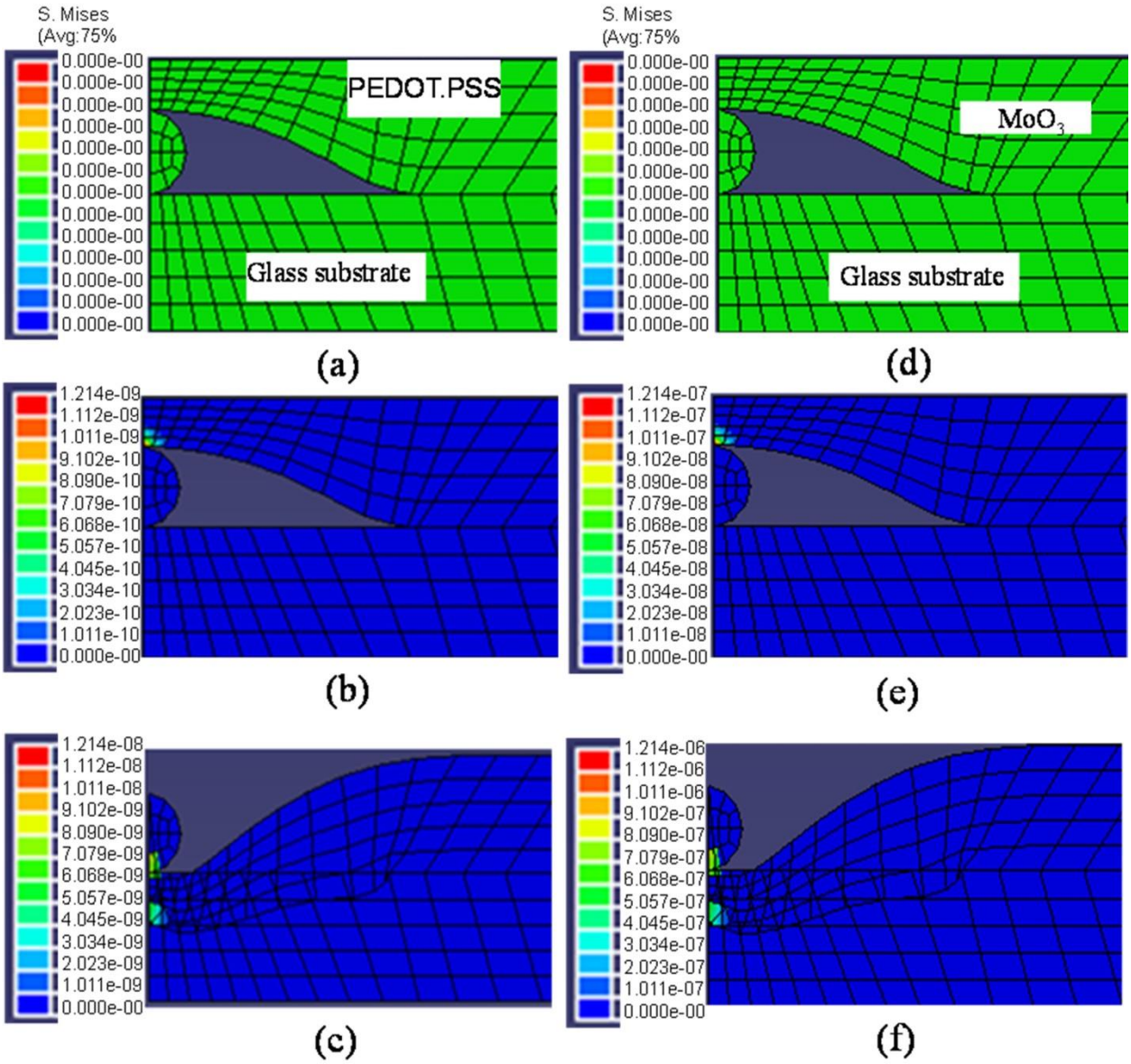

Figure 5.7 Finite element simulation of bi-materials pairs for the arc-shaped contact (smooth surface contact) based on PEDOT.PSS and MoO_3 devices with dust particle sandwiched between the HTL materials and the glass substrate; (‘a’ and ‘e’) no pressure, (‘b’ and ‘e’) moderate pressure, (‘c’ and ‘f’) high pressure application.

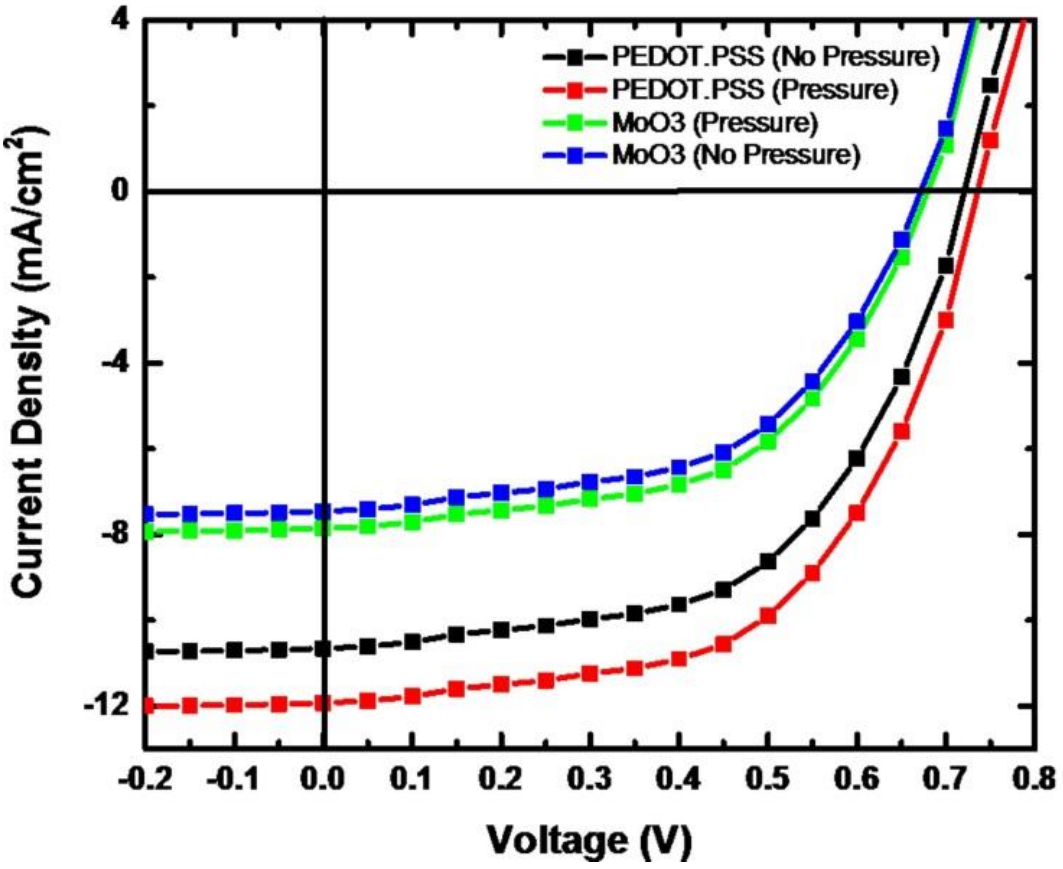

Figure 5.8 Current density and voltage characteristics for AM1.5 illumination of MoO_3 hybrid inorganic-organic photovoltaic devices with and without the influence of pressure

Chapter 6

Design of Thermally Reliable Environmental Barrier Coating for a SiC/SiC Ceramic Matrix Composites

6.1. Introduction

There have been significant efforts to develop silicon (Si)-based ceramics for air breathing engines in combustion environment [1]. This is due to their ability to handle high temperatures. There is no doubt that, the temperature capability of metallic structural components such as blades, nozzles, and combustor liners in hot engine section has become a major problem in the performance of gas turbines [2]. This has led to the development of ceramic matrix composites (CMCs). CMCs are possible candidates for various applications in high temperature environments with aggressive gases and possible corrosion deposits [1]. The hot section of most gas turbine engines can be made from Si-based ceramics such as silicon carbide-fiber-reinforced silicon carbide matrix composites (SiC/SiC CMCs) and monolithic silicon nitride (Si_3N_4) [3].

However, when the Si-based ceramic is exposed to corrosive environments containing high-pressure steam at elevated temperatures, they are susceptible to hot-corrosion and recession. The silica oxidation product formed from Si-containing materials further reacts with water vapor to form $Si(OH)_4$ (g)[1]. To mitigate the recession rates in air breathing silicon containing materials, environmental barrier coatings (EBCs) are needed. EBCs protect, SiC/SiC CMCs and other silicon containing materials from oxidation and recession. Among the factors considered for proper functioning of an EBC include phase stability of the coating with the substrate, e.g., SiC, and low coefficient of thermal expansion (CTE) with the substrate. The EBC should also have low permeability to oxygen, chemical compatibility with the silica scale formed from oxidation [4].

EBC design usually consists of two or more coating layers. Among the constituents of EBCs for SiC/SiC composites are Barium-Strontium-Alumino-Silicate (BSAS), rare earth mono- and di-silicates, and hafnia/zirconia based systems [3, 5, 6, 7]. Microstructure and durability of such coatings depend on the thickness and the processing methods used. Air plasma spray (APS), sputtering or slurry deposition and electron beam assisted physical vapor deposition are some of the common techniques for coating SiC/SiC turbine composites [8]. The first generation EBC consists of two layers; namely, mullite bond coat and yttria-stabilized zirconia (YSZ, ZrO_2 - 8 wt. % Y_2O_3) top coat. Second generation EBCs with substantially improved performance consist of three layers, a silicon bond coat, a mullite or a mullite + BSAS (BaO_{1-x} -SrOx -Al_2O_3 -$2SiO_2$) interlayer [9, 10] and a BSAS top coat.

Constant exposure of the EBCs to air breathing conditions introduces thermal residual stresses in the coating which eventually leads to the failure of the coatings [8]. Understanding the residual stresses [13] within the EBC multilayers enable the design of solutions to EBC failure.

In this chapter, EBC design and two dimensional (2D) thermal residual stresses analyses of a reliable EBC for a SiC/SiC CMCs are discussed.

6.2. Materials and Methods

6.2.1. EBC Design and Architecture

The design considered a three multilayer EBC on SiC/SiC CMC. Each distinct layer performs a unique function(s). The first layer serves as a bond coat with SiC/SiC CMC, the intermediate layer helps to prevent oxidation, while the topcoat increases oxidation resistance and slows down SiO_2 volatilization as shown in Figure 6.1a.

6.2.2. Environmental Barrier Coating: Materials Selection

6.2.2.1. Oxide layer selection

In this paper, the choice of materials for the bond coat was based on the following factors; environmental stability, especially in water vapor, CTE match, and chemical compatibility with SiC/SiC. Based on the above factors, $Y_2Si_2O_7$, $Yb_2Si_2O_7$ and $2Al_2O_3{\cdot}3SiO_2$ were selected as bond coat, top coat and intermediate layer respectively. Due to its similar low CTE to SiC ~ 4.0 x $10^{-6}/^{o}$C [14], $Y_2Si_2O_7$ was chosen as bond coat material. To grade the

CTE, mullite with CTE~ 5.5 x $10^{-6}/^{o}C$ [14] was selected as the intermediate layer to prevent oxidation. $Yb_2Si_2O_7$ (with CTE of 4.8 x$10^{-6}/^{o}C$ [9]) was finally chosen as the top coat to improve the oxidation resistance and also to minimize SiO_2 volatilization. The layer thicknesses were varied as shown in Table 6.1 and their corresponding thermal residual stresses were predicted using finite element modeling (FEM).

6.2.3. FEM of Thermal Residual Stress

Thermo-mechanical simulations of the multilayer structure were performed using the Structural Mechanics Module and Heat Transfer Module of COMSOL Multiphysics 3.4 Software Package (Stockholm, Sweden). The 2D FEM was used to analyze the build-up of the thermal residual stresses within the proposed EBC layers during service condition. The modelling was based on three-node elements and a fine mesh through both the coating layer and the substrate interface. Models 1, 2 and 3 meshes consist of 51392, 35744 and 37920 elements, respectively as shown in Table 6.1 for the three different EBC model dimensions used. Each model consists of the same three sub layers but different thicknesses. The thicknesses of the distinct layers were varied to investigate its effects on the thermal residual stresses under service conditions. The width of each model was 6 mm.

The physical, thermal, and mechanical properties of the candidate coating layers and the substrate are presented in Table 6.2. The boundary condition was chosen such that, there was no displacement in x-direction for the bottom of the substrate. Thermal boundary conditions' effects were imitated by applying a temperature of 1500°C to the top layer and 25^{o}C to the

bottom part of the SiC/SiC CMC. Internal thermal boundaries between the layers of the thermo-mechanical models were set to continuity. Also, the left and right side of EBC system were thermally insulated in all the three models. Time-dependent analysis with linear analysis system solver was used for all the three models. Direct solution methods were considered in the FEM, because it is faster than iterative methods, and it is always recommended for 2D built models.

6.3. Results and Discussion

The conventional EBC is made up of BSAS, Mullite and Silicon with BSAS as top coat as shown in Figure 6.2 a-b [14]. Low melting silicon at temperatures > 1400^{o}C prevents its use at higher temperatures. Further, in water-vapor atmospheres, BSAS suffers significant recession via volatilization at temperatures beyond 1400°C. $Y_2Si_2O_7$ was chosen because of its low volatility and low CTE that matches the CTE of $Y_2Si_2O_7$ and its improved adherence to SiC. The material combination systems and their interfacial interactions are presented in detail in section 6.1 to 6.3

6.3.1. $Y_2Si_2O_7$ - (SiC/SiC) System

In the conventional design, silicon is used as bond coat (Fig. 6.2(a-b)) due to its unique adherence to the SiC/SiC CMC. However, the use of silicon as a bond coat is limited by its melting point (~1416^{o}C). In air breathing engines that operate at temperatures greater than 1500^{o}C, Si will melt leading to a significant reduction in service time of the EBC. In this work, Si was replaced by $Y_2Si_2O_7$ which has a melting temperature of 1775^{o}C [12, 20and

have tsimilar CTE with SiC ~4 x $10^{-6}/^{o}$C. Therefore the use of $Y_2Si_2O_7$ as a bond coat will provide good adherence to the SiC/SiC CMC. $Y_2Si_2O_7$ has a low thermal conductivity of <3.0 W/mK above 300^{o}C and also, stable with SiO_2 which is an oxidation product of SiC. This combination of properties suggests $Y_2Si_2O_7$ as a possible bond coat with SiC/SiC CMCs.

6.3.2. Mullite/$Y_2Si_2O_7$ System

Mullite is selected as the intermediate layer due to its close CTE match with $Y_2Si_2O_7$ hence may bond easily to mullite. Also, $Yb_2Si_2O_7$ has been shown to adhere to mullite [24]. Mullite is thermally stable up to 1890^{o}C and is stable in dry and oxidizing atmospheres.

6.3.3. $Yb_2Si_2O_7$/Mullite System

An oxide with low water-vapor volatility will serve as a good top coat on mullite, which has relatively high silica activity (~0.3 - 0.4 μm/h). High silica activity results in higher selective volatilization of silica and the recession of mullite [25]. Volatilization of silica from the mullite leads to a porous alumina and irregular cracks. [14]. A top coat of $Yb_2Si_2O_7$ will protect the mullite interlayer from water vapor attack and subsequently mitigate its volatilization. $Yb_2Si_2O_7$ is known to have a low recession rate than mullite [24]. Bansal et al. showed $Yb_2Si_2O_7$ top coat on mullite to provide an EBC with no through thickness cracks (Figure 6.5). $Yb_2Si_2O_7$ is thermally compatible with mullite and provides good adherence due to CTE (4 x$10^{-6}/^{o}$C) match with mullite, CTE ~ 5 x$10^{-6}/^{o}$C. Further, advantage of the use of $Yb_2Si_2O_7$ is that, it is thermally stable up to 1850^{o}C. From the Rare earth disilicate polymorph

phase diagram shown in figure 6.3(a), both Lu-silicates and Yb-silicates exhibit monoclinic phase stability up to 1600°C; but due to significant higher cost of Lu, Yb was investigated more closely. Polymorphic rare earth disilicate materials vary in density and are not desirable coating candidates since volume change due to phase transformation [26] may cause cracks. The high melting temperature of $Yb_2Si_2O_7$ (~1850^oC) makes it applicable in air breathing engines operating at temperatures of less than 1500^oC.

6.3.4. Thermal Residual Stress Modelling Results

Figures 6.6 (a-c) present the finite element analyses of the thermal residual stresses obtained for models 1, 2 and 3. The thermal load at the surface of all the three models is identical. Figure 6.6 shows the stresses within the EBC layers due to the surface thermal loading applied at 1500^oC on both the coating and the substrate. It was observed that, the magnitude of thermal residual stresses within each layer is decreased when the thickness of the top coat increases. The smaller the thickness of the top coat, the higher the thermal gradient in the $Yb_2Si_2O_7$ coating and as a result, a higher surface compressive stress was expected as reported by Choules et al., 2001 [27] and Aziz et al., 2009 [11]. Thermal residual stresses are generated in the EBC multilayered system due to differences in the thermal and elastic properties of the underlying layers. Also, it was observed that, the thermal stress contribution in the coating was compressive while the substrate exhibited tensile thermal stress. This is as a result of difference between the substrate's (SiC/SiC) CTE and the EBC's CTE. The thickness of the $Yb_2Si_2O_7$ top layer in model 1 is greater than the subsequent two

coats. Comparing figures 6.6 (a-c), show that, when the thickness of the top coat is small, the magnitude of thermal residual stresses within the layer is high. Since for all the three models, the CTE and elastic modulus mismatch between the underlying layers were the same, the difference in the thermal stresses were due to the difference in the thicknesses. It is very clear from Figure 6.6 (c) that, the order of magnitude of the residual stresses is higher in model 3 than model 1 and 2. Comparing the three FEM results suggest that, model 1 has a better architecture in the proposed EBC system for SiC/SiC CMCs because the residual stresses are minimal. The lower the magnitude of the residual stresses, the greater the underlying coating can adhere.

6.4. Conclusion

In this study, a novel EBC system for SiC/SiC CMCs applicable for use in air breathing engines was designed and the thermal residual stresses within the system were modelled to determine the optimum layer thickness. Three-layer EBC system was chosen based on the following factors: (i) Environmental stability, especially water vapour (ii) CTE match; (iii) Chemical compatibility; and (iv) Phase stability. Based on these requirements, the following three-layer coatings were recommended; namely: $Y_2Si_2O_7$ (bond coat), $3Al_2O_3{\cdot}2SiO_2$ (interlayer) and $Yb_2Si_2O_7$ (top coat). The design indicates that, when Si bond coat is replaced by $Y_2Si_2O_7$, the EBC system function in air breathing engine at temperature (~ 1500 ^oC) because, $Y_2Si_2O_7$ melts at ~ 1775 ^oC and Si melts at ~1416 ^oC respectively.

The thermal residual stresses within the proposed three multilayers models with SiC/SiC substrate during service condition were modeled using COMSOL Multiphysics 3.4. The FEM results show that, the thermal residual stress within the top layer decreased when the layer thickness was increased. The thermal residual stresses in the coating decreased as the thickness of the top coat increased.

6.5 References

[1] Jacobson, N. S., Opila, E. J. and Lee, K. N., "Oxidation and Corrosion of Ceramics and Ceramic Matrix Composites," *Current Opinion in Solid State and Materials Science 5,* 301–309, 2001.

[2] K. N. Lee, D.S. Fox, J.I. Eldridge, D. Zhu, R.C. Robinson, N.P. Bansal and R.A. Miller. "Upper Temperature Limit of Environmental Barrier Coating Based on Mullite and BSAS," *J. Am. Ceram. Soc.* 86 [8] 1299-306, 2003.

[3] Lee, K.N., Fox, D.S., Robinson R.C. and Bansal, N.P., "Environmental Barrier coatings for Silicon-based Ceramics, High Temperature Ceramic matrix Composite," Krenkel, W., Naslain, R. and Schneider, H. (eds), *High temperature ceramic matrix composites*. Weinheim, Germany: Wiley- VCH, pp. 224–229, 2001.

[4] UK Patent no. 2427201, "Thermal/Environmental Barrier Coating System for Silicon-containing metals", 2013.

[5] K.N. Lee, D.S. Fox and N.P. Bansal, "Rare Earth Environmental Barrier Coatings for SiC/SiC Composites and Si_3N_4 Ceramics," *J. Eur. Ceram. Soc.,* 25(10): 1705–1715, 2005.

[6] N.P. Bansal, J.P. Singh, W.M. Kriven and H. Schnneider, "Advances in Ceramic Matrix Composites IX," *J. Am. Ceram. Soc.*,Vol. 153, pp. 331–343, 2003.

[7] D. M. Zhu, R.A. Miller and D.S. Fox, "Thermal and Environmental Barrier Coating Development for Advanced Propulsion Engine Systems. NASA TM-2008-215040, Jan., 2008.

[8] A. Abdul-Aziz and R.T. Bhatt, "Modeling of Thermal Residual Stress in Environmental Barrier Coated Fiber Reinforced Ceramic Matrix Composite," *Journal of composite materials,* 0(0) 1-8, 2011.

[9] H. E. Eaton and G.D. Linsey, "Acceleration Oxidation of SiC CMC's By Water Vapor and Protection via Environmental Barrier Coating Approach," *J. Eur. Ceram. Soc.*, 22:2741, 2002.

[10] S. Uenoa, T. Ohji and H. Lin, "Corrosion and Recession of Mullite in Water Vapor Environment," *J. Eur. Ceram. Soc*., 28:431, 2008

[11] K.N. Lee, J.I. Eldridge and R.C. Robinson, "Residual Stresses and their Effects on the Durability of Environment Barrier Coatings for SiC Ceramics," *J. Eur. Ceram. Soc.,* 88(12): 3483, 2005.

[12] Z. Sun, Y. Zhou, J. Wang and M. Li, ''γ-$Y_2Si_2O_7$, a Machinable Silicate Ceramic: Mechanical Properties and Machinability,'' *J. Am. Ceram. Soc*., 90, 2535–41, 2007.

[13] Z. Sun, L.Wu, M. Li, Y. Zhou, "Tribological Properties of γ-$Y_2Si_2O_7$ Ceramic against AISI 52100 Steel and Si_3N_4 Ceramic Counterparts," *Wear*, 266 960–967, 2009.

[14] B. J. Harder, J.D. Almer, C.M. Weyant, K.N. Lee and K.T. Faber, "Residual Stress Analysis of Multilayer Environmental Barrier Coatings," *J. Am. Ceram. Soc.,* 92[2] 452–459, 2009.

[15] H. Samadi, "A Thick Multilayer Thermal Barrier Coating: Design, Deposition, and Internal Stresses," Dept. of Materials Science and Engineering, *University of Toronto*. PhD thesis, 2009.

[16] Y.R. Takeuchi and K. Kokini, "Thermal Fracture of Multilayer Ceramic Thermal Barrier Coatings, *Journal of Engineering for Gas Turbines and Power-Transactions of the ASME*, 1994, 116, p. 266-271.

[17] Z. Sun, M. Li, and Y. Zhou, "Thermal properties of single phase Y_2SiO_5," *Journal of the European Ceramic Society* 29 551–557, 2009.

[18] C. M. Toohey, "Novel Environmental Barrier Coatings for Resistance against Degradation by Molten, Glassy Deposits in the Presence of Water Vapor," *Ohio State University*, Masters Thesis, 2011.

[19] International Town Meeting on SiC/SiC Design and Material Issues for Fusion Systems Oak Ridge, January 18-19, 2000.

[20] A.I. Becerro and A. Escudero, ''Polymorphism in the $Lu_{2-x}Y_xSi_2O_7$ System at High Temperatures,'' *J. Eur. Ceram. Soc.*, 26. 2293–9. 2006.

[21] D.M. Cupid and H. J. Seifert, ''Thermodynamic Calculations and Phase Stabilities in the Y–Si–C–O System,'' *J. Phase Equilib. Diff.*, 28, 90–100. 2007.

[22] J. Felsche, ''Polymorphism and Crystal Data of the Rare-Earth Disilicates of Type $RE_2Si_2O_7$,'' *J. Less Common Met.*, 21, 1–14. 1970.

[23] J. Felsche, ''The Crystal Chemistry of Rare-Earth Silicates,'' *Struct. Bonding*, 13, 99–113. 1973.

[24] K.N. Lee, "Current Status of Environmental Barrier Coatings for Si-based Ceramics," *Surface and Coatings Technology*, 133-134, 1-7. 2000.

[25] K. N. Lee, Transactions of the ASME 122 (2000): 632-636.

[26] X. Yue, and Y. Zhaotong, “Investigation on the Preparation of Si/mullite/$Yb_2Si_2O_7$ Environmental Barrier Coatings onto Silicon Carbide,” *Journal of Rare Earths*, Vol. 28, No. 3, p. 399. Jun. 2010.

[27] B. D. Choules, K. Kokini and T.A Taylor, “Thermal fracture of ceramic thermal barrier coatings under high heat flux with time-dependent behaviour,” Materials *Science and Engineering a-Structural Materials Properties Microstructure and Processing*, 2001, 299, p. 96-304.

LIST OF TABLES

Table 6.1 Layer thickness used in the FEM

Layers	Model 1	Model 2	Model 3
	Layer thickness	Layer thickness	Layer thickness
$Y_2Si_2O_7$	200 µm	100 µm	100 µm
$3Al_2O_3.2SiO_2$	200 µm	100 µm	200 µm
$Yb_2Si_2O_7$	130 µm	100 µm	75 µm
SiC/SiC CMC	3 mm	3 mm	3 mm

Table 6.2 Physical, thermal, and mechanical properties of the proposed multilayers

Layers	CTE (/°C)	Thermal Conductivity (W/m-K)	Heat Capacity (J/Kg.K)	Density (g/cm^3)	Elastic Modulus (GPa)	Poisson's Ratio
$Y_2Si_2O_7$	3.9×10^{-6} [12]	3.5 [13]	274*	3.96 [13]	155 [13]	0.27 [12]
$3Al_2O_3.2SiO_2$	5.5×10^{-6} [14]	1.29 [15]	760 [15]	2.71 [15]	145 [14]	0.25 [16]
$Yb_2Si_2O_7$	4.8×10^{-6} [9]	1.86 [17]	274*	6.19 [18]	90 [9]	0.18 [9]
SiC/SiC CMC	4.0×10^{-6} [19]	9.0 [19]	750 [19]	2.4 [19]	300 [19]	0.16 [19]

FIGURES

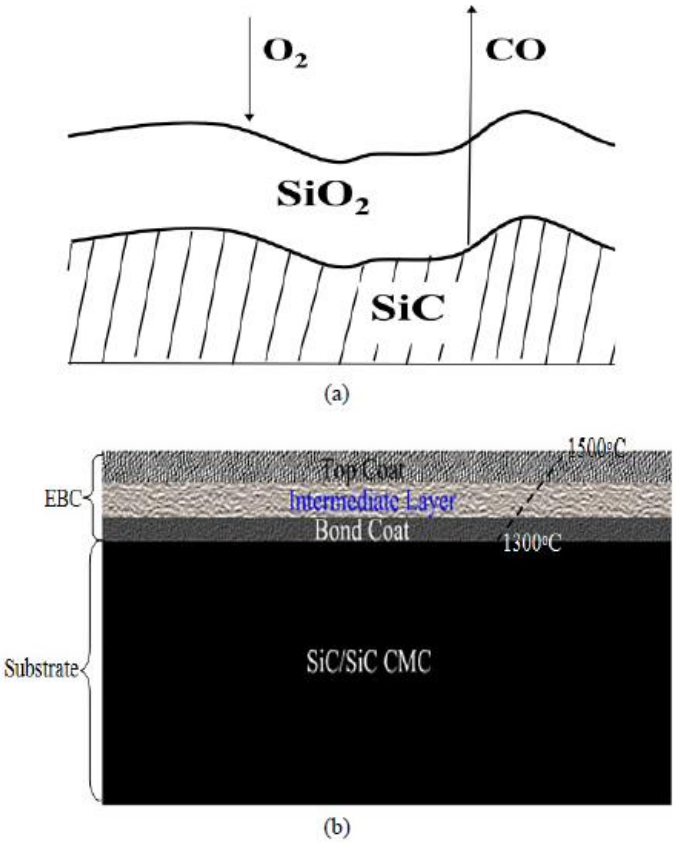

Figure 6.1: Schematic diagram of (a) surface recession of SiC and (b) SiC/SiC CMCs coated with EBC

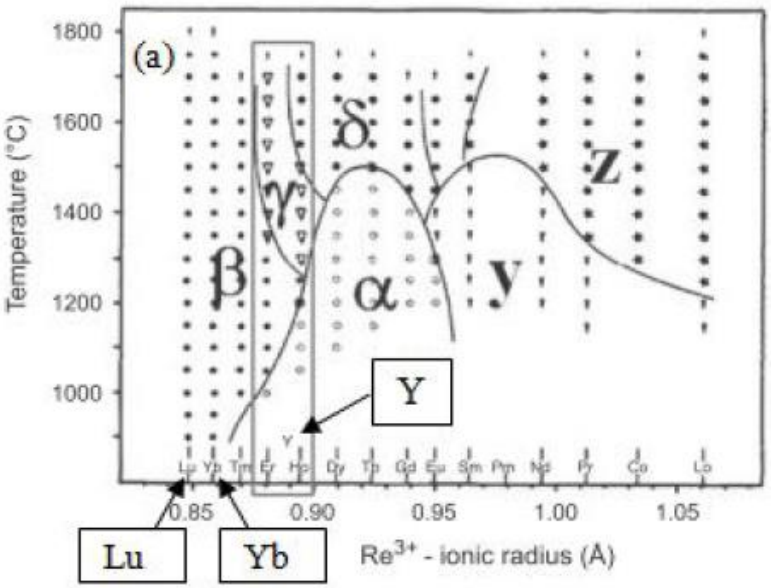

Figure 6.2 Phase diagram of rare earth disilicate polymorph [22, 23]

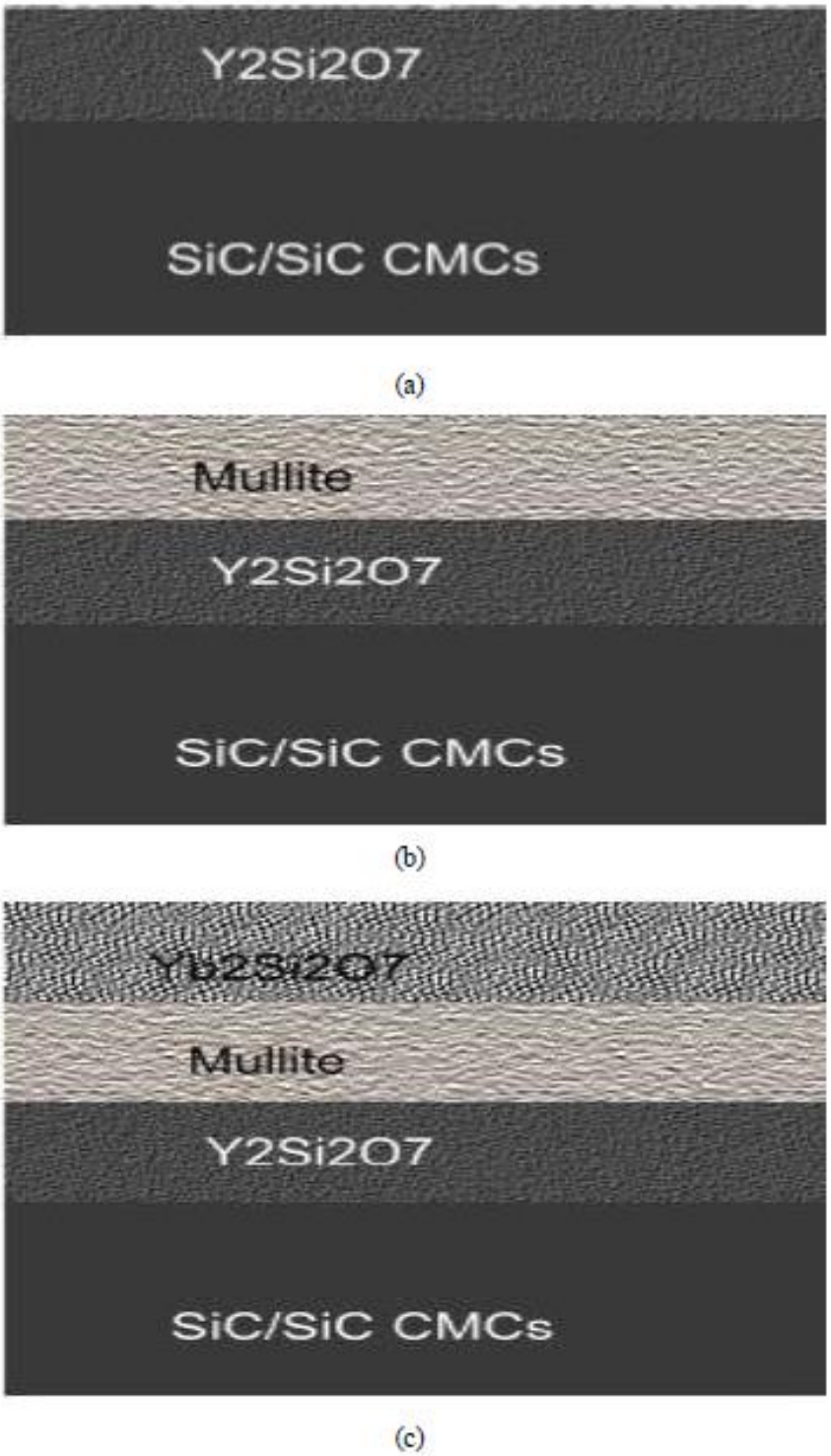

Figure 6.3: Structural schematic diagram (a) $Y_2Si_2O_7$, (b) $Y_2Si_2O_7$/mullite (c) $Y_2Si_2O_7$ /mullite /$Yb_2Si_2O_7$coatings system with SiC/SiC

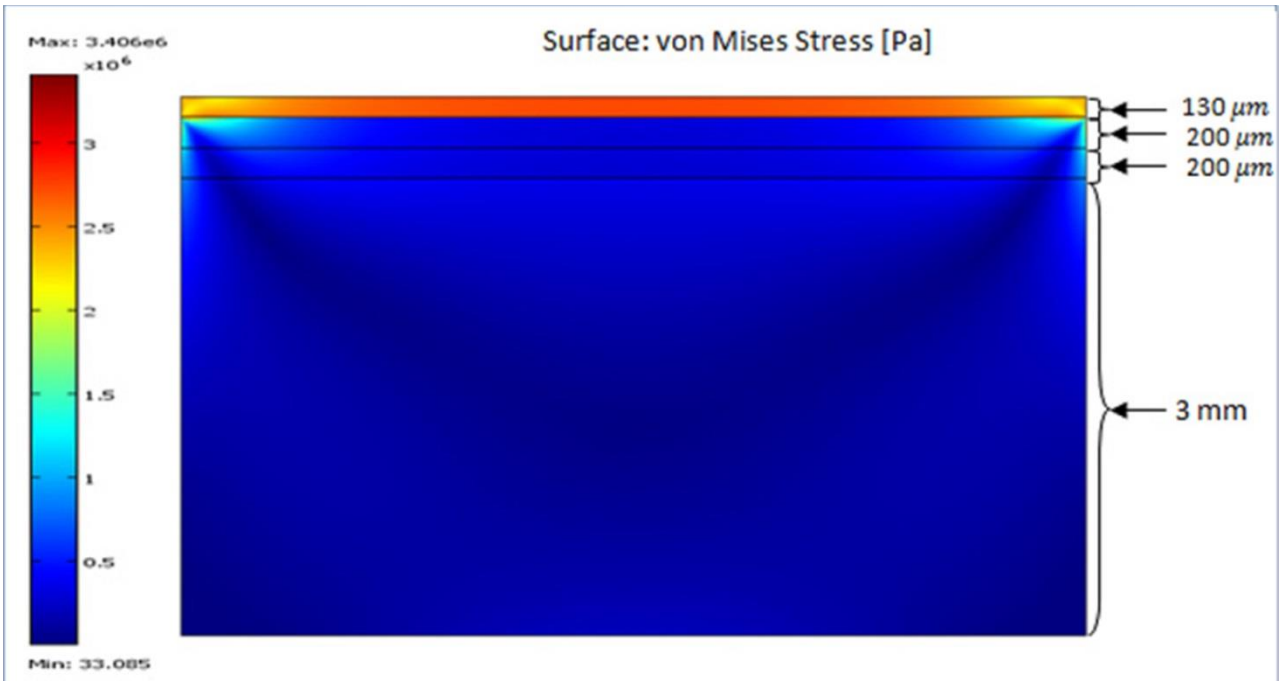
Surface: von Mises Stress [Pa]
Max: 3.406e6
x10^6
3
2.5
2
1.5
1
0.5
Min: 33.085
130 μm
200 μm
200 μm
3 mm

(a)

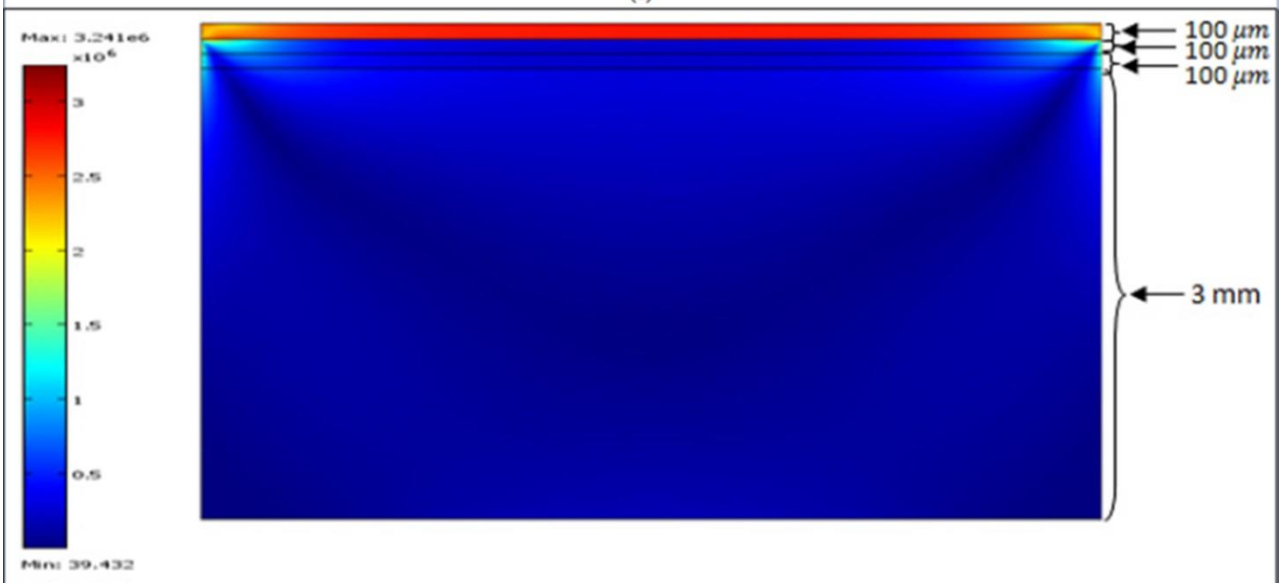
Max: 3.241e6
x10^6
3
2.5
2
1.5
1
0.5
Min: 39.432
100 μm
100 μm
100 μm
3 mm

(b)

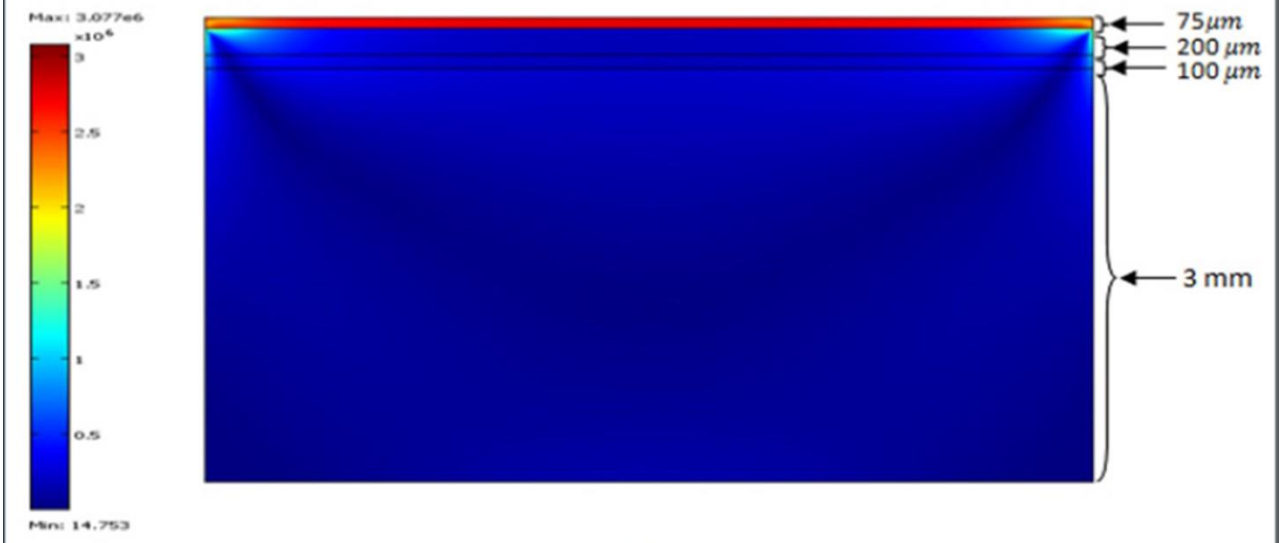
Max: 3.077e6
x10^6
3
2.5
2
1.5
1
0.5
Min: 14.753
75μm
200 μm
100 μm
3 mm

(c)

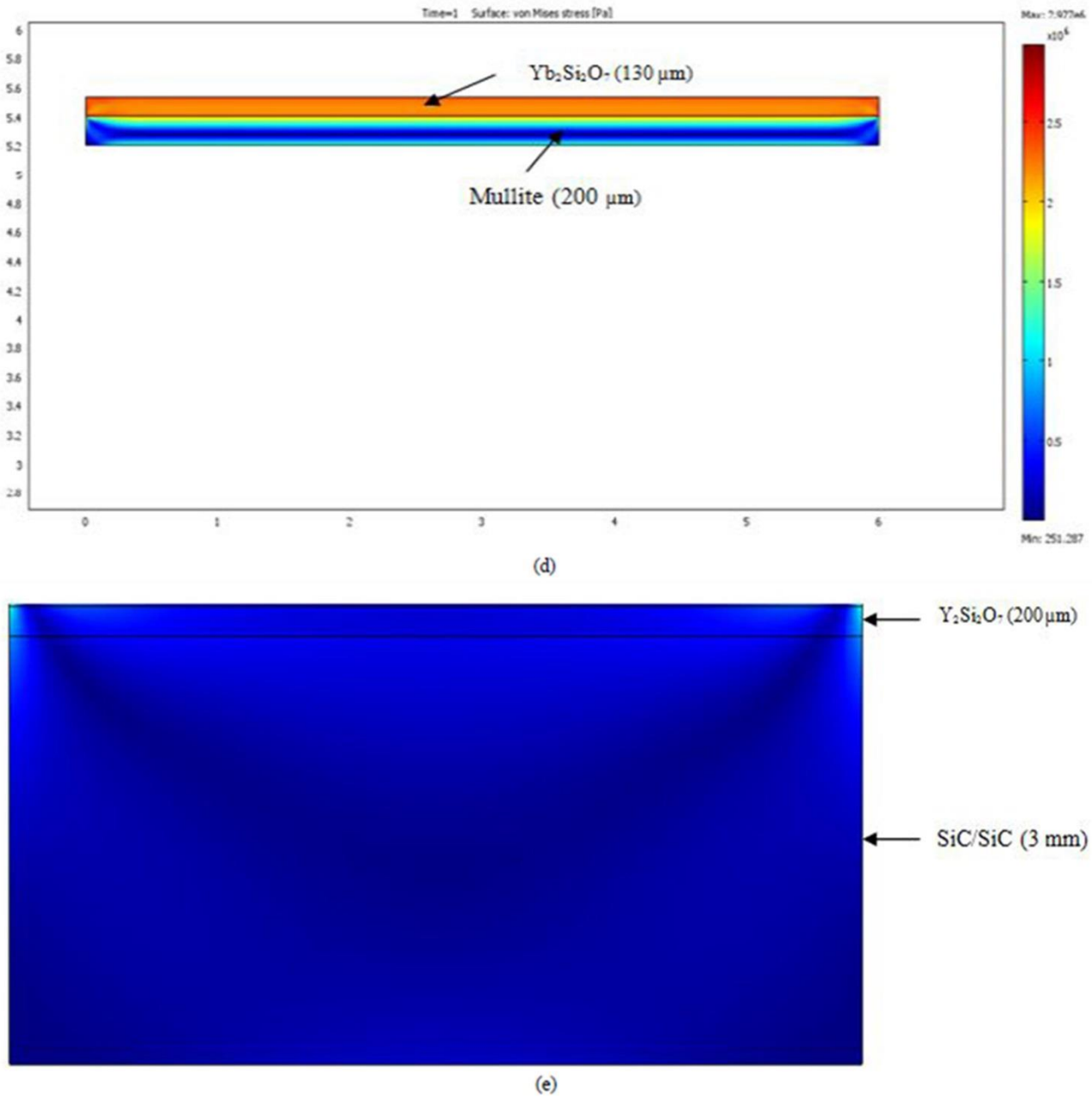

Figure 6.4a-e. Show the FEM for different EBC architecture and thicknesses; (a) Model 1: $Y_2Si_2O_7$ (200), Mullite (200) and $Yb_2Si_2O_7$ (130) ; (b) Model 2: $Y_2Si_2O_7$ (200), Mullite (200) and $Yb_2Si_2O_7$ (130) (c) Model 3: $Y_2Si_2O_7$ (200), Mullite (200) and $Yb_2Si_2O_7$ (130) with the SiC/SiC substrate. (d) Residual stress distribution within only Mullite (200) and $Yb_2Si_2O_7$ (130) and (e) Residual stress distribution within only the $Y_2Si_2O_7$ (200) and SiC/SiC substrate (3mm)

Chapter 7

Conclusion and Suggestions for Future work

7.1 Conclusions

This dissertation has presented efforts to use combined analytical, experimental and computational approaches to explore adhesion and contacts in hybrid organic and inorganic materials for photovoltaic applications. The chapters include: the effect of pressure on contacts between layers relevant to hybrid inorganic-organic materials for photovoltaic applications, the pressure and annealing effects on active layer processing and the influence of metallic surface oxides in optoelectronic devices. The key findings and some appropriate conclusions are summarized below:

7.1.1 Effect of Pressure on Interfacial Surface Contacts and Current-Voltage Characteristics of Organic Solar Cells

This paper presents the results of a combined analytical, computational and experimental study of interfacial surface contacts and current-voltage behavior, induced via pressure assistance on the OPV layers and devices. The models, using the adhesion energies, the Young's moduli of the OPV layers, trapped particles and the surface roughness characteristics of the layers were carried

out to assess the influence of pressure application. The predictions from the models were also verified with experimental results. The void length reduction and the contact length increase are associated with increases in the applied pressure. The pressure increases also results in improved power conversion efficiencies for devices with PEDOT.PSS HTL subjected to ~10 MPa pressure. The improvements are attributed to the combined effects of increased surface contacts and increased polymer crystallinity that occur during pressure application and annealing.

The current results suggest that pressure-induced contacts may be used to enhance the current-voltage response and power conversion efficiencies of organic photovoltaic cells. However, excessive pressure must be avoided to reduce the possibility of device damage due to sink-in of trapped particles. The surface roughness of the device layers should also be reduced to improve the adhesion and surface contacts in the OPV layers.

7.1.2 Effects of Pressure on Nano- and Micro- scale Morphological Changes in Conjugated Polymer Photovoltaic Cells

Organic Photovoltaic devices with enhanced efficiencies was fabricated and tested by the manipulation of the nano- and micro-structures of the active layers in bulk heterojunction solar cells. The results of the experimental study of the changes in the structure of the P3HT:PCBM blends suggested that annealing and pressure application can be used to control the surface morphology, crystallinity and current-voltage characteristics of bulk heterojunction solar cells. The Pressure application also resulted in the stretching of the polymer chains, predominantly in the edge-on configurations, with reduced lamellae spacing. The edge-on configuration induced polymer crystallinity, as well as significant enhancements in the current-voltage characteristics, and photoconversion efficiencies of the bulk heterojunction solar cells.

7.1.3 Pressure-Assisted Fabrication of Hybrid Materials Photovoltaic Cells

This chapter presented the results of a combined analytical/computational and experimental study of pressure induced contacts between layers in hybrid photovoltaic cells. The contacts between the inorganic MoO_3 and other organic layers were modeled using analytical concepts and finite element models. The potential effects of surface roughness and dust particles were also considered along with the effects of pressure and adhesion energy.

The results show that, increased pressure is associated with decreasing void length or increased contact length. Increased pressure also results in improved power conversion efficiency (from 3.79 to 5.02% for devices with PEDOT.PSS HTL and from 2.75 to 2.96% for devices with MoO_3 HTL). The improvements are partly attributed to the increased surface contacts that occur with increasing pressure. However, these effects are reduced when the HTL materials are stiffer. They are also as a result of the improvement in the crystallinity of the polymer chains during the pressure application.

The current results suggest that pressure-induced contacts may be used to enhance the current-voltage characteristics and power conversion efficiencies of organic photovoltaic cells. However excessive pressure must be avoided to reduce the possibility of device damage due to sink-in of dust particles. The surface roughness of the device layers should also be reduced to improve the contacts between the layers.

7.1.4. Design of Thermally Reliable Environmental Barrier Coating for a SiC/SiC Ceramic Matrix Composite

In this study, a novel EBC system for SiC/SiC CMCs applicable for use in air breathing engines was designed and the thermal residual stresses within the system were modelled to determine the optimum layer thickness. Three-layer EBC system was chosen based on the following factors: (i)

Environmental stability, especially water vapour (ii) CTE match; (iii) Chemical compatibility; and (iv) phase stability. Based on these requirements, the following three-layer coatings were recommended; namely: $Y_2Si_2O_7$ (bond coat), $3Al_2O_3{\cdot}2SiO_2$ (interlayer) and $Yb_2Si_2O_7$ (top coat). The design indicates that, when Si bond coat is replaced by $Y_2Si_2O_7$, the EBC system function in air breathing engine at temperature (~ 1500 ^oC) because, $Y_2Si_2O_7$ melts at ~ 1775 ^oC and Si melts at ~1416 ^oC respectively. The thermal residual stresses within the proposed three multilayers models with SiC/SiC substrate during service condition were modeled using COMSOL Multiphysics 3.4. The FEM results show that, the thermal residual stress within the top layer decreased when the layer thickness was increased. The thermal residual stresses in the coating decreased as the thickness of the top coat increased.

7.2 Future Work

7.2.1 Effects of Pressure on Interfacial Surface and Current-Voltage Characteristics of Organic Photovoltaic cells

Further work can be done to study the mechanism of charge transport across the interfaces in the presence of micro- and nano- voids. The stress distributions around the trapped particle regions can also be further studied with increased mesh sizes and finite element simulations. These will assist in explain into detail, the current-voltage response of the organic solar cells

7.2.2 Effects of Pressure on Nano- and Micro- scale Morphological Changes in Conjugated Polymer Photovoltaic Cells

However, additional work is needed to quantify the relative contributions of changes in P3HT microstructure and the interfaces between P3HT and PCBM to device performance as a result of low and elevated-temperature exposures with pressure application. Analytical and computational

models should be carried out to explain the differences in microstructural morphology, and how they can influence the overall electrical and optical properties.

7.2.3 Pressure-Assisted Fabrication of Hybrid Photovoltaic cells

Further work can be done to more directly link this section's results of devices' mechanical characteristic with their electrical performance. For example, maps of current density could be taken to compare the spatial distribution of areas with strong adhesion with those of high charge transport.

Also, due to the very thin film of MoO_3 layers, the pressure effect on the current density-voltage behavior could not be clearly evaluated probably because of the non-uniformity. This may have led to multiple contacts which are sure avenues for current leakage or short circuiting in the OPV devices. Further experiments with relatively thicker films should be carried out and the pressure effects re-evaluated. Finally, further AFM analyses could be done to ascertain the surface roughness' of the very thin films to confirm it impacts of multiple contacts.

7.2.3. Design of Thermally Reliable Environmental Barrier Coating for a SiC/SiC Ceramic Matrix Composite

There is the need to study further the nature of stresses within the top and middle coat, and the middle and top coat and how these relate to the overall thermal stress decrease when the bond coat material thickness is increased. Further work is recommended in the FEM analyses to better reflect results of the thermal residual stress within the top layer which decreased when the layer thickness was increased. We were limited by the number of elements since we used the student edition of COMSOL Multiphysics 3.4.